Electronic and transport properties of nanotubes

Jean-Christophe Charlier[*]

Unité de Physico-Chimie et de Physique des Matériaux (PCPM), Université Catholique de Louvain, 1 Place Croix du Sud, B-1348 Louvain-la-Neuve, Belgium

Xavier Blase[†]

Université de Louvain, F-69000, France, Laboratoire de Physique de la Matière Condensée et Nanostructures, Université Lyon I, CNRS, UMR 5586, Domaine scientifique de la Doua, F-69622 Villeurbanne Cedex, France

Stephan Roche[‡]

Commissariat à l'Energie Atomique, DSM/DRFMC/SPSMS/GT, 17 rue des Martyrs, 38054 Grenoble Cedex 9, France

(Published 16 May 2007)

This article reviews the electronic and transport properties of carbon nanotubes. The focus is mainly theoretical, but when appropriate the relation with experimental results is mentioned. While simple band-folding arguments will be invoked to rationalize how the metallic or semiconducting character of nanotubes is inferred from their topological structure, more sophisticated tight-binding and *ab initio* treatments will be introduced to discuss more subtle physical effects, such as those induced by curvature, tube-tube interactions, or topological defects. The same approach will be followed for transport properties. The fundamental aspects of conduction regimes and transport length scales will be presented using simple models of disorder, with the derivation of a few analytic results concerning specific situations of short- and long-range static perturbations. Further, the latest developments in semiempirical or *ab initio* simulations aimed at exploring the effect of realistic static scatterers (chemical impurities, adsorbed molecules, etc.) or inelastic electron-phonon interactions will be emphasized. Finally, specific issues, going beyond the noninteracting electron model, will be addressed, including excitonic effects in optical experiments, the Coulomb-blockade regime, and the Luttinger liquid, charge density waves, or superconducting transition.

PACS number(s): 73.63.Fg, 73.22.−f, 78.67.Ch, 61.46.Fg

CONTENTS

---

*Electronic address: charlier@pcpm.ucl.ac.be
†Electronic address: xblase@lpmcn.univ-lyon1.fr
‡Electronic address: stephan.roche@cea.fr

I. INTRODUCTION

The physics of one-dimensional (1D) systems has been a rich and active playground for theorists for more than 50 years, with major conceptual breakthroughs arising from the specific properties of the confined electron gas. While the reduced dimensionality is often used in introductory textbooks as a convenient way to simplify the analytic study of electronic properties, the enhanced interaction between electrons in 1D yields several instabilities that are not reproduced by standard tools developed for 3D solids. This richness and complexity involved in extending the basics of condensed matter physics to low-dimensionality systems explain the wealth of work and theories developed to deal with 1D solids or molecular chains.

The difficulty in synthesizing clean 1D systems with metallic behavior has for many decades confined this theoretical work to formal developments and unverified predictions. However, progress in synthesis and characterization techniques in the late 1970s allowed a confrontation between theory and experiments. Besides these fundamental aspects, the technological interest in controlling the properties of nanosized and/or plastic conductors was a strong driver for exploring this field. The attribution of the chemistry Nobel prize in 2000 to A. J. Heeger, A. G. MacDiarmid, and H. Shirakawa for the "discovery and development of conductive polymers" was a clear recognition from the community of the importance, and the difficulty, of obtaining conjugated one-dimensional metallic systems. Further, even when metallic, the conductivity in such systems has been shown to usually remain very low, with in most cases polaron-assisted transport leading to very large effective masses for the carriers. As a paradigmatic example, the conducting (and even superconducting) properties of DNA, at the frontiers of physics, chemistry, and biology, are currently generating fierce controversies in the literature.

The field of nanotubes has strongly benefited from this broad fundamental and technological interest. Not only can nanotubes be metallic, they are also mechani-

cally very stable and strong, and their carrier mobility is equivalent to that of good metals, suggesting that they would make ideal interconnects in nanosized devices. Further, the intrinsic semiconducting character of other tubes, as controlled by their topology, allows us to build logic devices at the nanometer scale, as already demonstrated in many laboratories. Finally, the large fullerene community (yet another area recognized by the Nobel prize in chemistry in 1996), and the even larger family of researchers interested in carbon-based systems, naturally joined this novel and promising field. This merging of interests and communities can certainly explain the formidable success and burgeoning activity generated by the discovery of nanotubes in 1991.

A nanotube is a honeycomb lattice rolled into a hollow cylinder with nanometric diameter and μm length. Depending on the community, specific interests, and targeted applications, nanotubes are regarded as either single molecules or quasi-one-dimensional crystals with translational periodicity along the tube axis. As there are an infinite number of ways of rolling a sheet into a cylinder, the large variety of possible helical geometries, defining the tube chirality, provides a family of nanotubes with different diameters and microscopic structures. Some properties of these nanotubes, such as the elastic ones, can be explained within a macroscopic model of a homogeneous cylinder. Others depend crucially on the atomic configuration. For instance, the electronic and transport properties, which constitute the scope of the present review, are certainly among the most significant physical properties of carbon nanotubes, and crucially depend on the diameter and chirality. This dependence on the atomic configuration, an effect explained below, is quite unique in solid-state physics. This sensitivity constitutes a challenge for synthesis techniques, since well-controlled properties are often desired, but it is also a source of innovation for applications.

In the following sections, we show how carbon nanotubes can be either (semi)metallic or semiconducting, with a band gap varying from zero to a few tenths of an eV, depending on their diameter and chirality. Further, the band gap of semiconducting tubes, or the energy difference between the peaks in the electronic density of states (the so-called van Hove singularities), can be shown to first order to be simply related to the tube diameter. Such remarkable results can be obtained from a variety of considerations, starting from the so-called band-folding approach, based on knowledge of the electronic properties of the graphene sheet, to the direct study of nanotubes using semiempirical tight-binding approaches. The comparison with more sophisticated *ab initio* calculations, and with available experimental results, allows us to set the limits of these simple treatments, with the introduction of finer considerations, such as curvature or trigonal warping effects.

Knowledge of the electronic properties of nanotubes further permits one to study their response to external probes. This is a crucial issue as it conditions most of the potentiality for the integration of tubes in real devices

and allows us to relate the structural and electronic properties with the experimental optical, Raman, etc., spectra. In particular, the effect of a magnetic field on the electronic band structure, the optical absorption and emission spectra, and finally the transport properties of tubes will be presented.

The tremendous importance of the transport properties of nanotubes, from both a fundamental and technological point of view, justifies devoting the second part of this review to that subject. First, the main characteristics of ballistic transport will be clarified, followed by a few analytical results about the absence of backscattering in the presence of long-range disorder and the derivation of the elastic mean free path induced by short-range disorder. All transport regimes will be reviewed in the presence of elastic disorder, starting with the simple Anderson model, followed by an extended analysis of more realistic disorders such as chemical substitutions or functionalization, topological defects, and so on. Quantum interference effects will then be addressed with a focus on weak- and strong-localization regimes, in light of recent experiments. Further, the contribution of inelastic scattering mechanisms (through electron-electron and electron-phonon interactions) will be scrutinized, with a discussion of the inelastic scattering times and decoherence mechanisms. As a specific case of transport (or tunneling), with much technological importance, the physics of field emission from nanotubes will be briefly presented.

Several topics strongly related to quantum confinement and dimensionality effects will be addressed at the end of this review. At the heart of the complex behavior of 1D systems, the physics of the Luttinger-liquid transition will be highlighted and the signature of this transition in available transport experiments will be put in perspective. Coulomb-blockade effects and their manifestation in transport measurements will then be summarized. Finally, the competing charge-density-wave (or Peierls) and superconducting instabilities upon switching on the electron-phonon interaction, observed experimentally, will be discussed.

The contents of the present review are theoretical, and experimental results are used primarily to provide the necessary and crucial evidence for validation of the theory. As a matter of fact, the difficulty in performing the synthesis and characterization of well-defined and isolated nanotubes has on many occasions granted to theory the important, but also dangerous, role of prediction. In return, these experimental difficulties have fostered the elaboration of original and creative experimental techniques. As emphasized below, most of the theoretical predictions seem now to be confirmed by many experimental results.

Even with a focus on theoretical results, space limitations impose a drastic, and necessarily subjective, selection of topics and references. Thorough lists of references and a more complete picture (with, e.g., a description of the synthesis and characterization techniques) can be found in the excellent books devoted to the subject (Dresselhaus *et al.*, 1996, 2001; Endo *et al.*, 1996; Ebbesen, 1997; Saito *et al.*, 1998; Harris, 1999; Tománek and Enbody, 1999; Reich *et al.*, 2004; Loiseau *et al.*, 2006).

II. STRUCTURE OF CARBON NANOTUBES

Carbon nanotubes were discovered and first characterized in 1991 by Iijima from NEC laboratories (Japan) (Iijima, 1991). This discovery was made possible thanks to the use of state-of-the-art transmission microscopy. The first nanotubes discovered were made of several concentric cylindrical-like shells regularly spaced by an amount of about 3.4 Å as in conventional graphite materials (Fig. 1, left). These multiwall nanotubes (MWNTs) were first synthesized with diameters ranging from a few nanometers to several hundred nanometers for the inner and outer shells, respectively. As for the length, MWNTs extending over several microns are currently synthesized.

Shortly after the discovery of multiwall carbon nanotubes, single-wall carbon nanotubes (SWNTs) were synthesized in abundance using arc-discharge methods with transition-metal catalysts (Bethune *et al.*, 1993; Iijima and Ichihashi, 1993). A carbon nanotube made of a single graphite layer (the graphene sheet) rolled up into a hollow cylinder is called a single-wall nanotube. These tubes have quite small and uniform diameter, on the order of 1 nm$=10^{-9}$ m. This unprecedentedly small diameter, combined with the crystalline perfection of the atomic network, explains why these objects were quickly considered as the ultimate carbon-based 1D systems.

Crystalline ropes (or bundles) of SWNTs, with each rope containing tens to hundreds of tubes of similar diameter, closely packed in a hexagonal configuration, have also been synthesized using a laser vaporization method (Guo *et al.*, 1995) and arc-discharge and chemical vapor deposition (CVD) techniques (Fig. 1, right). Various synthesis methods have provided ample amounts of sufficiently characterized samples for studying the fundamental properties of SWNTs.

Because the microscopic structure of SWNTs is closely related to that of graphene, the tubes are usually labeled in terms of the graphene lattice vectors. As illustrated in Fig. 2 a single-wall carbon nanotube is geometrically obtained by rolling up a single graphene strip (Saito *et al.*, 1998). Its structure can be specified or indexed by its circumferential vector ($\mathbf{C}_h$), as defined by the chiral vector (AA' in Fig. 2) which connects two crystallographically equivalent sites (A and A') on a graphene sheet. In this way, a SWNT's geometry is completely specified by a pair of integers (n,m) denoting the relative position $\mathbf{C}_h = n\mathbf{a}_1 + m\mathbf{a}_2$ of the pair of atoms on a graphene strip which, when rolled onto each other, form a tube ($\mathbf{a}_1$ and $\mathbf{a}_2$ are unit vectors of the hexagonal honeycomb lattice; see Fig. 2).

This chiral vector $\mathbf{C}_h$ defines the circumference of the tube. The diameter d_t of the nanotube can thus be estimated from
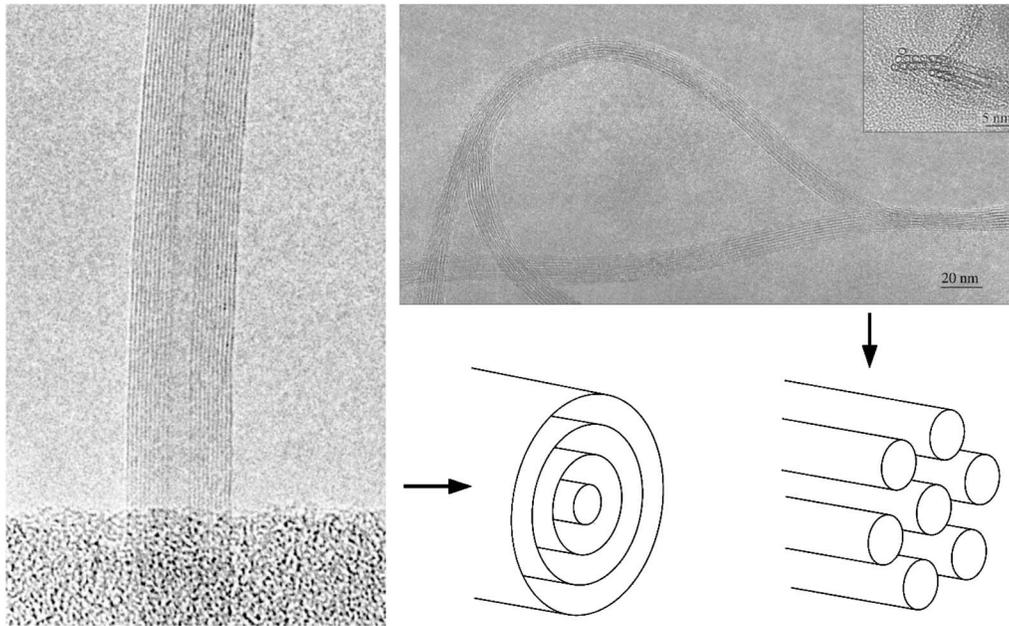
FIG. 1. High-resolution transmission electron microscopy pictures of a multiwall carbon nanotube (left) and a bundle of single-wall nanotubes (right), illustrating two different possible geometries for nanotubes. Courtesy of Gavillet, 2001.

$$d_t = |\mathbf{C}_h|/\pi = \frac{a}{\pi}\sqrt{n^2 + nm + m^2}, \qquad (1)$$

$$\cos\theta = \frac{\mathbf{C}_h \cdot \mathbf{a}_1}{|\mathbf{C}_h||\mathbf{a}_1|} = \frac{2n+m}{2\sqrt{n^2+nm+m^2}}. \qquad (2)$$

where a is the lattice constant of the honeycomb network: $a = \sqrt{3} \times a_{cc}$ ($a_{cc} \simeq 1.42$ Å, the C-C bond length). The chiral vector $\mathbf{C}_h$ uniquely defines a particular (n,m) tube, as well as its chiral angle θ, which is the angle between $\mathbf{C}_h$ and $\mathbf{a}_1$ (zigzag direction of the graphene sheet; see Fig. 2). The chiral angle θ can be calculated as follows:

The value of θ is in the range $0 \leqslant |\theta| \leqslant 30°$, because of the hexagonal symmetry of the graphene lattice. This chiral angle θ also denotes the tilt angle of the hexagons with respect to the direction of the nanotube axis. Nanotubes of the type $(n,0)$ ($\theta=0°$) are called zigzag tubes, because they exhibit a zigzag pattern along the circumference. Such tubes display carbon-carbon bonds parallel to the nanotube axis. Nanotubes of the type (n,n) ($\theta=30°$) are called armchair tubes, because they exhibit an armchair pattern along the circumference. Such tubes display carbon-carbon bonds perpendicular to the nanotube axis. Both zigzag and armchair nanotubes are achiral tubes, in contrast with general $(n, m \neq n \neq 0)$ chiral tubes (Fig. 3).

The geometry of the graphene lattice and the chiral vector determine not only the diameter of the tube, but also the unit cell and its number of carbon atoms. The smallest graphene lattice vector $\mathbf{T}$ perpendicular to $\mathbf{C}_h$
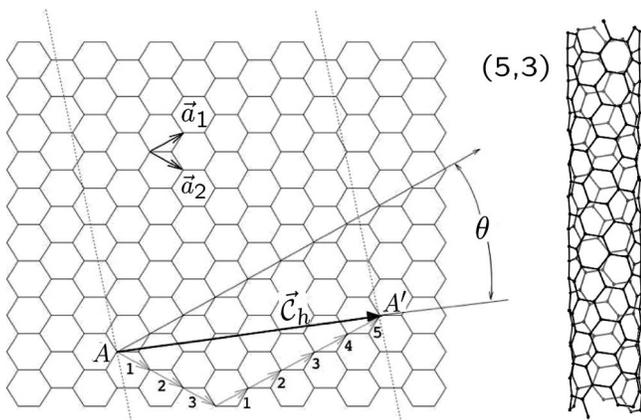
FIG. 2. Graphene honeycomb network with lattice vectors $\mathbf{a}_1$ and $\mathbf{a}_2$. The chiral vector $\mathbf{C}_h = 5\mathbf{a}_1 + 3\mathbf{a}_2$ represents a possible wrapping of the two-dimensional graphene sheet into a tubular form. The direction perpendicular to $\mathbf{C}_h$ is the tube axis. The chiral angle θ is defined by the $\mathbf{C}_h$ vector and the $\mathbf{a}_1$ zigzag direction of the graphene lattice. In the present example, a (5,3) nanotube is under construction and the resulting tube is illustrated on the right.

FIG. 3. Atomic structures of (12,0) zigzag, (6,6) armchair, and (6,4) chiral nanotubes.

TABLE I. Structural parameters for a (n,m) carbon nanotube. In this table, n, m, t_1, t_2 are integers.

Symbol	Name	Formula	Value
a	lattice constant	$a = \sqrt{3}a_{cc} \simeq 2.46$ Å	$a_{cc} \simeq 1.42$ Å
$\mathbf{a}_1$, $\mathbf{a}_2$	basis vectors	$\left(\dfrac{\sqrt{3}}{2}; \dfrac{1}{2}\right)a, \left(\dfrac{\sqrt{3}}{2}; -\dfrac{1}{2}\right)a$	
$\mathbf{b}_1$, $\mathbf{b}_2$	reciprocal-lattice vectors	$\left(\dfrac{1}{\sqrt{3}}; 1\right)\dfrac{2\pi}{a}, \left(\dfrac{1}{\sqrt{3}}; -1\right)\dfrac{2\pi}{a}$	
$\mathbf{C}_h$	chiral vector	$\mathbf{C}_h = n\mathbf{a}_1 + m\mathbf{a}_2 \equiv (n,m)$	$(0 \leq |m| \leq n)$
d_t	tube diameter	$d_t = \dfrac{|\mathbf{C}_h|}{\pi} = \dfrac{a}{\pi}\sqrt{n^2 + nm + m^2}$	
θ	chiral angle	$\sin\theta = \dfrac{\sqrt{3}m}{2\sqrt{n^2 + nm + m^2}}$	$0 \leq |\theta| \leq \dfrac{\pi}{6}$
		$\cos\theta = \dfrac{2n+m}{2\sqrt{n^2 + nm + m^2}}$	$\tan\theta = \dfrac{\sqrt{3}m}{2n+m}$
$\mathbf{T}$	translational vector	$\mathbf{T} = t_1\mathbf{a}_1 + t_2\mathbf{a}_2 \equiv (t_1, t_2)$	$\gcd(t_1, t_2) = 1$[a]
		$t_1 = \dfrac{2m+n}{N_R}, \ t_2 = -\dfrac{2n+m}{N_R}$	$N_R = \gcd(2m+n, 2n+m)$[a]
N_C	number of C atoms per unit cell	$N_C = \dfrac{4(n^2 + nm + m^2)}{N_R}$	

[a]$\gcd(n,m)$ denotes the greatest common divisor of the two integers n and m.

defines the translational period t along the tube axis. The lattice vector $\mathbf{T}$ can also be expressed in terms of the basis vectors $\mathbf{a}_1$ and $\mathbf{a}_2$ as $\mathbf{T} = t_1\mathbf{a}_1 + t_2\mathbf{a}_2$. Using $\mathbf{C}_h \cdot \mathbf{T} = 0$, the expressions for t_1 and t_2 are given by

$$t_1 = \frac{2m+n}{N_R}, \quad t_2 = -\frac{2n+m}{N_R}, \tag{3}$$

where N_R is the greatest common divisor of $(2m+n)$ and $(2n+m)$. The length of the translational vector t is given by

$$t = |\mathbf{T}| = \sqrt{3}a\sqrt{n^2 + nm + m^2}/N_R. \tag{4}$$

The nanotube unit cell is thus formed by a cylindrical surface with height t and diameter d_t. The number of carbon atoms per unit cell N_C can also be expressed as a function of n and m:

$$N_C = 4(n^2 + nm + m^2)/N_R. \tag{5}$$

The symmetry of carbon nanotubes can be described by the so-called line groups, which are full space groups of one-dimensional systems including translations in addition to the point-group symmetries like rotations or reflections. The carbon-nanotube line groups are nonsymmorphic groups as they always contain a screw axis. Every (n,m) carbon nanotube belongs to a different line group (Damnjanović *et al.*, 1999; Reich *et al.*, 2004). Only

armchair (n,n) and zigzag $(n,0)$ tubes with the same n belong to the same symmetry group. Moreover, by starting with a single carbon atom and successively applying all symmetry operations of the line group, the whole tube is constructed. However, for many applications, such as optical transitions or first-order Raman scattering, it is not necessary to work with the full line group, the point group being quite sufficient. These point groups are D_q for chiral nanotubes $(n, m \neq n \neq 0)$ and D_{2nh} for achiral tubes such as (n,n) or $(n,0)$. After the symmetry operations of the nanotube have been determined using its point group and its most basic structural properties (diameter, chirality, lattice, and reciprocal lattice vectors, as summarized in Table I), the corresponding graphene strip can be constructed and rolled up into a cylinder. The next step is now to predict its electronic behavior.

III. ELECTRONIC PROPERTIES OF CARBON NANOTUBES

Carbon nanotubes are characterized by two types of bond, in analogy with graphene, which exhibits so-called planar sp^2 hybridization. Among the four valence orbitals of the carbon atom (the $2s$, $2p_x$, $2p_y$, and $2p_z$ orbitals, $\hat{z}$ perpendicular to the sheet), the (s, p_x, p_y) orbitals combine to form in-plane σ (bonding or occupied) and σ^*
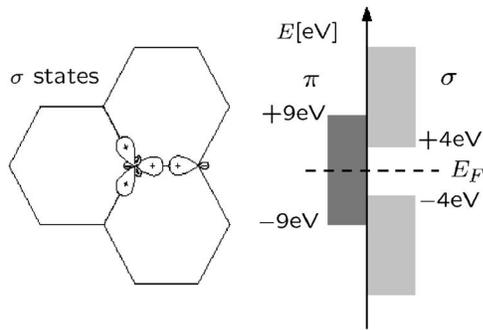
FIG. 4. The σ bonds in the carbon hexagonal network connect the carbon atoms and are responsible for the binding energy and the elastic properties of the graphene sheet (left). The π bonds are perpendicular to the surface of the sheet. The corresponding bonding and antibonding σ bands are separated by a large energy gap (right), while the bonding and antibonding π states lie in the vicinity of the Fermi level (E_F). Adapted from Loiseau *et al.*, 2006.

(antibonding or unoccupied) orbitals (Fig. 4). Such orbitals are even with respect to planar symmetry. The σ bonds are strong covalent bonds responsible for most of the binding energy and elastic properties of the graphene sheet. The remaining p_z orbital, pointing out of the graphene sheet, is odd with respect to the planar symmetry and cannot couple with the σ states. The lateral interaction with neighboring p_z orbitals (labeled the $pp\pi$ interaction) creates delocalized π (bonding) and π^* (antibonding) orbitals. In analogy, the σ bonds in the nanotube form a hexagonal network which strongly connects the carbon atoms in the cylinder wall of the tube. The π bonds are perpendicular to the surface of the nanotube and are responsible for the weak interaction between SWNTs in a bundle, similar to the weak interaction between carbon layers in pure graphite (Charlier *et al.*, 1991). The energy levels associated with the in-plane σ bonds are known to be far away from the Fermi energy in graphite (Fig. 4, right) and thus do not play a key role in its electronic properties. In contrast, the bonding and antibonding π bands cross the Fermi level

at high-symmetry points in the Brillouin zone of graphene (Wallace, 1947). For a good understanding of the electronic properties of SWNTs, the electronic structure of graphene will be briefly discussed in the next section.

A. From graphite to nanotubes

Although graphite has been studied for decades, graphene was only isolated experimentally in 2004 after a long struggle (Novoselov *et al.*, 2004). Further, and despite early predictions (Wallace, 1947), its remarkable conducting properties, in which electrons mimic the behavior of massless, relativistic particles, have only been observed recently (Novoselov *et al.*, 2005; Zhang *et al.*, 2005).

The electronic bands of graphene along the high-symmetry M-Γ-K directions are presented in Fig. 5. The π and π^* bands cross at the vertices of the hexagonal Brillouin zone (Fig. 6). Such vertices are labeled by their momentum vector usually written as K. Consequently, graphene is a special semimetal whose Fermi surface is reduced to the six distinct K points of the hexagonal Brillouin zone. Close to the Fermi energy, the π and π^* bands are nearly linear, in contrast with the quadratic energy-momentum relation obeyed by electrons at band edges in conventional semiconductors. This linear energy-momentum relation of electrons will explain the extremely good conductivity in graphene and bears much importance in the Luttinger-liquid (LL) behavior for low-energy excitations in nanotubes (see Sec. IV.E.3).

The bonding and antibonding σ bands are well separated in energy (>10 eV at Γ). These bands are frequently neglected in semiempirical calculations as they are too far away from the Fermi level to play a role in the electronic properties of graphene. The remaining two π bands can be simply described with a rather simple tight-binding Hamiltonian, leading to analytical solutions for their energy dispersion and the related eigenstates. This simple approach can be further ex-
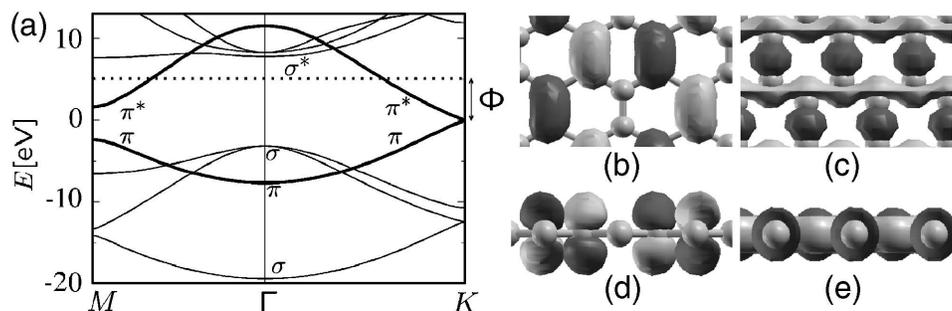
FIG. 5. Electronic properties of graphene. (a) Electronic band structure of graphene. The bonding σ and antibonding σ^* bands are separated by a large energy gap. The bonding π (last valence) band and antibonding π^* (first conduction) band cross at the K points of the Brillouin zone. The Fermi energy is set to zero, and ϕ indicates the work function. Above the vaccum level (dotted horizontal line), the states of the continuum are difficult to describe and merge with the σ^* bands. (b),(d) π state at K and (c),(e) σ state at Γ, seen from above and from the side of the graphene plane. Note that the π wave function cancels on a hexagonal sublattice due to the $\exp(i\mathbf{K}\cdot\mathbf{r})$ phase factor. The π (σ) state is odd (even) with respect to the graphene plane reflection. Courtesy of Fernández-Serra, 2006.

(a)

(b)

$$|\vec{a}_1| = |\vec{a}_2| = \sqrt{3}a_{cc}$$

$$\vec{a}_1 = \sqrt{3}a_{cc}\left(\frac{\sqrt{3}}{2}, \frac{1}{2}\right)$$

$$\vec{a}_2 = \sqrt{3}a_{cc}\left(\frac{\sqrt{3}}{2}, -\frac{1}{2}\right)$$

$$\vec{C}_h = 3\vec{a}_1 - 2\vec{a}_2$$
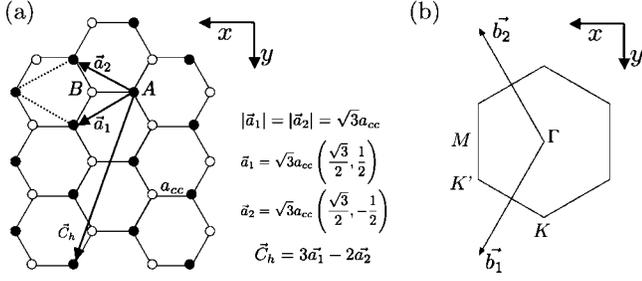
FIG. 6. Brillouin zone and reciprocal space. (a) Basis vectors in the hexagonal lattice of graphene. (b) Brillouin zone. The corresponding reciprocal basis vectors read $\mathbf{b}_1 = b(1/2, \sqrt{3}/2)$ and $\mathbf{b}_2 = b(1/2, -\sqrt{3}/2)$, with $b = 4\pi/a\sqrt{3}$.

tended to study the properties of nanotubes by combining these analytic results with the requirement that the wave functions in tubes must satisfy the proper boundary conditions around the tube circumference. This is what we show in the next sections.

B. Tight-binding model of graphene

As mentioned in the previous section, the graphene plane is a hexagonal lattice with two atoms per unit cell (A and B) and a basis defined by vectors ($\mathbf{a}_1, \mathbf{a}_2$) (see Fig. 6). The condition $\mathbf{a}_i \cdot \mathbf{b}_j = 2\pi\delta_{ij}$ allows one to obtain the reciprocal-lattice vectors ($\mathbf{b}_1, \mathbf{b}_2$). Every carbon atom possesses four valence electrons (two $2s$ and two $2p$ electrons). When the atoms are placed onto the graphene hexagonal lattice, as in Fig. 6, the electronic wave functions from different atoms overlap. However, such an overlap between the p_z orbitals and the s or p_x and p_y electrons is strictly zero by symmetry. Consequently, the p_z electrons, which form the π bonds in graphene, can be treated independently of other valence electrons. Within this π-band approximation, the A atom (B atom) is uniquely defined by one orbital per atom site $p_z(\mathbf{r} - \mathbf{r}_A)$ [$p_z(\mathbf{r} - \mathbf{r}_B)$].

To derive the electronic spectrum of the total Hamiltonian, the corresponding Schrödinger equation has to be solved, and by applying the Bloch theorem, the wave functions can be written as follows:

$$\Psi(\mathbf{k}, \mathbf{r}) = c_A(\mathbf{k})\tilde{p}_z^A(\mathbf{k}, \mathbf{r}) + c_B(\mathbf{k})\tilde{p}_z^B(\mathbf{k}, \mathbf{r}), \tag{6}$$

with

$$\tilde{p}_z^A(\mathbf{k}, \mathbf{r}) = \frac{1}{\sqrt{N_{\text{cells}}}}\sum_{\ell} e^{i\mathbf{k}\cdot\ell} p_z(\mathbf{r} - \mathbf{r}_A - \ell), \tag{7}$$

$$\tilde{p}_z^B(\mathbf{k}, \mathbf{r}) = \frac{1}{\sqrt{N_{\text{cells}}}}\sum_{\ell} e^{i\mathbf{k}\cdot\ell} p_z(\mathbf{r} - \mathbf{r}_B - \ell), \tag{8}$$

where $\mathbf{k}$ is the electron momentum (the quantum number), N_{cells} is the number of unit cells in the graphene sheet, and ℓ is the cell position index. The spectrum is derived by solving the Schrödinger equation which reduces to a 2×2 matrix diagonalization:

$$\begin{pmatrix} \mathcal{H}_{AA} - E & \mathcal{H}_{AB} \\ \mathcal{H}_{BA} & \mathcal{H}_{BB} - E \end{pmatrix}, \tag{9}$$

where the matrix elements are defined as

$$\mathcal{H}_{AA}(\mathbf{k}) = \frac{1}{N_{\text{cells}}}\sum_{\ell,\ell'} e^{i\mathbf{k}\cdot(\ell'-\ell)}\langle p_z^{A,\ell}|\mathcal{H}|p_z^{A,\ell'}\rangle, \tag{10}$$

$$\mathcal{H}_{AB}(\mathbf{k}) = \frac{1}{N_{\text{cells}}}\sum_{\ell,\ell'} e^{i\mathbf{k}\cdot(\ell'-\ell)}\langle p_z^{A,\ell}|\mathcal{H}|p_z^{B,\ell'}\rangle, \tag{11}$$

with the notation $p_z^{A/B,\tau} = p_z(\mathbf{r} - \mathbf{r}_{A/B} - \tau)$. Here we have neglected the overlap matrix elements $S = \langle \tilde{p}_z^A|\tilde{p}_z^B\rangle$ between neighboring $\tilde{p}_z$ orbitals (neglect of overlap integrals defines the so-called orthogonal tight-binding schemes). After simple manipulations and restricting interactions to first nearest neighbors only, one gets

$$\mathcal{H}_{AB}(\mathbf{k}) = \langle p_z^{A,0}|\mathcal{H}|p_z^{B,0}\rangle + e^{-i\mathbf{k}\cdot\mathbf{a}_1}\langle p_z^{A,0}|\mathcal{H}|p_z^{B,-\mathbf{a}_1}\rangle$$
$$+ e^{-i\mathbf{k}\cdot\mathbf{a}_2}\langle p_z^{A,0}|\mathcal{H}|p_z^{B,-\mathbf{a}_2}\rangle = -\gamma_0\alpha(\mathbf{k}), \tag{12}$$

with γ_0 the transfer integral between first-neighbor π orbitals (a typical value for γ_0 is 2.9 eV), $\alpha(\mathbf{k}) = (1 + e^{-i\mathbf{k}\cdot\mathbf{a}_1} + e^{-i\mathbf{k}\cdot\mathbf{a}_2})$, and $\langle p_z^{A,0}|\mathcal{H}|p_z^{A,0}\rangle = \langle p_z^{B,0}|\mathcal{H}|p_z^{B,0}\rangle = 0$ as the energy reference. The dispersion relations are then readily obtained:

$$E^{\pm}(\mathbf{k}) = \pm\gamma_0\sqrt{3 + 2\cos(\mathbf{k}\cdot\mathbf{a}_1) + 2\cos(\mathbf{k}\cdot\mathbf{a}_2) + 2\cos[\mathbf{k}\cdot(\mathbf{a}_2 - \mathbf{a}_1)]}, \tag{13}$$

which can be further developed as

$$E^{\pm}(k_x, k_y) = \pm\gamma_0\sqrt{1 + 4\cos\frac{\sqrt{3}k_xa}{2}\cos\frac{k_ya}{2} + 4\cos^2\frac{k_ya}{2}} \tag{14}$$

by setting $a = \sqrt{3}a_{cc}$ ($a_{cc} = 1.42$ Å). The $\mathbf{k} = (k_x, k_y)$ vectors that belong to the first hexagonal Brillouin zone (BZ)

constitute an ensemble of available electronic momenta. In Fig. 7, these simple tight-binding dispersion relations are represented with dashed lines along high symmetry directions of the BZ, defined by the Γ and M points together with the six BZ vertices (K points).

With one p_z electron per atom in the π-π^* model (the three other s, p_x, and p_y electrons fill the low-lying σ band), the $(-)$ band (negative energy branch) in Eq. (14)
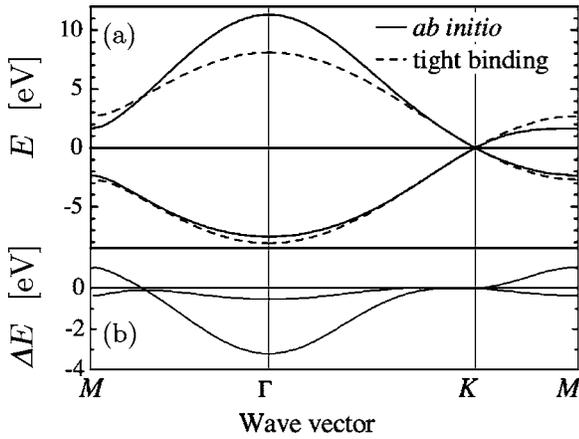
FIG. 7. Limitations of the π-π^* model. (a) *Ab initio* (solid lines) and nearest-neighbor orthogonal tight-binding [dashed lines, from Eq. (14)] π and π^* electronic bands for graphene. (b) Difference ΔE between the *ab initio* and tight-binding band structures. Adapted from Reich, Maultzsch, Thomsen, and Ordejón, 2002.

is fully occupied, while the ($+$) branch is empty. These occupied and unoccupied bands cross at the K points [one verifies that $\alpha(\mathbf{k}=K)=0$]. The Fermi level E_F (or charge-neutrality point) is therefore the zero-energy reference in Fig. 7, and the Fermi surface is defined by the set of K points. Since the occupied and unoccupied bands do cross, the graphene sheet displays a metallic (zero-gap) character. However, as the Fermi surface is of zero dimension (since it is reduced to a discrete and finite set of points), the term semimetal is usually used.

This simple orthogonal tight-binding model yields π and π^* zone-center Γ energies which are symmetric ($\pm\gamma_0$) with respect to E_F. In fact, the antibonding (unoccupied) π^* bands are located at a higher energy if the overlap integral S is not set to zero (see Fig. 7). A better, but more complicated, π-π^* parametrization can be found in Reich, Maultzsch, Thomsen, and Ordejón (2002) where a careful comparison between *ab initio* and various tight-binding schemes is presented for graphene and several nanotubes. The main advantage of the present nearest-neighbor approximation is the very simple analytical expression for the π electronic states of graphene.

C. Zone-folding approximation

Due to periodic boundary conditions along the circumferential direction of the tube, the allowed wave vectors "around" the nanotube circumference are quantized: they can take only a set of discrete values. In contrast, the wave vectors along the nanotube axis remain continuous (for infinite tubes). Plotting these allowed vectors for a given nanotube onto the Brillouin zone of graphene generates a series of parallel lines. The length, number, and orientation of these cutting lines depend on the chiral indices (n,m) of the nanotube. The basic idea behind the zone-folding approximation is that the elec-

tronic band structure of a specific nanotube is given by superposition of the graphene electronic energy bands along the corresponding allowed $\mathbf{k}$ lines. This is what we explain now.

A specific carbon nanotube defines a unique chiral vector $\mathbf{C}_h=(n,m)$ expressed in the basis ($\mathbf{a}_1,\mathbf{a}_2$) (Fig. 2) that fixes its symmetry and its diameter. As mentioned in Sec. II, the chiral vector length $|\mathbf{C}_h|$ equals $\sqrt{3}a_{cc}\sqrt{n^2+nm+m^2}$ or πd_t (d_t being the nanotube diameter). The application of periodic boundary conditions around the tube circumference leads to some restrictions on the allowed wave function quantum phase:

$$\Psi_{\mathbf{k}}(\mathbf{r}+\mathbf{C}_h)=e^{i\mathbf{k}\cdot\mathbf{C}_h}\Psi_{\mathbf{k}}(\mathbf{r})=\Psi_{\mathbf{k}}(\mathbf{r}), \tag{15}$$

with the vectors $\mathbf{r}$ and $\mathbf{k}$ taken on the tube surface. The first equality stems from the Bloch theorem. Depending on the tube symmetry, that is, on the chiral vector $\mathbf{C}_h=(n,m)$, two situations can occur.

1. Metallic nanotubes

We make an analysis in the neighborhood of the Fermi surface, so that we write $\mathbf{k}=\mathbf{K}+\delta\mathbf{k}$, with $\delta\mathbf{k}$ small, taking, e.g., $\mathbf{K}=(\mathbf{b}_1-\mathbf{b}_2)/3=(0,4\pi/3a)$, so that $\mathbf{k}=(\delta k_x,4\pi/3a+\delta k_y)$. When $e^{i\mathbf{K}\cdot\mathbf{C}_h}=1$ (which is possible only when $n-m=3l$, with l an integer), then the constraint on the wave function becomes $\delta\mathbf{k}\cdot\mathbf{C}_h=2\pi q$ (q integer). Each index q defines a line of allowed $\mathbf{k}$ vectors, and each line contributes to one occupied π band and one unoccupied π^* band. The condition $n-m=3l$ is always satisfied for armchair tubes and for the subset of the $(n,0)$ zigzag tubes with n multiples of 3. Rewriting the dispersion relation in the general case as $E^2(k_x,k_y)=\gamma_0^2|\alpha|^2$ and performing a second-order perturbation expansion in the vicinity of the $\mathbf{K}$ points, one finally obtains $|\alpha(k_x,k_y)|^2\simeq\frac{3}{4}(\delta k_x^2+\delta k_y^2)+O(\delta k^3)$ (with δk_x and δk_y related by $\delta\mathbf{k}\cdot\mathbf{C}_h=2\pi q$). Close to E_F, the dispersion relation then reads $E^{\pm}(\delta\mathbf{k})\simeq\pm(\sqrt{3}a/2)\gamma_0\|\delta\mathbf{k}\|$, a linear energy-momentum relation mentioned above. Therefore, states arbitrarily close in energy to the Fermi level can be found for $q=0$ and the system is metallic (see Fig. 8). The Fermi velocity $v_F=\sqrt{3}a\gamma_0/2\hbar=\frac{3}{2}a_{cc}\gamma_0/\hbar$ is typically given by $v_F\simeq8\times10^5$ m s^{-1} for $\gamma_0=2.9$ eV. The linear band dispersion close to E_F will be shown to have useful consequences.

A simple expression for the eigenstates can also be derived close to E_F within the same type of approximation. Such an expression will be used in Sec. IV.C.2 to show that elastic backscattering is quenched in nanotubes if the disorder is long ranged. One notes that, for a general helical symmetry, the full properties of the eigenstates can be derived by constructing generalized Bloch states satisfying helical (rototranslation) symmetries (Mintmire *et al.*, 1992).

2. Semiconducting nanotubes

The second possible choice for (n,m) nanotubes is given by the condition $n-m=3l\pm1$. In this situation
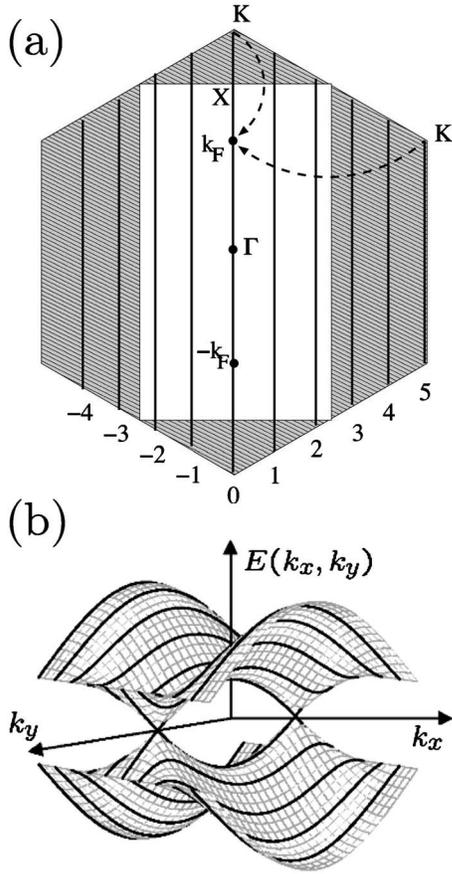
FIG. 8. The band-folding scheme. (a) Brillouin zone of graphene. The white rectangle is the Brillouin zone associated with the four-atom cell with lattice vectors $\mathbf{C}_h/\mathrm{n}=\mathbf{a}_1+\mathbf{a}_2$ and $\mathbf{T}$ ($\mathbf{T}=\mathbf{a}_1-\mathbf{a}_2$ for an armchair tube). Thick lines are the allowed $\mathbf{k}$ lines for the (5,5) armchair tube. To obtain the (5,5) band structure in the band-folding approach, fold the colored corners onto the rectangular cell and superimpose the graphene energy bands calculated along the obtained thick lines of length $2\pi/|\mathbf{T}|$. In particular, the $\mathbf{K}$ points are folded at two-thirds of ΓX (or its inversion symmetry image). The bands are indexed by the integer q such that $\mathbf{k}\cdot\mathbf{C}_h=2\pi q$. In the corresponding (5,5) tube, q is also the azimuthal quantum number. (b) Dispersion relations $E^{\pm}(k_x,k_y)$ for the graphene plane, together with that of an armchair nanotube (bold line).

$e^{i\mathbf{K}\cdot\mathbf{C}_h}=\pm e^{2i\pi/3}$, and one gets $\delta\mathbf{k}=(2\pi/|\mathbf{C}_h|)(q\pm1/3)\kappa_{\perp}+k_{\parallel}\kappa_{\parallel}$ with $\kappa_{\perp}$ and $\kappa_{\parallel}$ the basis vectors along the $\mathbf{C}_h$ and $\mathbf{T}$ directions, respectively, where $\mathbf{T}$ is the translational vector along the tube axis, as defined in Sec. II. By following a similar calculation as for the prior case, one obtains in the vicinity of the Fermi level a new dispersion relation, namely,

$$E_q^{\pm}(k_{\parallel}) \simeq \pm \frac{\sqrt{3}a}{2}\gamma_0 \sqrt{\left(\frac{2\pi}{|\mathbf{C}_h|}\right)^2\left(q\pm\frac{1}{3}\right)^2+k_{\parallel}^2}, \qquad (16)$$

where the integer variable q counts the available bands, whereas $k_{\parallel}$ is the part of the wave vector that continuously describes the states within a given subband (and associated with the direction parallel to the tube axis).
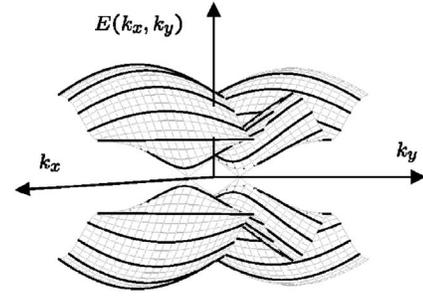
FIG. 9. Dispersion relations $E_{\pm}(k_x,k_y)$ for the graphene plane, together with that of a zigzag semiconducting nanotube (bold line).

This case leads to an obvious gap opening at the Fermi level (Fig. 9) since

$$E_{q=0}^{+}(k_{\parallel}=0) - E_{q=0}^{-}(k_{\parallel}=0) = \frac{2\pi a\gamma_0}{\sqrt{3}|\mathbf{C}_h|} = \Delta E_g^1. \qquad (17)$$

It appears that ΔE_g^1 decreases as the inverse of the tube diameter d_t ($d_t=|\mathbf{C}_h|/\pi$). For a very large diameter, one finds as expected a zero-gap semiconductor since we recover the graphene sheet. For realistic tubes, with, e.g., a diameter of 1.4 nm [helical vector (17,0)], one gets $\Delta E_g^1 \simeq 0.59$ eV. This $1/d$ dependence of the gap on the diameter relies on the assumption of a linear dispersion of the bands around E_F, a result first derived by White and Mintmire (1998). In reality, the bands are not linear away from E_F, an effect called trigonal warping (Saito, Dresselhaus, and Dresselhaus, 2000) which induces a dependence of the band gap not only on the diameter, but on the (n,m) indices as well.

In relation to the study of transport properties an important quantity linked to the dispersion relation is the so-called effective mass of the charge carriers. In semiconducting nanotubes, this quantity can be derived from Eq. (16),

$$E_{q=0}^{\pm} = \pm \sqrt{(m^*v_F^2)^2+(\hbar k_{\parallel}v_F)^2},$$

defining $m^*=2\pi\hbar/3|C_h|v_F$, which is thus inversely proportional to the nanotube diameter and tends to zero as the diameter tends to infinity (graphene limit). This concept has been used (Zhou et al., 2005) to estimate the charge mobility properties in semiconducting nanotubes.

In summary, early theoretical calculations (Hamada et al., 1992; Mintmire et al., 1992; Saito et al., 1992) showed that the electronic properties of carbon nanotubes are very sensitive to their geometric structure. Although graphene is a semimetal, theory has predicted that carbon nanotubes can be metals or semiconductors with an energy gap that depends on the tube diameter and helicity, i.e., on the indices (n,m). These results can be simply understood within a band-folding picture, as illustrated in the present section. This approach is made relatively simple in nanotubes because of the special shape of the graphene Fermi surface and the restriction of the electronic bands to the π-π^* manifold.

When forming a tube, owing to the periodic boundary conditions imposed in the circumferential direction, only a certain set of **k** vectors in the graphene BZ are allowed. This allowed set of Bloch momenta depends on the diameter and helicity of the tube. Whenever the allowed **k** vectors include the point K, the system is a metal with a nonzero density of states at the Fermi level, resulting in a one-dimensional metal with two bands dispersing linearly close to E_F. When the K point is not included, the system is a semiconductor with a small band gap that depends mainly on the diameter. In this case, the conduction- and valence-band edges come from states with **k** vectors located on the allowed line(s) closest to the K point.

Within the zone-folding approximation, the general rules for the metallicity of single-wall carbon nanotubes are as follows: a nanotube defined by the (n,m) indices will be metallic (semiconductor) if $n-m=3l$, with l an integer $(n-m=3l\pm1)$. Consequently, most carbon nanotubes are semiconductors and only a fraction $(1/3)$ are metallic (or semimetallic).

To conclude this subsection, we note that the index q, as defined above by the condition $\mathbf{k}\cdot\mathbf{C}_h=2\pi q$ [Eq. (15)] is also the azimuthal quantum number associated with the states on the corresponding allowed **k** line. This quantum number therefore characterizes the behavior of eigenstates with respect to rotations around the axis that transform the tube into itself. It can be used in particular to study, on the basis of symmetry-related selection rules (Vucović *et al.*, 2002), the effect of a perturbation on various subbands and their mixing upon static (e.g., tube squashing, interaction with a substrate, etc.) or time-dependent (e.g., optical excitation) perturbations.

D. Band structures and densities of states

As the nanotubes are one dimensional, their Brillouin zone is one dimensional as well, with zone edges usually labeled X, namely, $\mathbf{X}=\pm(\pi/T)\boldsymbol{\kappa}_\parallel$, with $\boldsymbol{\kappa}_\parallel$ and **T** defined above. The nanotube band structure is therefore represented along the ΓX direction ($\Gamma X'$ with $X'=-X$ symmetric by time reversal). In the band-folding approach, one obtains therefore a superposition of all allowed $E_q^\pm(k_\parallel)$ graphene eigenvalues, with q the allowed line index (two bands per line) and $k_\parallel$ the continuous momentum along $\boldsymbol{\kappa}_\parallel$ (from now on, as there is only one direction, we drop the $\parallel$ subscript and write $k_\parallel=k$). One says that the allowed **k** lines are "folded" onto the ΓX direction [see Fig. 8(a) for armchair tubes]. We now study the band structure and related density of states of (n,m) tubes as given by the band folding of the π-π^* bands of graphene within the orthogonal tight-binding scheme presented above.

The electronic band structure of an armchair (5,5) carbon nanotube is presented in Fig. 10. Six bands for the conduction and an equal number for the valence states are observable. However, four of them are degenerate, leading to ten electronic levels in each case, consistent
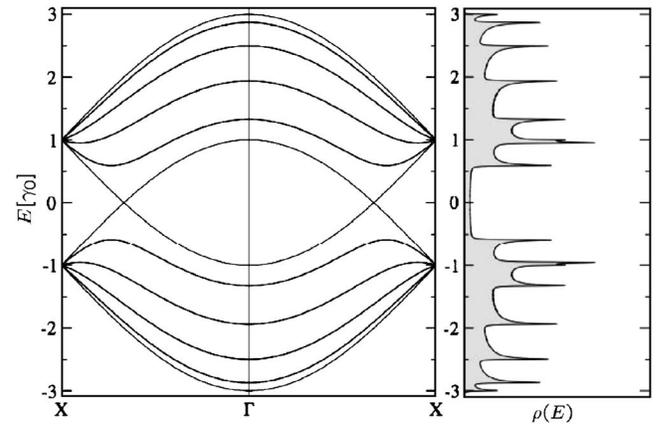
FIG. 10. Band structure and density of states for a (5, 5) armchair nanotube within the zone-folding model. The 1D energy dispersion relations are presented in the $[-3\gamma_0;3\gamma_0]$ energy interval in dimensionless units (γ_0 being the nearest-neighbor C-C tight-binding overlap energy ~2.9 eV). The energy bands are plotted along the X-Γ-X direction. The Fermi level is located at zero energy.

with the ten hexagons around the circumference of the (5,5) nanotube. Indeed, the bands coming from two allowed lines with opposite q index, for $q=\pm1$ to $q=\pm4$ [see Fig. 8(a)], are degenerate by symmetry. For all armchair nanotubes, the energy bands exhibit a large degeneracy at the zone boundary, where $k=\pm\pi/a$ (X point), so that Eq. (14) becomes $E(k=\pm\pi/a)=\pm\gamma_0$. This comes from the absence of dispersion along the segments connecting the neighboring centers of the BZ sides (the M points), an effect that will yield the so-called trigonal warping of the bands as discussed below. The valence and conduction bands for armchair nanotubes cross at $k=k_F=\pm2\pi/(3a)$, a point that is located at two-thirds of ΓX [Fig. 8(a)]. This means that the original **K** vertices of the original graphene hexagonal BZ are folded at two-thirds of the ΓX line (or its inversion symmetry image). As discussed above, the (5,5) armchair nanotube is thus a zero-gap semiconductor which will exhibit metallic conduction at finite temperatures, since only infinitesimal excitations are needed to promote carriers into the conduction bands.

The density of states (DOS) $\Delta N/\Delta E$ represents the number of available states ΔN for a given energy interval ΔE ($\Delta E\to0$). This DOS is a quantity that can be measured experimentally under some approximations. The shape of the density of states is known to depend dramatically on dimensionality. In 1D, as shown below, the density of states diverges as the inverse of the square root of the energy $(1/\sqrt{E})$ close to band extrema. These "spikes" in the DOS are called Van Hove singularities (VHSs) and manifest the confinement properties in directions perpendicular to the tube axis. As carbon nanotubes are one dimensional, their corresponding DOSs exhibit such a spiky behavior at energies close to band edges (see Fig. 10). The position of these Van Hove singularities can be analytically derived from the dispersion relations. The density of states is defined by

$$\rho(E) = \frac{1}{\Omega} \text{Tr}[\delta(E - \mathcal{H})], \qquad (18)$$

where $\delta(E - \mathcal{H})$ is the spectral measure; the trace is expanded within a complete basis, and Ω is the volume of the considered system. For the set of eigenvalues $E_q^s(k)$, where $s = \pm$ refers to the sign of the solution in Eq. (14), the DOS can be expressed as

$$\rho(E) = \frac{2}{\Omega} \sum_q \sum_{s=\pm} \int dk\, \delta(E - E_q^s(k))$$

$$= \frac{2}{\Omega} \sum_q \sum_{s=\pm} \int dk\, \delta(k - k_{qs}) \left| \frac{\partial E_q^s(k)}{\partial k} \right|^{-1}, \qquad (19)$$

where k_{qs} are the roots of the equation $E - E_q^s(k) = 0$, while $\Omega = 4\pi|\mathbf{C}_h|/\sqrt{3}a^2$ is the volume (surface) of the reciprocal space for each allowed state divided by the distance between allowed lines in the graphene Brillouin zone (see above). In the vicinity of $\mathbf{K}$, where one can use the linear energy-momentum relation, the contribution of $\mathbf{k}$ to the density of states is related to

$$\left| \frac{\partial E_q^s(k)}{\partial k} \right|^{-1} = \frac{2}{\sqrt{3}\,\gamma_0 a} \frac{|E_q^s(k)|}{\sqrt{(E_q^s)^2(k) - \varepsilon_{qs}^2}}, \qquad (20)$$

where ε_{qs} gives the energy position of the Van Hove singularities. In the vicinity of E_F, those positions are given by $|\varepsilon_{qs}| = \sqrt{3}\gamma_0 a \Delta k_\perp^q / 2$ with $\Delta k_\perp^q = |(\mathbf{k} - \mathbf{K}) \cdot \mathbf{C}_h/|\mathbf{C}_h|| = 2\pi|3q - n + m|/3|\mathbf{C}_h|$. Hence $|\varepsilon_{qs}| = \pi \gamma_0 a_{cc}|3q - n + m|/|\mathbf{C}_h|$, and one finally obtains the density of states

$$\rho(E) = \frac{2a}{\pi \gamma_0 |\mathbf{C}_h|} \sum_{q=1}^{2n} \sum_{s=\pm} \frac{|E_q^s(k)|}{\sqrt{(E_q^s)^2(k) - \varepsilon_{qs}^2}}. \qquad (21)$$

For all metallic nanotubes, the density of states per unit length along the nanotube axis is a constant at the Fermi energy (E_F) and can be expressed analytically (Mintmire and White, 1998):

$$\rho(\varepsilon_F) = 2\sqrt{3}a_{cc}/(\pi \gamma_0 |\mathbf{C}_h|). \qquad (22)$$

Beyond the linear-band approximation, one can rewrite Eq. (14) for metallic armchair (n, n) nanotubes to obtain the following band dispersion relation:

$$E_q^\pm(k) = \pm \gamma_0 \sqrt{1 + 4 \cos \frac{ka}{2} \cos \frac{q\pi}{n} + 4 \cos^2 \frac{ka}{2}}, \qquad (23)$$

where $q = 1, 2n$ corresponds to the discrete part of the wave vector (band index) and k is the continuous part of the wave vector, describing states in a specific band ($-\pi < ka < \pi$). The positions of the Van Hove singularities can then be derived analytically directly from Eq. (23), and a simple calculation gives $\varepsilon_{q,s=\pm} = \pm \gamma_0 \sin q\pi/n$. In Fig. 10, the spikes in the DOS are localized at $\varepsilon_{q=1,10;s=\pm} = \pm \gamma_0 \sin q\pi/5$.

We now turn to zigzag tubes. The calculated 1D dispersion relations $E(k)$ for the (9,0) and (10,0) zigzag nanotubes are illustrated in Figs. 11 and 12, respectively. As expected, the (9,0) tube is metallic, with the Fermi surface located at Γ, whereas the (10,0) nanotube exhib-
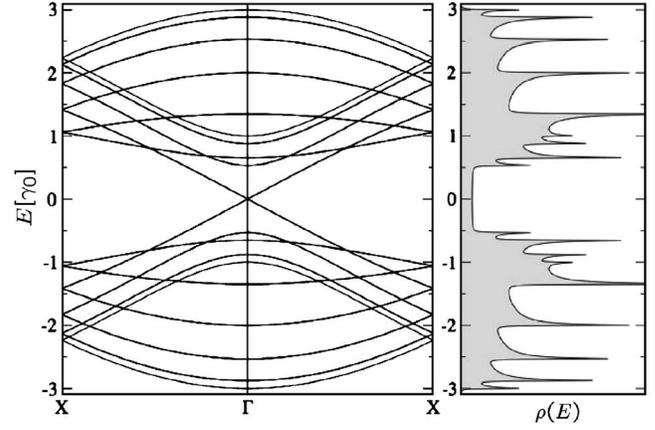
FIG. 11. Band structure and density of states for a (9, 0) zigzag nanotube within the zone-folding model. The Fermi level is located at zero energy.

its a finite energy gap at Γ. In particular, in the case of the (10,0) nanotube, there is a dispersionless energy band at $E/\gamma_0 = \pm 1$, which gives a singularity in the DOS at these particular energies. For a general $(n,0)$ zigzag nanotube, when n is a multiple of 3, the energy gap at $k = 0$ (Γ point) becomes zero. However, when n is *not* a multiple of 3, an energy gap opens at Γ. The corresponding densities of states have a zero value at the Fermi energy for the semiconducting nanotube and a small nonzero value for the metallic one.

It should be noted that the k values for the band crossing at E_F in metallic nanotubes are $k = \pm 2\pi/3T$ or $k = 0$ for armchair or zigzag tubes, respectively. These k values are also the locations of the band gaps for semiconducting zigzag nanotubes. The same k values denote as well the positions of the energy gaps (including zero energy gaps) for the general case of chiral nanotubes. In Fig. 13, the dispersion relations $E(k)$ for the (8,2) chiral nanotube are shown. Since $n - m$ is a multiple of 3, this nanotube exhibits a metallic behavior with a band crossing at $k = \pm 2\pi/3T$. Other chiral nanotubes, like the (9,6), display a zero energy gap at $k = 0$. The DOS of chiral
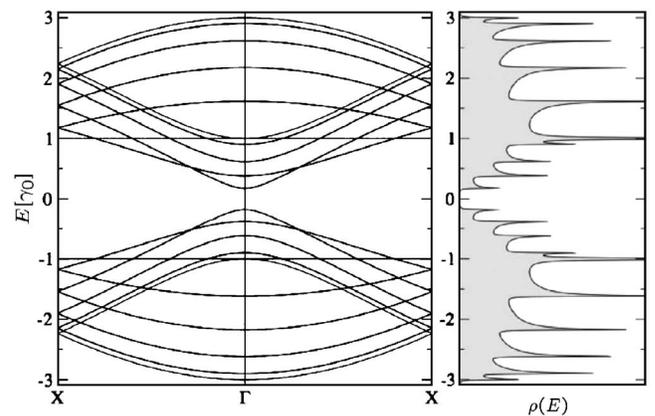
FIG. 12. Band structure and density of states for a (10,0) zigzag nanotube within the zone-folding model. The Fermi level is located at zero energy.
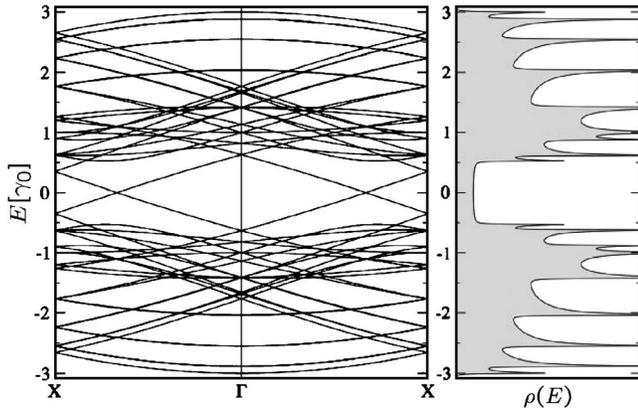
FIG. 13. Band structure and density of states for a (8,2) chiral nanotube within the zone-folding model. The Fermi level is located at zero energy.

nanotubes (see Fig. 13) also displays Van Hove singularities as for achiral tubes (Charlier and Lambin, 1998; Mintmire and White, 1998; White and Mintmire, 1998).

In semiconducting zigzag or chiral nanotubes, the band gap [as expressed by Eq. (17)] is independent of the chiral angle and varies inversely with the nanotube diameter: $\Delta E_g^1 = 2\gamma_0 a_{cc}/d_t$ (in the linear-band approximation). Density-of-states measurements by scanning tunneling spectroscopy (STS) provide a powerful tool for probing the electronic structure of carbon nanotubes. It can be shown, indeed, that under some assumptions the voltage-current derivative dI/dV is proportional to the DOS. These experiments (Odom et al., 1998; Wildöer et al., 1998) confirmed that the energy band gap of semiconducting tubes is roughly proportional to $1/d_t$ and that about 1/3 of nanotubes are conducting, while the other 2/3 are semiconducting. Resonances in the DOS have also been observed experimentally (Odom et al., 1998; Wildöer et al., 1998) on both metallic and semiconducting nanotubes whose diameters and chiral angles were determined using a scanning tunneling microscope (STM) (Venema et al., 2000). Several other experimental techniques, such as resonant Raman scattering (Jorio et al., 2001) and optical absorption and emission measurements (Bachilo et al., 2002; O'Connell et al., 2002; Lefebvre et al., 2003), have also confirmed this structure in Van Hove singularities of the electronic densities of states in single-wall carbon nanotubes.

E. Band structures in a magnetic field

The application of a uniform external magnetic field has profound consequences on the electronic band structure of carbon nanotubes. There exist two cases of high symmetry for the direction of the magnetic field with respect to the nanotube axis. When the magnetic field is applied parallel to the tube axis, electrons within the nanotube are influenced by the electromagnetic potential, whose dominating effect is to add a new phase factor to the quantum wave function (with subsequent modification of the associated momentum), and in the

cylinder geometry this phase factor will be driven in a periodic fashion by the magnetic flux threading the nanotube cross section. This quantum phenomenon was first described theoretically by Aharonov and Bohm (1959), whereas field-periodic oscillations of the magnetoresistance were experimentally measured in ordinary metallic rings (Webb et al., 1985), opening a new field for mesoscopic physics (Imry, 1997).

Given that the metallic or semiconducting character of carbon nanotubes results from the existence of the allowed momentum **k** at the **K** points of the hexagonal Brillouin zone, the superimposed Aharonov-Bohm phase factor, modulated by the field, will induce some field-dependent disruption of the initial eigenstate distribution in reciprocal space, with a first spectacular effect of the band gap opening for an initially metallic system, as first described by Ajiki and Ando (1993). In this section, we provide the basics for understanding the Aharonov-Bohm phenomenon in carbon nanotubes and its consequences on the electronic spectrum. In Sec. IV.D.1, its corresponding effects on transport properties will be further described.

1. Aharonov-Bohm quantum phase

To further deepen and illustrate these effects, let us describe the modifications of the quantum phase factor, driven by the vector potential **A** and associated with the external magnetic field $\mathbf{B}=B(u_x,u_y,u_z)$ (with $\mathbf{B}=\mathrm{rot}\mathbf{A}$). Within the tight-binding scheme, the Bloch functions in the static **B** can be written as

$$\Psi(\mathbf{k},\mathbf{r}) = \frac{1}{\sqrt{N}}\sum_{\mathbf{R}} e^{i\mathbf{k}\cdot\mathbf{R}} e^{i\varphi_R}\Phi(\mathbf{r}_R).$$

With **R** a lattice vector and φ_R the phase factor associated with the magnetic field, it can be shown that $\varphi_R(\mathbf{r}) = \int_{\mathbf{R}}^{\mathbf{r}}\mathbf{A}(\mathbf{r}')d\mathbf{r}' = \int_0^1(\mathbf{r}-R)\cdot\mathbf{A}(\mathbf{R}+\lambda[\mathbf{r}-\mathbf{R}])d\lambda$ (Luttinger, 1951), so that the total matrix elements of $\mathcal{H}=(\mathbf{p}/2m - e\mathbf{A})^2 + V(\mathbf{r})$, in the presence of **B**, are simply obtained through multiplication of those in the zero-field case by the phase factor (Saito et al., 1998). For a general description of the **B**-dependent band-structure effects, one possibility is to adopt the Cartesian basis $(\mathbf{e}_x,\mathbf{e}_y,\mathbf{e}_z)$ where $\mathbf{e}_z$ and $\mathbf{e}_x$ are, respectively, taken along and perpendicular to the tube axis. In the Landau gauge $\mathbf{A} = B(0,u_z x,u_x y)$, the Aharonov-Bohm phase acquired during an electronic motion between an orbital located at (x_i,y_i,z_i) and another located at (x_j,y_j,z_j) can be easily derived:

$$\varphi_{ij} = \frac{2\pi}{\phi_0}B\left[(y_j-y_i)u_z\frac{x_i+x_j}{2} + (z_j-z_i)u_x\frac{y_i+y_j}{2}\right], \quad (24)$$

where ϕ_0 is the quantum flux. This result is applicable whatever the direction of **B** with respect to the tube axis and gives the axial configuration for $(u_x=0,u_z=1)$ and the perpendicular configuration for $(u_x=1,u_z=0)$. This further allows us to compute the remormalized field-dependent coupling overlap between π orbitals, $\gamma_{ij}(\mathbf{B})$
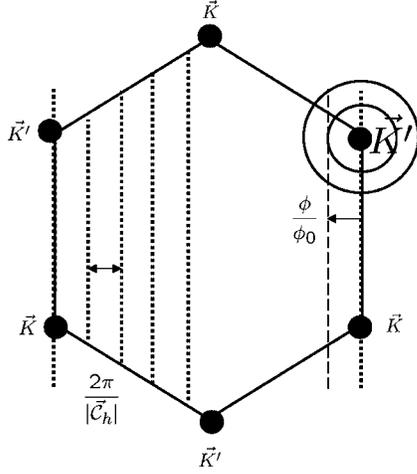
FIG. 14. Representation of the first Brillouin zone of a graphene sheet together with allowed states for an armchair tube (dashed lines) at zero flux. Modifications of allowed states in the vicinity of **k** points, under the effect of a magnetic field applied parallel to the tube axis (circles give the equipotentials close to the Fermi energy).

FIG. 15. (Color online) Density of states of the (5,5) carbon nanotube for several magnetic flux values: $\phi/\phi_0=0$ (a), $\phi/\phi_0=0.1$ (b), $\phi/\phi_0=0.2$ (c), and $\phi/\phi_0=0.5$ (d). This is a metallic tube at zero magnetic flux but a gap opens up once a finite flux is applied and increases with the flux.

$$= \gamma_0 \exp[(2i\pi/\phi_0)\int_{\mathbf{r}_i}^{\mathbf{r}_j}\mathbf{A}(\mathbf{r})d\mathbf{r}]= \gamma_0 e^{-i\varphi_{ij}},$$ known as the Peierls substitution (Peierls, 1933).

2. Parallel field: The band-gap opening and orbital degeneracy splitting

In the axial case, however, the use of another basis set makes understanding of the Aharonov-Bohm effect straightforward. Indeed, if one considers the two-dimensional Cartesian coordinates $\tilde{\mathbf{r}}=(\tilde{x},\tilde{y})$ in the basis defined by the directions $(\mathbf{C}_h, \mathbf{T})$, then the vector potential is recast as $\mathbf{A}=(\phi/|\mathbf{C}_h|, 0)$ and the magnetic phase factor between two π orbitals located at $\tilde{\mathbf{r}}_i=(\tilde{x}_i, \tilde{y}_i)$ and $\tilde{\mathbf{r}}_j=(\tilde{x}_j, \tilde{y}_j)$ is simply written as $\varphi_i-\varphi_j=i\phi(\tilde{x}_i-\tilde{x}_j)/|\mathbf{C}_h|$. Accordingly, the periodic boundary conditions on the quantum phase will be modified as

$$\Psi_k(\mathbf{r} + |\mathbf{C}_h|) = e^{i\mathbf{k}\cdot\mathbf{C}_h}\exp\left((2\pi/\phi_0) \int_{\mathbf{r}}^{\mathbf{r}+C_h} \mathbf{A}(\mathbf{r}')d\mathbf{r}' \right)\Psi_k(\mathbf{r}),$$

and since the additional magnetic phase factor thus reduces to $2\pi\phi/\phi_0$, the change in the quantum momentum becomes

$$\kappa_\perp \rightarrow \kappa_\perp(\phi) = \frac{2\pi}{|\mathbf{C}_h|}\left(q \pm \frac{\alpha}{3} + \frac{\phi}{\phi_0} \right), \quad (25)$$

with $\alpha=0$ for metallic tubes, and $\alpha=\pm 1$ for semiconducting tubes. In Fig. 14 the effect of this change in momentum is illustrated in reciprocal space. From Eqs. (16) and (25), the field-dependent gap oscillation for an initially metallic tube is obtained,

$$\Delta E_B = E^+_{q=0}(k_\parallel, \phi/\phi_0) - E^-_{q=0}(k_\parallel, \phi/\phi_0) = 3\Delta E^1_g \phi/\phi_0,$$

if $\phi \leqslant \phi_0/2$, where $\Delta E^1_g=2\pi a_{cc}\gamma_0/\sqrt{3}|\mathbf{C}_h|$ denotes the gap at zero flux as given by Eq. (17). If $\phi_0/2 \leqslant \phi \leqslant \phi_0$, then $\Delta E_B=3\Delta E^1_g|1-\phi/\phi_0|$, so that the band gap exhibits an

oscillation between 0 and ΔE^1_g with a period ϕ_0 (Ajiki and Ando, 1993, 1994, 1996; Tian and Datta, 1994; Lin et al., 1995; Lu, 1995). For instance, $\Delta E_B \approx 75$ meV at 50 T for the (22,22) tube (diameter ≈ 3 nm), while $\Delta E_B \approx 40$ meV at 60 T for the (10,10) tube (diameter $=1.4$ nm). In addition, to obtain a field equivalent to $\phi=\phi_0$ in nanotubes with diameters of 1, 10, 20, and 40 nm, one typically needs magnetic fields of 5325, 53, 13, and 3 T, respectively.

In addition to such ϕ_0-periodic band-gap oscillations, the Aharonov-Bohm effect more generally affects the whole subband structure, as evidenced by Van Hove singularity splitting and shifts (Jiang et al., 2000; Roche et al., 2000; Shyu et al., 2003). These effects result from the influence of the magnetic field on the orbital degeneracy. Indeed, the initial symmetry of the carbon nanotubes implies that each available energy level is initially four-fold degenerate (including spin and orbital degeneracy). The orbital degeneracy is attributed to the symmetry between clockwise (+) and counterclockwise (−) electronic motions around the tube. In the presence of an external magnetic field, electrons in degenerate (+) and (−) eigenstates will acquire opposite orbital magnetic moments $\pm\mu_{\rm orb}$, which will thus produce an upshift of the energy of (+) and a downshift of the energy of (−), resulting in lifting the orbital degeneracy (or Van Hove singularity splitting).

This mechanism is illustrated in the DOS plots for the (5,5) and (10,10) tubes in Figs. 15 and 16, respectively, which are both metallic nanotubes at zero magnetic field (Roche et al., 2000). The calculations have been performed using a simple tight-binding model in the π-orbital approximation, while nearest-neighbor hopping integrals have been renormalized in the presence of a magnetic field using Eq. (24).
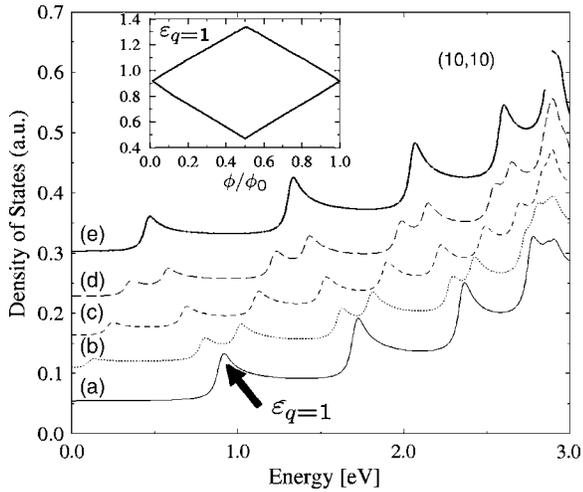
FIG. 16. Density of states of the (10,10) metallic tube as a function of energy for several magnetic flux values (see text). Curves have been vertically offset for clarity. Inset: Evolution of one VHS with magnetic flux. Adapted from Roche *et al.*, 2000.

As predicted theoretically, by applying a finite magnetic flux ϕ threading the tube, the band gap opens and increases linearly with ϕ, to reach a maximum value at half the quantum flux ($\phi_0/2$). Further, the band gap is linearly reduced until it finally closes back when the field reaches one quantum flux. The labels (a)–(e) in Fig. 16 are the DOSs for the (10,10) tube at $\phi/\phi_0=$(a) 0, (b) 0.125, (c) 0.25, (d) 0.375, and (e) 0.5. For $\phi/\phi_0=0.125$ [trace (b)], one notices that in the vicinity of the charge-neutrality point (i.e., $\varepsilon=0$), a new VHS appears, indicating the gap opening. In (c), (d), and (e), the gap is seen to increase, reaching its maximum value at $\phi/\phi_0=0.5$. The evolution of the VHS is then reversed and the gap closes again at $\phi/\phi_0=1$. For VHSs at higher energies (e.g., those located at $\varepsilon_{q=1}$), the oscillatory behavior is slightly more involved: at low fields a splitting is observed for each VHS, which is followed by crossing at higher flux, and finally all VHSs return to the original positions when $\phi/\phi_0=1$ (see the inset of Fig. 16).

In the case of armchair (n,n) metallic tubes, the magnitude of the field-dependent splitting of the qth VHS can be analytically ascertained:

$$\Delta E_B(\varepsilon_q,\phi/\phi_0)=2\gamma_0\left[\sin\frac{\pi}{q}\left(\cos\frac{\pi\phi}{q\phi_0}-1\right)\right.$$
$$\left.-\cos\frac{\pi}{q}\sin\frac{\pi\phi}{q\phi_0}\right]. \tag{26}$$

Semiconducting tubes [i.e., (n,m) tubes with $n-m=3l\pm1$ (l being an integer)] are affected in a similar way, but the gap expression is slightly different. One finds $\Delta E_B=\Delta E_g^1|1-3\phi/\phi_0|$ if $0\leq\phi\leq\phi_0/2$ and $\Delta E_B=\Delta E_g^1|2-3\phi/\phi_0|$ when $\phi_0/2\leq\phi\leq\phi_0$. Hence, the initial zero-field energy gap (ΔE_g^1) continuously decreases with increasing ϕ, to reach zero at $\phi=\phi_0/3$. The gap further opens as ϕ increases from $\phi_0/3$, reaching a local maxi-

mum ($\Delta E_g^1/2$) at $\phi=\phi_0/2$, before closing again at $\phi=2\phi_0/3$, and finally recovering its original value ΔE_g^1 at $\phi=\phi_0$. In Fig. 17, the DOS of a 3-nm-diameter semiconducting single-walled tube for various magnetic flux is illustrated. One notes that magnetic-field-induced lifting of the spin degeneracy brings some additional contribution to the total electron magnetic moment (Zeeman effect). This effect has been shown to yield an energy level displacement between spin up and spin down, linear with the magnetic flux, but inversely proportional to the squared radius of the tube (Jiang *et al.*, 2000).
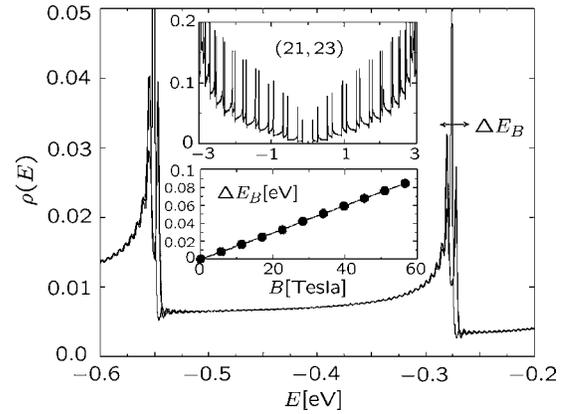
The Van Hove singularity splitting was recently observed by spectroscopic experiments (Zaric *et al.*, 2004). In addition, several experimental studies of electronic transport spectroscopy at low temperature in the Coulomb blockade regime (Kanda *et al.*, 2002; Coskun *et al.*, 2004; Jarillo-Herrero *et al.*, 2004; Minot *et al.*, 2004) or in the Fabry-Perot regime (Cao *et al.*, 2004; Jarillo-Herrero *et al.*, 2005) have also provided compelling evidences of the Aharonov-Bohm effect. The experimental estimation of the orbital magnetic moment was found to be of the order of $\simeq0.7$–1.5 meV/T (Minot *et al.*, 2004; Jarillo-Herrero *et al.*, 2005).

Magnetoresistance oscillations were also a subject of intense controversy in the early stage of carbon nanotube studies, since the origin and value of the Aharonov-Bohm oscillation period were apparently of different natures. Indeed, while some studies of large-diameter multiwall carbon nanotubes (Bachtold *et al.*, 1999) first revealed clear signatures of weak localization, with negative magnetoresistance and ($\phi_0/2$)-periodic Aharonov-Bohm oscillations driven by quantum interferences (Altshuler and Aronov, 1985), other reports assigned their magnetoresistance oscillations to field-modulated band structure effects, assuming a negligible contribution from interference effects (Fujiwara *et al.*, 1999; Lee *et al.*, 2000). The superimposed contributions to the Aharonov-Bohm oscillations from both band-structure and quantum interferences effects have been clearly disentangled recently (Stojetz *et al.*, 2005) and will be discussed in Sec. IV.D.1.

FIG. 17. Density of states of the (21,23) tube at zero and finite flux. Top inset: Expanded plot of the DOS. Bottom inset: Evolution of the VHS splitting Δ_B as a function of magnetic field.
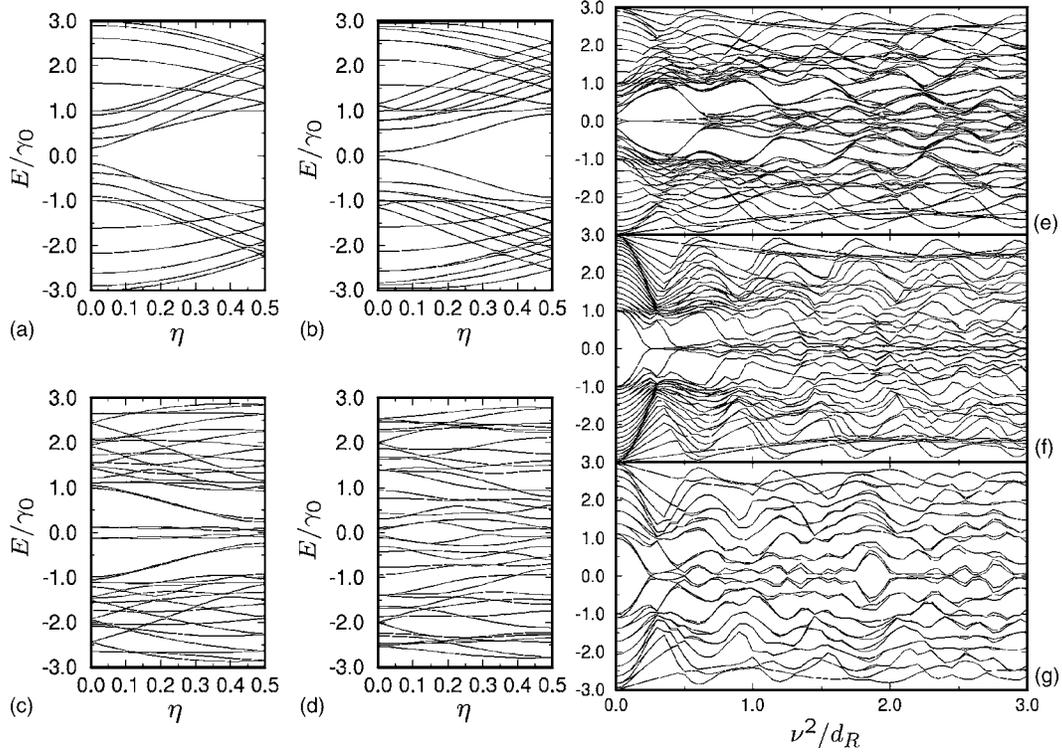
FIG. 18. Energy dispersion relation of a (10,0) tube as a function of the dimensionless wave vector $\eta = k_\parallel|\mathbf{T}|/2\pi$ for several values of the dimensionless inverse magnetic length ν. (a) $\nu = 0.0$, (b) 1.0, (c) 2.0, and (d) 3.0. (e), (f), (g) The energy at $k_\parallel = 0$ as a function of ν^2/N_R [N_R is the highest common divisor of $(2n+m,n+2m)$] for tubes (20,0), (20,20), and (9,9), respectively. Adapted from Saito, Dresselhaus, and Dresselhaus, 1994.

3. Perpendicular field: The onset of Landau levels

In the situation where the magnetic field is applied perpendicular to the tube axis, the modifications of the electronic spectrum are profoundly different. First the two-dimensional vector potential within the Landau gauge for the nanotube surface is now given by $\mathbf{A} = (0,(|\mathbf{C}_h|B/2\pi)\sin(2\pi\tilde{x}/|\mathbf{C}_h|))$, keeping $(\tilde{x},\tilde{y})$ as the coordinates along the circumferential and nanotube axis directions. For evident symmetry reasons, the net magnetic flux threading the tube is now zero. The phase factors can be computed using either this basis or the Cartesian basis defined earlier. The energy dispersion can then be evaluated as a function of magnetic field intensity (Ajiki and Ando, 1993, 1996; Saito *et al.*, 1994). In Fig. 18, the dispersion relation of the energy E/γ_0 is reported as a function of the dimensionless wave vector $k_\parallel|\mathbf{T}|/2\pi$ (Saito *et al.*, 1994), for several values of the dimensionless inverse magnetic length $\nu = |\mathbf{C}_h|/2\pi\ell_m$, where $\ell_m = \sqrt{\hbar/eB}$ is the magnetic length (first cyclotron orbit radius).

As seen in Fig. 18, as the intensity of the magnetic field is enhanced, the subband dispersion is reduced, with a particularly strong effect in the vicinity of the charge-neutrality point. This onset of a Landau-type subband can be further rationalized analytically. Indeed, by using the $\mathbf{k} \cdot \mathbf{p}$ method, an expression for the eigenstates under magnetic field close to the $\mathbf{K}$ points can be derived analytically for metallic tubes (see Sec. IV.C.1

for the zero-field case). The $\mathbf{k} \cdot \mathbf{p}$ equation at the charge-neutrality point ($\delta k = 0$) in the presence of a perpendicular magnetic field can be decoupled into two equations (Ando and Seri, 1997):

$$\left[-\frac{\partial}{\partial\tilde{x}} + \frac{|\mathbf{C}_h|}{2\pi\ell_m^2}\sin\left(\frac{2\pi\tilde{x}}{|\mathbf{C}_h|}\right) \right]\mathcal{F}_A^k(\tilde{x}) = 0, \tag{27}$$

$$\left[+\frac{\partial}{\partial\tilde{x}} + \frac{|\mathbf{C}_h|}{2\pi\ell_m^2}\sin\left(\frac{2\pi\tilde{x}}{|\mathbf{C}_h|}\right) \right]\mathcal{F}_B^k(\tilde{x}) = 0, \tag{28}$$

from which two independent solutions can be obtained:

$$\Psi_A(\tilde{x}) = \begin{pmatrix} 1 \\ 0 \end{pmatrix}\mathcal{F}_A(\tilde{x}), \quad \Psi_B(\tilde{x}) = \begin{pmatrix} 0 \\ 1 \end{pmatrix}\mathcal{F}_B(\tilde{x}),$$

$$\mathcal{F}_A(\tilde{x}) = \frac{1}{\sqrt{|\mathbf{C}_h|I_0(2\nu^2)}}\exp\left[-\nu^2\cos\left(\frac{2\pi x}{|\mathbf{C}_h|}\right) \right],$$

$$\mathcal{F}_B(\tilde{x}) = \frac{1}{\sqrt{|\mathbf{C}_h|I_0(2\nu^2)}}\exp\left[+\nu^2\cos\left(\frac{2\pi x}{|\mathbf{C}_h|}\right) \right],$$

where $I_0(2\nu^2)$ is a modified Bessel function of the first kind. Note that for sufficiently large magnetic field ($\nu \gg 1$) these wave functions become strongly localized in the circumference direction; that is, $\Psi_A(\tilde{x})$ is a wave function localized around $\tilde{x} = \pm|\mathbf{C}_h|/2$ at the bottom side of the cylinder, whereas $\Psi_B(\tilde{x})$ is localized around the
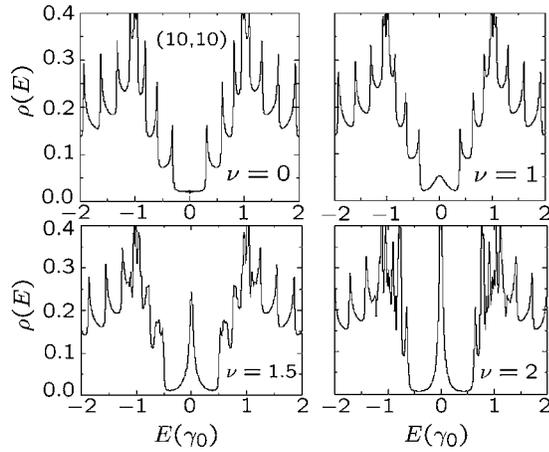
FIG. 19. Density of states of the (10,10) tube in a perpendicular magnetic field for several field strengths. The field strengths are expressed in terms of the dimensionless parameter $\nu = |\mathbf{C}_h|/2\pi\ell_m$, where $\ell_m = \sqrt{\hbar/eB}$ is the magnetic length.

top side $\tilde{x}=0$. As a result, the boundary condition on the wave function becomes irrelevant and the resulting band structures, starting from an initially metallic or semiconducting nanotube, become identical (Ajiki and Ando, 1993). For a small $\delta\mathbf{k}$ around the $\mathbf{K}$ points, the low-energy properties are described by an effective Hamiltonian, which can be determined by the two degenerate states Ψ_A and Ψ_B as

$$\mathcal{H}_{\text{eff}} = \begin{pmatrix} 0 & -i\gamma_0\delta k I_0^{-1}(2\nu^2) \\ +i\gamma_0\delta k I_0^{-1}(2\nu^2) & 0 \end{pmatrix}, \quad (29)$$

whose eigenvalues are $E_{q=0}^{\pm} = \pm\gamma_0|\delta\mathbf{k}|/I_0(2\nu^2)$, with a group velocity given by $v = \gamma_0/\hbar I_0(2\nu^2)$, while the density of states becomes $\rho(E_F) \sim I_0(2\nu^2)/\pi\gamma_0 \sim e^{\nu^2}/\sqrt{4\pi\nu^2}$ ($\nu \gg 1$) (Ando and Seri, 1997). The DOS at the charge-neutrality point thus diverges exponentially with increasing magnetic field. This is shown in Fig. 19 for the (10,10) tube for several magnetic field strengths.

Given the diameter-dependent scaling property of the band structure, the larger the tube diameter, the smaller the required value of the magnetic field to fully develop such a Landau subband at the charge-neutrality point. This effect has also been investigated analytically using a supersymmetry framework (Lee and Novikov, 2003). The appearance of the so-called Hofstadter butterfly was further explored numerically for large diameter nanotubes (Nemec and Cuniberti, 2006). As already seen in the field-dependent band structures (Fig. 18), the whole DOS also progressively degrades as the Landau subbands start to emerge within the whole spectrum, although strong mixing between high-energy subbands remains (Fig. 19).

As soon as $\nu = |\mathbf{C}_h|/2\pi\ell_m \geq 1$ is satisfied, the electronic spectrum becomes fully dominated by Landau levels. One finds that for tubes with diameters of 1, 10, 20, and 40 nm, the condition $\nu=1$ corresponds to magnetic field strengths of 2635, 26, 6.6, and 1.6 T, respectively.

In each case, $\ell_m \ll \ell_e$ (or $\omega_c\tau_e \gg 1$) has to be further satisfied for clear observation of Landau quantization, where ℓ_e is the mean free path, $\omega_c = eB/m$ is the cyclotron frequency, and τ_e is the scattering time (this condition is easily met at such high magnetic fields in carbon nanotubes since ℓ_e can be as long as 1 μm). Some signature of such Landau level formation was first reported by Kanda and co-workers (Kanda *et al.*, 2002).

F. Curvature effects: Beyond the zone-folding model

In the preceding sections, a model for the electronic properties of SWNTs was based on the confinement of electrons around the tube circumference, a confinement shown to induce selection on allowed $k_\perp$ Bloch vector components. As a matter of fact, since the states selected in the band-folding scheme were those of the planar graphene sheet, curvature effects are neglected. However, carbon nanotubes are not just stripes of graphene but small cylinders. Carbon atoms are placed on a cylindrical wall, a topology that induces several effects different from those of a planar graphene sheet: (a) the C-C bonds perpendicular and parallel to the axis are slightly different, so that the $\mathbf{a}_1$ and $\mathbf{a}_2$ basis vectors now have different lengths; (b) these bond length changes, and the formation of an angle for the two p_z orbitals located on bonds not strictly parallel to the axis, yield differences in the three hopping terms γ_0 between a carbon atom and its three neighbors; and (c) the planar symmetry is broken so that the π and σ states can mix and form hybrid orbitals that exhibit partial sp^2 and sp^3 character. Such curvature effect is not taken into account in the zone-folding model of graphene, where the π orbitals cannot mix with the σ states as they show different parity with respect to planar reflection. In the present section, the effect of finite curvature on the electronic properties of single-wall nanotubes will be investigated.

The effects labeled (a) and (b) modify the conditions that define the $\mathbf{k}$ point at which occupied and unoccupied bands do cross (a point we label k_F) and shift this Fermi vector k_F away from the Brillouin zone corners (K point) of the graphene sheet (Kane and Mele, 1997; Yang and Han, 2000). For armchair nanotubes, taking curvature into account shifts the Fermi wave vector along an allowed line of the graphene Brillouin zone. Consequently, for symmetry reasons, armchair tubes always preserve their metallic character with finite curvature. However, for metallic nonarmchair nanotubes, k_F moves away from the K point perpendicularly to the allowed $\mathbf{k}$ lines such that the allowed 1D subband (k,q) no longer passes through k_F, opening a very small band gap at E_F (see Fig. 20).

In summary, when accounting for curvature effects, the only zero-band-gap tubes are the (n,n) armchair nanotubes. The (n,m) tubes with $n-m=3l$, where l is a nonzero integer, are tiny-gap semiconductors. Armchair tubes are sometimes labeled type-I metallic tubes, while the others are of type-II. All other nanotubes are
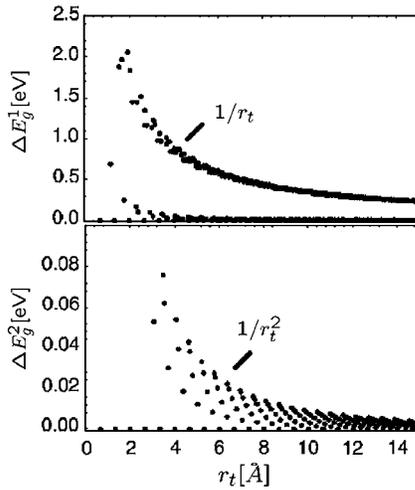
FIG. 20. Magnitude of primary (E_g^1) and secondary (E_g^2) gaps in carbon nanotubes with radii less than 15 Å. The primary gap (ΔE_g^1) scales as $1/R$ (top panel). The secondary gap (ΔE_g^2 or cuvature-induced gap) scales as $1/R^2$. The dots at $\Delta E_g^1 = \Delta E_g^2 = 0$ correspond to the armchair nanotubes which always preserve their metallic character. Adapted from Kane and Mele, 1997.

FIG. 21. *Ab initio* electronic band structure and density of states of a (6,0) carbon nanotube, illustrating the strong hybridization that occurs between π and σ states in a small-diameter tube. A new band σ^* appears and crosses the π states around the center of the Brillouin zone. The Fermi level is at zero energy. Adapted from Blase, Benedict, Shirley, and Louie, 1994.

intermediate-gap (a few tenths of an eV) semiconductors. For the tiny-gap semiconducting nanotubes, the so-called secondary gap (due to the curvature) depends on the diameter and the chiral angle, and scales as $1/d_t^2$ (Kane and Mele, 1997). For the quasimetallic zigzag nanotubes (chiral angle=0), this secondary gap is given by

$$\Delta E_g^2 = \frac{3\gamma_0 a_{cc}^2}{4 d_t^2} \qquad (30)$$

and is so small that, for most practical purposes, all $n-m=3l$ tubes can be considered as metallic at room temperature (see Fig. 20). Density-of-states measurements by scanning tunneling spectroscopy (Ouyang *et al.*, 2001b) confirm the expected $1/d_t^2$ dependence for three zigzag nanotubes and show that armchair nanotubes remain truly metallic. Consequently, the band-folding picture, based on the tight-binding approach (Hamada *et al.*, 1992; Mintmire *et al.*, 1992; Saito *et al.*, 1992), continues to be valid for large diameter tubes.

We now discuss point (c). For small tubes, the curvature is so strong that some rehybridization among the σ and π states appears. In such a case, the zone-folding picture may fail completely and *ab initio* calculations should be performed to predict the electronic properties of small diameter nanotubes. As an example, the *ab initio* band structure of the (6,0) tube is shown in Fig. 21. These first-principles pseudopotential local density functional (LDA) calculations (Blase, Benedict, Shirley, and Louie, 1994) indeed revealed that hybridization effects can occur in small radius nanotubes sufficiently strong to significantly alter their electronic structure. Strongly modified low-lying conduction band states are introduced into the band gap of insulating tubes because of

hybridization of the σ^* and π^* states. As a result, the energy gaps of some small radius tubes are decreased by more than 50%. In the specific case of the (6,0) tube, which is predicted to be a semimetal in the band-folding scheme, a singly degenerate hybrid σ^*-π^* state (see Fig. 21) is found to lie 0.83 eV (at Γ) below the doubly degenerate state that forms the top of the valence band in the zone-folding model. This band overlap makes the (6,0) tube a true metal within the LDA, with a density of states at the Fermi level equal to 0.07 state/eV atom. The σ^*-π^* hybridization can be clearly observed by drawing the charge density associated with the states around the Fermi level. Such states are no longer antisymmetric with respect to the tube wall, with a clear "charge spilling" out of the tube. For nanotubes with diameters greater than 1 nm, these rehybridization σ-π effects are unimportant. Further, as discussed above, symmetry considerations suggest that armchair tubes are less affected by such rehybridization.

Ultrasmall radius single-wall carbon nanotubes (diameter of about 4 Å) have been produced by confining their synthesis inside inert $AlPO_4$-5 zeolite channels (with inner diameter of about 7.3 Å) (Wang *et al.*, 2000). The diameter of these tubes gives them many unusual properties such as superconductivity (Tang *et al.*, 2001). Such a narrow distribution of diameters around 4 Å reduces the potential carbon nanotube candidates to three: the (3,3), (4,2), and (5,0). The properties of these ultrasmall tubes have already been extensively investigated by *ab initio* simulations (Dubay *et al.*, 2002; Liu and Chan, 2002; Machón *et al.*, 2002; Cabria *et al.*, 2003). In particular, it was shown that the (5,0) tube, expected to be semiconducting following the band-folding picture, is actually a metal with two bands (one doubly degenerate) crossing the Fermi level (yielding two different k_F).
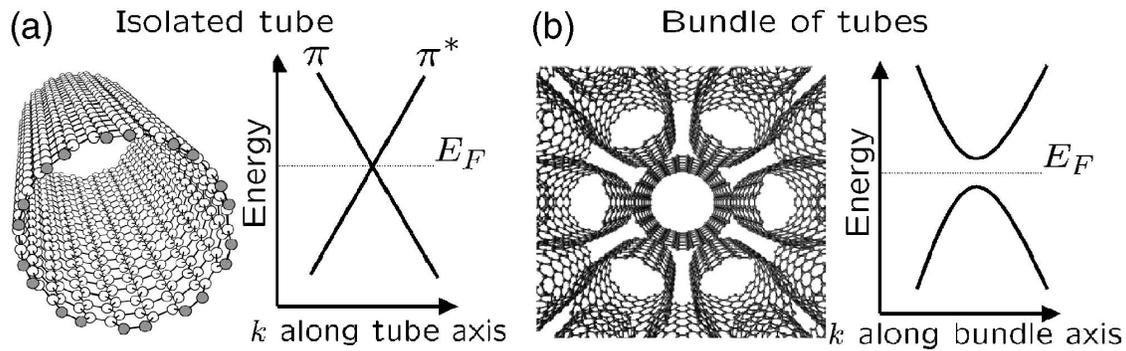
FIG. 22. Band crossing and band repulsion. (a) Schematic diagram of the crossing of the two linear bands for an isolated (n,n) carbon nanotube. One band has π-bonding character and the other has π-antibonding (π^*) character. E_F is the Fermi energy and k is the wave vector. (b) Repulsion of the bands due to breaking of mirror symmetry. Adapted from Delaney *et al.*, 1998.

This is a clear manifestation of curvature effects. We will come back to such small tubes when discussing the Peierls and superconducting instabilities in Sec. IV.F. The armchair (3,3) tube remains semimetallic, but with a π-π^* band crossing at E_F that is displaced off its ideal $2\Gamma X/3$ position, confirming as described above that armchair tubes are much less sensitive to curvature effects.

G. Nanotube bundle and multiwall system

From the previous section, we can deduce that only a special achiral subset of these carbon structures (armchair nanotubes) exhibits a true metallic behavior. Such metallic character can be explained by the high symmetry of these (n,n) tubes, namely, the n vertical planes and glide planes. Incorporating an armchair tube into a bundle, or inside another nanotube as in a multiwall system, could modify its intrinsic electronic properties as the symmetry is lowered.

Single-wall carbon nanotubes are grown by a laser-ablation, arc-discharge, or CVD method and always occur in bundles of 10–100 nanotubes. These bundles usually consist of nanotubes with different chirality and slightly different diameter. Even a "perfect" crystal made of identical tubes will alter the properties of the constituent CNTs through tube-tube interaction. Indeed, first-principles calculations reveal that broken symmetry of the (10,10) tube caused by interactions between tubes in a bundle induces a pseudogap of about 0.1 eV at the Fermi energy (Delaney *et al.*, 1998). This pseudogap strongly modifies many of the fundamental electronic properties of the armchair tubes, with a specific signature in the temperature dependence of the electrical conductivity and in the infrared absorption spectrum.

In the limit of an isolated (10,10) tube, the two bands crossing at E_F belong to different irreducible representations with respect to the tube symmetry planes, so that crossing is allowed. Upon breaking of this symmetry by tube-tube interaction in the hexagonal bundle symmetry, these bands can mix and start to repel at E_F (Fig. 22). The presence and magnitude (which depends inversely on the nanotube radius) of this pseudogap have been observed experimentally using low-temperature scan-

ning tunneling spectroscopy (Ouyang *et al.*, 2001b). In contrast, if (6,6) nanotubes are arranged in a hexagonal lattice which fully preserves the D_{6h} symmetry of the hexagonal packing, the band gap due to these intertube interactions is not observed (Charlier *et al.*, 1995). A small rotation of the (6,6) tubes in such an arrangement would break the D_{6h} symmetry of the (6,6) bundle and would open up this expected gap at the Fermi energy (Reich, Thomsen, and Ordejón, 2002).

Another possibility to tailor the electronic properties of nanotubes can be observed in the multilayering effect. In fact, the weak interaction between the concentric shells in a multiwall nanotube may have important effects on the electronic properties of the constituent isolated nanotubes (Lambin *et al.*, 1994; Kwon and Tománek, 1998). Interwall coupling, which, as just mentioned, opens a pseudogap in bundles of single-wall nanotubes (due to symmetry lowering), may periodically open and close four such pseudogaps near the Fermi energy in a metallic double-wall nanotube upon rotation of its inner shell with respect to the nanotube axis.

Figure 23 illustrates the intriguing interplay between geometry and electronic structure during the rotation of an inside (5,5) armchair nanotube in an outside (10,10) nanotube (both tubes sharing the same axis). The individual (5,5) and (10,10) tubes are both metallic and show the preferred graphitic interwall separation of 3.4 Å when nested. To determine the electronic properties of the double-wall nanotube, a tight-binding technique with parameters determined by *ab initio* calculations for simpler structures has been used (Lambin *et al.*, 1994; Kwon and Tománek, 1998). Due to the relatively high symmetry of the coaxial system, consisting of a D_{10h} (5,5) nanotube nested inside a D_{20h} (10,10) nanotube, the dependence of the intertube interaction on the tube orientation shows a periodicity of 18°. In the absence of the intertube interaction, the band structure of each tube is characterized by two crossing linear bands near E_F, one for left- and one for right-moving electrons. The band structure of a pair of decoupled (5,5) and (10,10) nanotubes, a mere superposition of the individual band structures, is shown in Fig. 23(a). Switching on the intertube interaction in the (5,5)@(10,10) double-wall tube re-
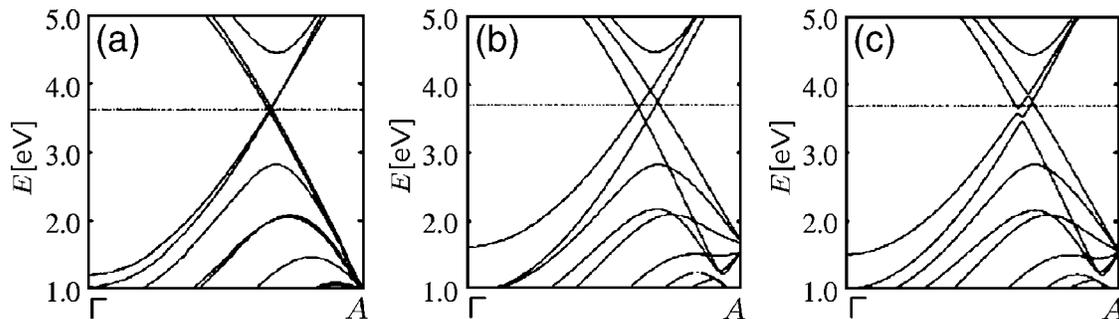
FIG. 23. Band structures of the same double-wall tube for different relative orientations. Near-degenerate bands with no gap characterize the (5,5)@(10,10) double-wall nanotube without intertube interaction (a). In the presence of intertube interaction, depending on the mutual tube orientation, the (5,5)@(10,10) system may show a zero gap (b) in the most symmetric (point group symmetry D_{10h}) or four pseudogaps (c) in a less symmetric and stable configuration (point group symmetry C_5). Adapted from Kwon and Tománek, 1998.

moves the near degeneracy of the bands near E_F as well [see Figs. 23(b) and 23(c)]. In the most stable orientation, the double-wall system is still characterized by the D_{10h} symmetry of the inner tube. The four bands cross, with a very small change in the slope [Fig. 23(b)]. While the same argument also applies to the least-stable configuration, a markedly different behavior is obtained at any other tube orientation that lowers the symmetry, giving rise to four band crossings [Fig. 23(c)]. This translates into four pseudogaps in the density of states near E_F.

At the Fermi level, the density of states of double-wall nanotubes is thus affected by the mutual orientation of the two constituent nanotubes, since the positions of the four pseudogaps depend significantly on it. The opening and closing of pseudogaps during the libration motion of the double-wall tube is a unique property that cannot be observed in single-wall nanotube ropes (Kwon and Tománek, 1998).

Finally, self-consistent charge-density and potential profiles for double-wall nanotubes, considering various chiralities, have been determined (Miyamoto et al., 2001) and demonstrate that the inner tube modifies the charge density associated with states near E_F, even outside the outer tube. A significant amount of charge, originating mainly from π electrons, is transferred into an interwall state, related to the interlayer state in graphite. In the limit of small tubes, the significant evolution of the CNT work function with respect to diameter shows as well that charge transfer may occur from one tube to another.

H. Structural defects in carbon nanotubes

In the previous sections, curvature effects and intertube and intershell interactions have been shown to significantly modify the electronic properties of carbon nanotubes from those obtained by a simple band folding of the graphene band structure. However, until now, each constituent nanotube was assumed to be perfect. In reality, the intrinsic honeycomb network of CNTs is probably not as perfect as usually assumed. Defects like pentagons, heptagons, vacancies, adatoms, or substitu-

tional impurities have been proposed theoretically and recently observed experimentally (Hashimoto et al., 2004; Fan et al., 2005). These defects are found to modify, at least locally, the electronic properties of the host nanotubes. Consequently, the introduction of defects in the carbon network is an interesting way to tailor its intrinsic properties, enabling new potential nanodevices and fostering innovative applications in nanoelectronics (Gómez-Navarro et al., 2005). The cases of chemical doping and functionalization will be explored in Sec. IV.C.4 where their effect on conductance will be analyzed.

1. Finite length and capping topologies

We have dealt so far with the properties of infinitely long nanotubes. In reality, nanotubes have a finite length (up to a few microns), a property which has two main consequences: (a) the confinement of the electronic states along the tube length; and (b) the disruption of the atomic network at the two ends, also labeled tips or apexes, with specific reconstructions and local electronic properties.

A conducting nanotube cut to a finite length should display standing waves characteristic of a one-dimensional particle-in-a-box model. Indeed, when electrons are confined in a box, quantum mechanics tells us that electrons can have only discrete values of kinetic energy. The energy spacing of the eigenvalues depends directly on the dimensions of the box: $\Delta E = h^2/2mL^2$, with L the length of the box. If this energy spacing is much higher than the thermal energy ($\Delta E \gg k_B T$), there are only completely occupied and completely empty levels and the system is an insulator. Further, the eigenstates are standing waves of the form $\sin(kz)$, with $k = 2\pi m/L$ and m an integer (the variable z is along the nanotube axis).

These standing waves have been studied theoretically by Rubio et al. (1999), and the highest occupied molecular orbital (HOMO), lowest unoccupied molecular orbital (LUMO), and "tip states" associated with a typical finite-length tube are illustrated in Fig. 24. Such stationary states have also been observed experimentally by
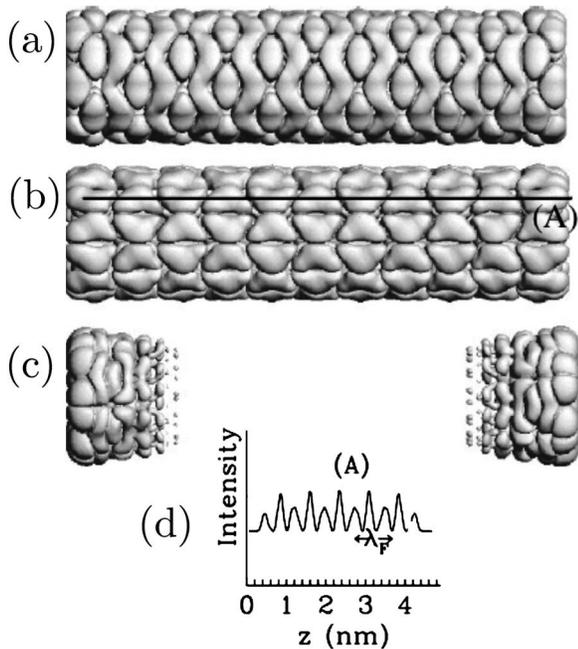
FIG. 24. *Ab initio* simulated STS images of the (a) HOMO, (b) LUMO, and (c) tip states of a 4.18-nm-long armchair tube. The solid line (A) in (b) corresponds to the line scan shown in (d) where the maxima of the electronic wave function are compared to the Fermi wavelength (λ_F). Adapted from Rubio *et al.*, 1999.

FIG. 25. (Color online) Densities of states along a (10,10) nanotube capped with half a C_{240} molecule. The horizontal bars indicate zero densities. The Fermi level is located at zero energy. The DOS curves are averaged over the atoms composing the sections labeled by $a-g$ on the right-hand side. Adapted from Charlier, 2002.

means of STS (Venema *et al.*, 1999; Lemay *et al.*, 2001) which essentially sees the square of the wave functions close to the Fermi level $[dI(V,x)/dV \sim |\Psi_F(x)|^2]$. The STS scans display several maxima repeated with a periodicity $\lambda_F \approx 0.74$ nm. Such an observation requires a higher energy resolution than the eigenstate separation (ΔE) and an electron coherence length larger than the tube length, which was satisfied for $L_{\text{tube}} \sim 30$ nm and $T=4$ K.

We now turn to the properties of tube tips or apexes. Due to the finite length, interesting structural features occur near the ends of all tubes. The closure of the graphene cylinder results from incorporation of topological defects, such as pentagons, which induce a disclination in the planar hexagonal carbon lattice. Such modifications of the structure modify, even though fairly locally, the tube electronic properties, while the tube body properties are essentially unchanged due to the large aspect ratio of most CNTs. Complex apex structures can arise, for instance, conical-shaped sharp tips, due to the way pentagons are distributed near the ends for full closure. Each topology leads to a specific local electronic structure (Tamura and Tsukada, 1995; Charlier and Rignanese, 2001).

These topological changes in the atomic structures near the end of closed carbon nanotubes are known to initiate sharp resonances in the DOS close to the Fermi energy region (Carroll *et al.*, 1997), affecting locally the electronic properties of the system, with, for example, expected consequences on field-emission energy-resolved spectra (see Sec. IV.G), or the chemical activity

of the apex, such as an enhanced sensitivity to oxidation (Ajayan *et al.*, 1993), a property used for selective tube opening at the apex. The energy positions of these resonant states with respect to the Fermi level depend sensitively on the relative positions of pentagons and their degree of confinement at the tube ends (De Vita *et al.*, 1999). The variations of the density of states along a (10, 10) nanotube capped by a hemispherical C_{240} tip apex, containing six pentagons in a fivefold-symmetric arrangement, are shown in Fig. 25 for illustration.

2. Connecting nanotubes

Since carbon nanotubes can be metallic or semiconducting, depending on their structure, they can be used to form metal-semiconductor, semiconductor-semiconductor, or metal-metal junctions. These junctions have an interesting potential for applications in logical devices. The key issue is to connect two semi-infinite nanotubes of different chirality but with equivalent diameters to allow for a smooth (energetically reasonable) tube-tube junction. It has been shown that the introduction of pentagon-heptagon pair defects into the hexagonal network of a single carbon nanotube can change the helicity of the carbon nanotube and fundamentally alter its electronic structure (Dunlap, 1994; Lambin *et al.*, 1995; Charlier *et al.*, 1996; Chico, Crespsi, Benedict, Louie, and Cohen, 1996; Saito *et al.*, 1996). Both the existence of such local atomic rearrangements and the measurement of their respective electronic and transport properties have been resolved experimentally (Yao *et al.*, 1999; Ouyang *et al.*, 2001a).

Such defects must induce zero net curvature to prevent the tube from flaring or closing. The smallest topological defect with minimal local curvature (hence mini-

FIG. 27. Carbon-based ideal junctions, exhibiting, respectively, (a) X, (b) T, and (c) Y geometries, respectively. Adapted from Terrones *et al.*, 2002.

mission electron microscope can indeed be used to locally irradiate carbon-based nanostructures. Covalently connected crossed single-wall carbon nanotubes have been created using electron beam welding at elevated temperatures (Terrones, Terrones, Banhart, Charlier, and Ajayan, 2000; Terrones *et al.*, 2002). These molecular junctions of various geometries (X, Y, and T) are found to be stable after the irradiation process. Figure 27(a) depicts an ideal X-shaped nanotube connection, where a (5,5) armchair nanotube intersects a (11,0) zigzag tube. In order to generate a smooth topological welding at the junctions, six heptagons are introduced at each crossing point to create the needed negative curvature. The electronic properties of such junctions, with the signature of the heptagonal rings, are characterized by an enhancement of the DOS close to E_F, an effect similar to that described in the case of pentagons at the tube apex (Charlier, 2002).

Electronic transport measurements on multiwall Y-shaped junctions showed that these carbon nanostructures behave as intrinsic nonlinear devices, displaying strong rectifying behavior at room temperature (Papadopoulos *et al.*, 2000). However, theoretical calculations have shown that the rectifying behavior of Y-shaped junctions is not an intrinsic property of the branching, but is solely due to the properties of the interfaces between the nanotube branches and metallic leads (Meunier *et al.*, 2002). Much more research is needed to pave the way toward the controlled fabrication of nanotube-based molecular junctions and network architectures exhibiting interesting electronic behavior.

3. Vacancies, adatoms, Stone-Wales, etc.

As in many other materials, the existence of defects in nanotubes affects the material properties. These defects can occur in various forms, among which are atomic vacancies (El-Barbary *et al.*, 2003). A vacancy is simply the absence of a carbon atom in the hexagonal network. However, as illustrated in Fig. 28(a), an atomic reconstruction of the vacancy (C_s) is found to be more stable energetically as compared to the unreconstructed vacancy (D_{3h}) in the graphene sheet. Removing the remaining two-coordinated C atom [see Fig. 28(a)] leads to a "divacancy," which is composed of two pentagons separated by an octagon (Gómez-Navarro *et al.*, 2005).

FIG. 26. (Color online) Nanotube-based junctions. (a) Atomic structure of a (8,0)/(7,1) intramolecular carbon nanotube junction. The large balls denote atoms forming the heptagon-pentagon pair. (b) The electron densities of states related to the two perfect (8,0) and (7,1) nanotubes are illustrated with thick and thin lines, respectively. Adapted from Charlier, 2002.

mizing the energy cost) and zero net curvature is a pentagon-heptagon pair. When the pentagon is attached to the heptagon, as in the aniline structure, it only creates topological changes (but no net disclination) which can be treated as a single local defect. Such a pair will create only a small local deformation and may also generate a small change in the helicity, depending on its orientation in the hexagonal network.

Figure 26 depicts the connection, using a single 5-7 pair, between two nanotubes exhibiting different electronic properties. The (8,0) nanotube has a 1.2-eV gap in the tight-binding approximation, and the (7,1) tube is a semimetal (although a small curvature-induced gap is present close to the Fermi energy). Such a system represents thus a semiconductor/metal Schottky junction which could be used, together with similar junctions, as building blocks in nanoscale electronic devices, provided that their growth is controlled. These carbon-carbon junctions have been generalized to the case of C/BN heterojunctions (Blase *et al.*, 1997), with BN (boron-nitride) tubes displaying a large band gap (see Sec. III.I). Such junctions could result from the segregation of carbon atoms in composite boron-carbon-nitrogen tubes, a segregation which is energetically favorable and has been observed experimentally (Suenaga *et al.*, 1997).

While the spontaneous formation during growth of 5-7 pairs conveying the synthesis of tube-tube junctions seems difficult to engineer, another approach has been developed to connect nanotubes. The beam of a trans-

FIG. 28. Defects in the hexagonal network. (a) Graphene portion containing a vacancy. The carbon network exhibits some reconstruction. (b) Graphene portion displaying a Stone-Wales defect (two adjacent heptagons surrounded by two pentagons). Adapted from Ewels *et al.*, 2002.

FIG. 29. Nonchiral Haeckelite nanotubes of similar diameter (1.4 nm). (a) Nanotube segment containing only heptagons and pentagons paired symmetrically. (b) Nanotube segment exhibiting repetitive units of three agglomerated heptagons, surrounded by alternating pentagons and hexagons. (c) Nanotube segment containing pentalene and heptalene units bound together and surrounded by six-membered rings. Adapted from Terrones, Terrones, Hernandez, Grobert, Charlier, and Ajeyan, 2000.

Electron irradiation induces structural transformations in carbon nanotubes, mainly vacancies and interstitials, created by the impact of high-energy electrons, followed by saturation of highly reactive dangling bonds at undercoordinated carbon atoms (Banhart, 1999). Defects have been intensively studied in irradiated graphite (Telling *et al.*, 2003), and the carbon vacancy-adatom pair is certainly one of the most common (Ewels *et al.*, 2002). In addition, it is suggested that both the adatom and the single monatomic vacancy induce magnetic properties in these carbon nanostructures (Lehtinen *et al.*, 2003).

Another well-known form of defect that occurs in carbon nanotubes is the Stone-Wales reconstruction [Fig. 28(b)], which creates two pentagon-heptagon pairs by the 90° rotation of any C-C bond in the hexagonal network (Stone and Wales, 1986). Such a topological defect can be induced by strain and determines the plastic response and mechanical resistance to tension applied to the nanotube (Orlikowski *et al.*, 2000; Jensen *et al.*, 2002).

Most of the outstanding properties of carbon nanotubes rely on them being almost atomically perfect, but the amount of imperfections and the effect that they have on the tube properties have been poorly understood to date. Defects are known to modify the elastic, mechanical, and electrical response of carbon nanotubes. Such defects are present in as-grown tubes, but controlling their density externally (i.e., using ion irradiation) may open a path toward the tuning of the electronic characteristics of the nanotube (Gómez-Navarro *et al.*, 2005).

Following the previous idea of introducing five- and seven-membered rings into hexagonal networks, a novel class of perfect crystals, consisting of layered sp^2-like carbon sheets containing periodic arrangements of pentagons, heptagons, and hexagons, has been proposed (Terrones, Terrones, Hernandez, Grobert, Charlier, and Ajayan, 2000). These sheets are rolled up so as to generate single-wall nanotubes (Fig. 29), which resemble locally the radiolaria drawings of Haeckel (1998).

Calculations indicate that these Haeckelite structures are more stable than C_{60} and have energies of the order of 0.3–0.4 eV/atom with respect to graphene. These ide-

ally defective tubes exhibit intriguing electronic properties: density-of-states calculations of Haeckelite tubes revealed an intrinsic metallic behavior, independent of orientation, tube diameter, and chirality. Further, a rather large DOS at the Fermi level is noticed for the family of tubes depicted in Fig. 29(b). Such properties are clearly related to our discussion of the 5-7 defects and extend an early prediction on the evolution of electronic properties with increasing defect concentration (Crespi *et al.*, 1997). The predicted *ab initio* infrared and Raman frequencies (Rocquefelte *et al.*, 2004) allow one to distinguish these structures unambiguously and may help in identifying them in future syntheses.

I. Optical properties and excitonic effects

We conclude this section on the electronic properties of nanotubes by exploring their optical response. As optical absorption spectra are conventionally interpreted in terms of transitions between the valence and conduction bands, discussing the interaction with photons just after discussing the electronic band structure looks like a good idea. However, the importance of many-body effects (electron-hole interactions or excitons) significantly complicates this interpretation.

The optical properties of nanotubes are of major importance not only for potential applications of CNTs in optoelectronic devices (Misewich *et al.*, 2003), but also as a powerful tool to relate the observed absorption or photoluminescence (PL) spectra to the (n, m) indices of the tubes, complementing other techniques such as Raman, diffraction, or STM studies. Experimentally, an important step forward was taken with the observation of a rather bright and structured PL spectra in the infrared, associated with CNTs isolated in cylindrical micelles (Bachilo *et al.*, 2002; O'Connell *et al.*, 2002). The aggregation of tubes in bundles is indeed expected to strongly
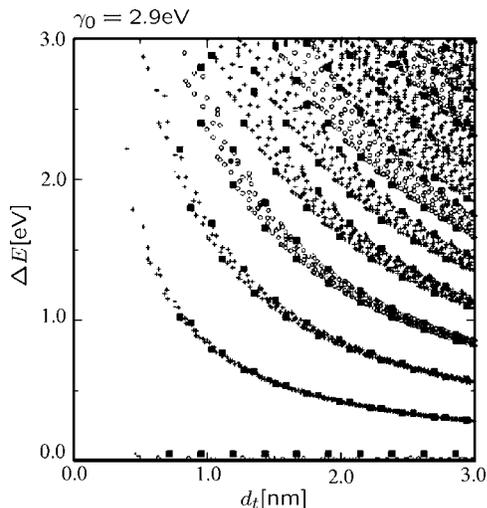
FIG. 30. Energy separation $E_{ii}(d)$ for all (n,m) values as a function of CNT diameter d_t, with $0.7 \leqslant d_t \leqslant 3.0$ nm. Crosses and open circles denote the peaks of semiconducting and metallic tubes, respectively. Solid squares denote $E_{ii}(d)$ values for zigzag tubes. Adapted from Saito, Dresselhaus, and Dresselhaus, 2000.

quench and broaden the luminescence of carbon tubes through transfer of hot electrons to metallic tubes where they can recombine nonradiatively. This subject of the optical properties of SWNTs is rapidly growing, and the following topics should be considered as a brief introduction to the field.

The first analysis of the optical data relied on the assumption that the absorption peaks can be mapped onto the energy differences between Van Hove singularities in the valence and conduction bands. In the case of nanotubes, the accumulation of states at VHS suggests that the optical spectrum will be dominated by transitions between these spikes in the density of states. Further, as the absorption is strongly quenched by the depolarizing fields for light polarized in transverse directions (Benedict, Louie, and Cohen, 1995; Marinopoulos *et al.*, 2003), the selection rules associated with light polarized parallel to the tube ($\Delta q = 0$, q the azimuthal quantum number) will even specify that the strongest optical transitions will take place between subbands with the same angular momentum, yielding the so-called E_{ii} excitation energies. We recall that in the orthogonal (π-π^*) model, each q index yields two symmetric bands, one occupied and one unoccupied, and transitions between these two subbands are therefore allowed.

This analysis led to the useful Kataura's plot (Kataura *et al.*, 1999; Saito, Dresselhaus, and Dresselhaus, 2000; Popov and Henrard, 2004) which gathers on the same graph the $E_{ii}(d_t)$ transition energies as a function of diameter d_t. The interest of such a representation (see Fig. 30) stems from an early remark by White and Mintmire (1998) that the E_{ii} transitions should depend only on the nanotube diameter, and not its chirality, leading to well-defined and -separated $E_{ii}(d_t)$ lines (see Sec. III.D

above). The same arguments were developed for the primary band gaps in semiconducting tubes. In particular, it was suggested that the diameter of CNTs could be straightforwardly inferred from the optical absorption peaks or the resonance energies in Raman spectra, complementing data obtained from the evolution with diameter of the RBM frequency. This diameter-only dependence of E_{ii} transitions works remarkably well at low excitation energies, but strong deviations can be seen on the plot of Kataura *et al.* by a marked broadening of the high-energy E_{ii} lines. This broadening was shown to originate in deviations from the linear dispersion of the energy bands away from the Fermi level, an effect designated as "trigonal warping" (Saito, Dresselhaus, and Dresselhaus, 2000).

However, accurate absorption studies on well-calibrated (n,m) nanotubes showed evidence for some deviations from the analysis of Kataura *et al.* since peaks in the absorption spectra and E_{ii} transition energies in between Van Hove singularities showed systematic deviations (Bachilo *et al.*, 2002; O'Connell *et al.*, 2002; Wang and Griffoni, 2005). In particular, the ratio E_{22}/E_{11}, predicted to be equal to 2 in the approximation where bands are linear close to E_F (Mintmire and White, 1998), was found to be significantly smaller (Bachilo *et al.*, 2002), even in the limit of large tubes where the approximation is supposed to work best. While trigonal warping effects can easily account for deviations from 2 of the E_{22}/E_{11} ratio in small SWNTs, it was a puzzling result in the limit of large tubes. This is the so-called ratio problem in SWNTs (Kane and Mele, 2003). Further, Bachilo *et al.* (2002) reported the decrease of the PL intensity for SWNTs with small chiral angles (zigzag tubes), an effect that is difficult to understand within the independent-electron model.

These deviations triggered several theoretical studies to explore excitonic effects in the CNT optical spectra. Excitonic effects in purely 1D systems have been shown to exhibit very specific features, such as a divergency of the binding energy of the electron-hole pairs (Loudon, 1959) in a simple 1D generalization of the Mott-Wannier model (Elliott, 1957), or the quenching of the so-called Sommerfeld factors (Ogawa and Takagahara, 1991a, 1991b) which compensates for the Van Hove singularity at the E_{11} edge. It is not clear, however, that such effects, valid for strictly 1D objects, should be easily observed in carbon nanotubes.

Following early predictions based on semiempirical approaches (Ando, 1997; Kane and Mele, 2003; Perebeinos *et al.*, 2004), accurate *ab initio* calculations showed that bound excitons with binding energies of up to an eV could be found in semiconducting tubes (Chang *et al.*, 2004; Spataru *et al.*, 2004). This is shown in Fig. 31 in the case of the (8,0) carbon nanotube. Such calculations were based on the resolution of the so-called Bethe-Salpeter equations which can be written as follows:
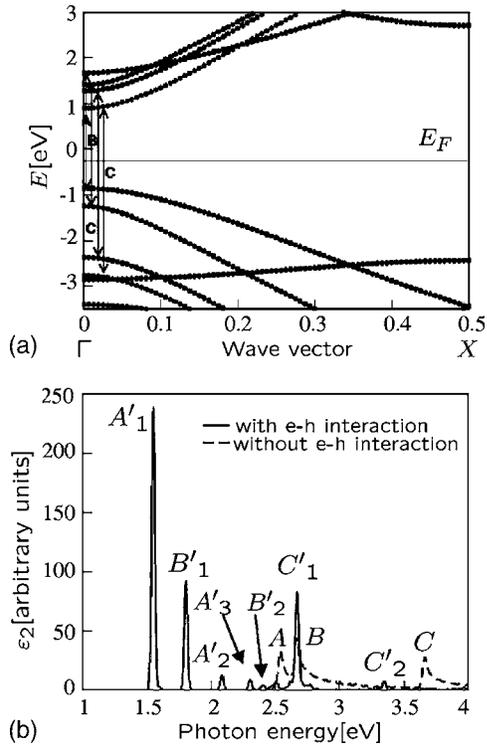
FIG. 31. Excitons in nanotubes. (a) Quasiparticle band struc-
ture and (b) optical absorption spectra (with and without
electron-hole interaction) for a semiconducting (8,0) carbon
nanotube. Adapted from Spataru *et al.*, 2004.

$$(E_{c\mathbf{k}} - E_{v\mathbf{k}})A^S_{vc\mathbf{k}} + \sum_{v'c'\mathbf{k}'} \langle vc\mathbf{k}|K^{eh}|v'c'\mathbf{k}'\rangle A^S_{vc\mathbf{k}} = \Omega^S A^S_{vc\mathbf{k}},$$

(31)

where $A^S_{vc\mathbf{k}}$ is the exciton amplitude, K^{eh} is the electron-
hole kernel, and $|vc\mathbf{k}\rangle$ is the electron-hole two-body
wave functions in the absence of interactions (taken as a
basis to expand the interacting electron-hole eigen-
states). The first term on the left-hand side of Eq. (31)
corresponds to the quasiparticle spectrum in the absence
of electron-hole interactions (yielding the E_{ii} energies).
The second term accounts for the electron-hole interac-
tions. The kernel K^{eh} includes two contributions:
screened Coulomb interaction and an exchange term.
This latter stabilizes triplet states, yielding potentially
low-lying dark excitons with vanishingly small dipole
matrix elements with the ground state which is a singlet.
This is a crucial issue since the existence of low-lying
dark excitons dramatically reduces the PL efficiency of
isolated tubes. The application of a magnetic field, by
mixing singlet and triplet states, allows us to bypass this
problem, even though very large fields are needed (Zaric
et al., 2005). Clearly, as the electron-hole interactions are
screened, excitonic effects will be predominant when-
ever screening is weak, namely, in semiconducting tubes.
Further, the binding energy is expected to be large in
small tubes where holes and electrons are spatially con-
fined.

These theoretical evaluations of the exciton binding
energies were confirmed by experimental measurements
yielding values of 0.3–0.4 eV for nanotubes with diam-
eters in the 0.7–0.9-nm range (Maultzsch *et al.*, 2005;
Wang *et al.*, 2005a). Concerning the helicity-related PL
intensity, it was suggested by Reich *et al.* (2005) that
exciton-exciton resonance effects, strongly depending on
the E_{22}/E_{11} ratio, and thus on chirality through trigonal
warping, might explain the experimental observations.
On more general grounds, the PL efficiency of nano-
tubes is found to be rather small. This suggests the exis-
tence of rather long radiative lifetimes, allowing for non-
radiative processes and/or the existence of low-lying
optically inactive (dark) excitons. Radiative lifetimes in
SWNTs are under intensive theoretical and experimen-
tal investigation and results are still very scattered
(Hagen *et al.*, 2004, 2005; Wang *et al.*, 2004; Spataru *et al.*,
2005). Other topics, such as electroluminescence, based
on the recombination of electrons and holes injected at
the two different electrodes of an ambipolar transistor
(Misewich *et al.*, 2003) or generated by impact excitation
(Chen, Perebeinos, Freitag, Tsang, Fu, Lin, and Avouris,
2005; Marty *et al.*, 2006), or photoconductivity, where, on
the contrary, the optically excited electron-hole pairs are
separated by an applied bias, are also under investiga-
tion, and theoretical results are still very scarce (Perebei-
nos and Avouris, 2006).

We conclude this section on the optical properties of
nanotubes by making a small incursion into the physics
of "composite" BCN tubes. Boron nitride nanotubes
(Blase, Rubio, Cohen, and Louie, 1994; Rubio *et al.*,
1994) are wide-gap insulators and strong excitonic ef-
fects have been shown theoretically (Arnaud *et al.*, 2006;
Park *et al.*, 2006; Wirtz *et al.*, 2006) to explain the experi-
mentally available optical results (Watanabe *et al.*, 2004;
Arenal *et al.*, 2005; Lauret *et al.*, 2005). The prospect of
obtaining lasing materials in the uv range (215 nm, Wa-
tanabe *et al.*, 2004) is strong motivation for pursuing the
study of *h*-BN systems. Finally, intermediate between
metallic or small-gap CNTs and insulating BN tubes,
composite $B_xC_yN_z$ systems have been synthesized and
PL in the visible range has been demonstrated for sys-
tems with a BC_2N stoichiometry (Watanabe *et al.*, 1996;
Chen *et al.*, 1999; Bai *et al.*, 2000). It has been shown on
the basis of *ab inito* calculations that the band gap of
such systems could vary in the visible range depending
on the size of segregated pure carbon or BN sections, a
segregation phenomenon which stabilizes the structure
(Blase *et al.*, 1997, 1999; Mazzoni *et al.*, 2006). Such sys-
tems, even though opening the way for the design of
tube-based optoelectronic devices, remain much less
studied than CNTs.

IV. TRANSPORT PROPERTIES OF CARBON NANOTUBES

A. Preliminary remarks

Coherent quantum transport in mesoscopic and low-
dimensional systems can be rigorously investigated with
either the Kubo-Greenwood (Kubo, 1966) or the

Landauer-Büttiker formalisms (Büttiker *et al.*, 1985). The first approach, which derives from the fluctuation-dissipation theorem, allows one to evaluate the intrinsic conduction regimes within the linear response and gives direct access to the fundamental transport length scales, such as the elastic mean free path (ℓ_e) and localization length (ξ). While ℓ_e results from elastic backscattering driven by static perturbations (defects, impurities) of an otherwise clean crystalline structure, ξ denotes the scale beyond which quantum conductance decays exponentially with the system length (L), owing to the accumulation of quantum interference effects that progressively drive the electronic system from weak to strong localization. The coherence length L_ϕ gives the scale beyond which localization effects are fully suppressed owing to decoherence mechanisms, such as electron-phonon (e-ph) or electron-electron (e-e) couplings, treated as perturbations on the otherwise noninteracting electronic gas (weak-localization regime). When ℓ_e becomes longer than the length of the nanotube between voltage probes, the carriers propagate ballistically and contact effects prevail. In such a situation, the Landauer-Büttiker formalism becomes more appropriate, since it rigorously treats transmission properties for open systems and arbitrary interface geometries. In addition, its formal extensions [nonequilibrium Green's functions (NEGFs) and the Keldysh formalism] further enable one to investigate quantum transport in situations far from equilibrium, of relevance for high-bias regimes or situations with a dominating contribution of Coulomb interactions (Datta, 1995).

Interestingly, to investigate coherent quantum transport in a nanotube of length L with reflectionless contacts to external reservoirs, the two transport formalisms are formally fully equivalent (Szafer and Stone, 1988). Within the linear response theory, the Kubo conductance can be numerically computed as $G(E,L) = (2e^2/L)\lim_{t\to\infty}\mathrm{Tr}\{\delta(E-\hat{H})\hat{D}(E,t)\}$, where $\delta(E-\hat{H})$ is the spectral measure operator, the trace of which gives the total density of states, whereas $\hat{D}(t) = [\hat{X}(t) - \hat{X}(0)]^2/t$ is the diffusivity operator, defining $\hat{X}(t)$ as the position operator in the Heisenberg representation and L as the relevant length scale associated with the normalization factor (Roche and Mayou, 1997; Roche, 1999). In the presence of static disorder, the diffusivity for a given wave packet will reach a saturation regime whose value will be related to the elastic mean free path $\ell_e(E)$ through $D(E) \sim v(E)\ell_e(E)$, with $v(E)$ the velocity of wave packets with energy E. The wave-packet quantum dynamics is numerically explored by solving the time-dependent Schrödinger equation. Such an approach, implemented using order-N computational techniques, has been successfully compared to analytical results derived from Fermi's golden rule (FGR) for uniform disorder (White and Todorov, 1998; Roche *et al.*, 2000). Figure 32 (top) shows the various conduction regimes (ballistic, diffusive, and localized) for wave packets propagating in CNTs with on-site random fluc-
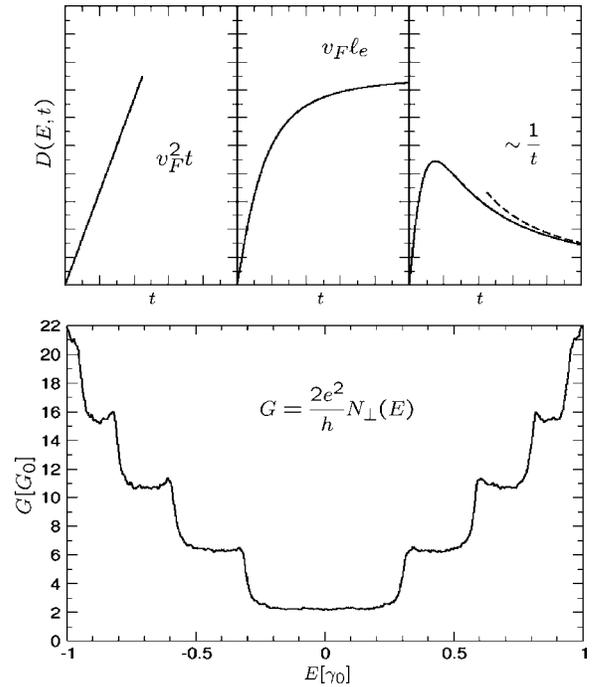
FIG. 32. Conduction regime in nanotubes. Top: Diffusion coefficient for three typical conduction regimes in (10,10) metallic nanotubes. From left to right: ballistic, diffusive, and localized regimes are seen at a long time scale. Bottom: Kubo conductance for the ballistic case.

tuations (Anderson-type elastic disorder). In Fig. 32 (bottom), the quantum conductance obtained with the Kubo formula for a clean infinite metallic armchair nanotube is shown to be quantized, retrieving the Landauer-Büttiker formulation in terms of conducting channels.

On the other hand, the Landauer-Büttiker conductance is evaluated from the transmission coefficient

$$T(E) = \mathrm{tr}\{\hat{\Gamma}_L(E)\hat{G}_{\mathrm{tube}}^{(+)}(E)\hat{\Gamma}_R(E)\hat{G}_{\mathrm{tube}}^{(-)}(E)\}, \qquad (32)$$

given as a function of the retarded Green's function $\hat{G}_{\mathrm{tube}}^{(+)}(E) = \{E\hat{I} - \hat{H}_{\mathrm{tube}} - \hat{\Sigma}_L(E) - \hat{\Sigma}_R(E)\}^{-1}$ where $\hat{\Sigma}_R$ ($\hat{\Sigma}_L$) is the self-energy accounting for the coupling with the right (left) electrode and $\hat{\Gamma}_L = i(\hat{\Sigma}_L) - \hat{\Sigma}_L^{(+)}$ (Datta, 1995). These quantities are generally computed through some order-N decimation technique (López-Sancho *et al.*, 1984). The Landauer-Büttiker formula can be implemented with different effective models, such as a tight-binding Hamiltonian or a Hamiltonian derived from first principles.

In the following, the main transport characteristics of metallic carbon nanotubes in ballistic or weakly disordered regimes will be first addressed. Transport length scales will be discussed, as well as conduction regimes such as weak and strong localization. Further, the effects of e-ph and e-e interactions will be scrutinized in regard to their fundamental contribution either to decoherence and inelastic scattering or to the temperature dependence of the conductance. The possibility of a strong departure from Fermi-liquid behavior will also be dis-
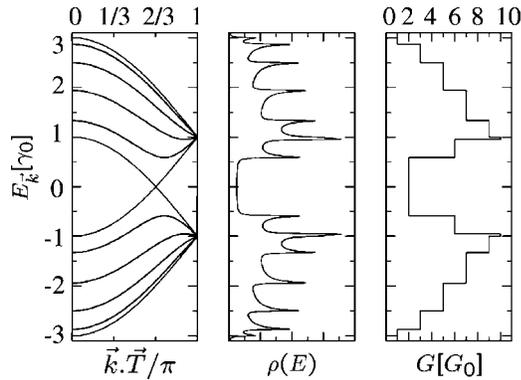
FIG. 33. Band structure (left), density of states (middle), and conductance (right) for the (5,5) armchair nanotube.

cussed through a presentation of the Luttinger-liquid model, mainly derived for armchair nanotubes, the predictions of which have received experimental supporting evidence.

B. The clean limit

1. Ballistic motion and conductance quantization

For a carbon nanotube of length L between metallic contact reservoirs, the transport regime is ballistic if the measured conductance is L independent and only given by the energy-dependent number of available quantum channels $N_\perp(E)$ times the conductance quantum $G_0 = 2e^2/h$, that is, $G(E) = 2e^2/h \times N_\perp(E)$, including spin degeneracy. This occurs only in the case of perfect (reflection less) or ohmic contacts between the CNT and the metallic voltage probes. In this regime, the expected energy-dependent conductance spectrum is easily deduced, from band structure calculations, by counting the number of channels at a given energy. For instance, metallic armchair nanotubes present two quantum channels at the Fermi energy $E_F = 0$, or charge-neutrality point, resulting in $G(E_F) = 2G_0$. At higher energies, the conductance increases as more channels become available to conduction. For illustration, the electronic bands and conductance of the (5,5) metallic tube are displayed in Fig. 33 within the symmetric π-π^* model.

These values are, however, the uppermost theoretical limits that could be experimentally measured. In practical situations, lower values are found since reflectionless transmission at the interface between the voltage probes and nanotubes is fundamentally limited by interface symmetry mismatch, inducing Bragg-type backscattering. Additionally, topological and chemical disorder, as well as intershell coupling, introduce intrinsic backscattering along the tube, which also reduces the transmission capability. To account for both effects, one generally introduces $T_n(E) \leq 1$, the transmission amplitude for a given channel, at energy E, so that $G(E) = G_0 \Sigma_{n=1, N_\perp} T_n(E)$ (Datta, 1995).
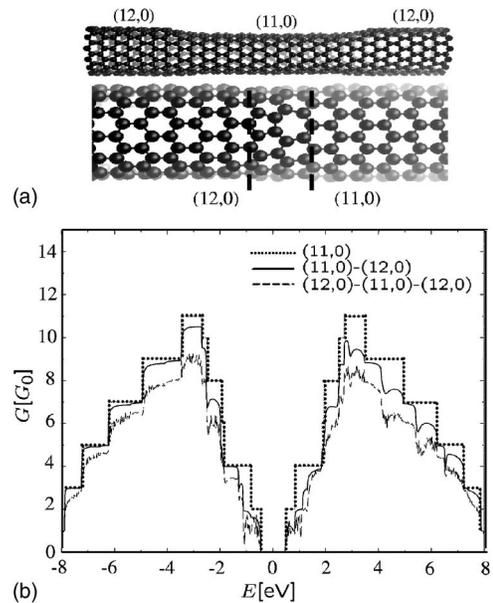
FIG. 34. Quantum conductance in nanotube-based junctions. (a) Top: Illustration of a nanotube-based metal-(12,0)/semiconductor-(11,0)/metal-(12,0) heterojunction. Bottom: Close-up of the interface region with pentagon-heptagon pair defect at the origin of chirality changes. (b) Corresponding conductance spectra for the single nanotube (11,0) showing the exact number of conduction channels (dotted line), together with the conductance of the double junctions (11,0)-(12,0) (bold line) and (12,0)-(11,0)-(12,0) (bold dashed line).

2. Transport properties of CNT-based junctions and contact resistance

Beyond the fundamental interest in understanding the transport properties of 1D systems, the integration of CNTs in electronic devices such as field-effect transistors (CNFETs) (Martel *et al.*, 1998; Tans *et al.*, 1998) raises the question of the contact resistance, that is, the ability for electrons to jump from a metallic electrode, used as the source or drain, onto the nanotube. In particular, in contrast to the predictions of quantized conductance obtained for clean infinite systems, for a given nanotube/electrode contact geometry, a lowering of the transmission across the interface will be systematically obtained.

As first analyzed by Chico and co-workers (Chico, Benedict, Louie, and Cohen, 1996), even for the most favorable case, i.e., for an intramolecular nanotube-based heterojunction, the symmetry mismatch between incoming and outgoing electronic states yields a transmission probability lower than 1. This is illustrated in Fig. 34 for clean nanotubes with different helicities (Triozon *et al.*, 2005). Note that such intramolecular junctions have been experimentally observed by STM (Odom *et al.*, 2002). The reduction of transmission at the interface is general to all realistic nanoscale junctions between a nanotube and a metallic electrode, or other interface geometries leading to different charge injection capabilities.

To discuss this point, we first define two different classes of metal-nanotube junctions, namely, the metal–

metallic-nanotube–metal (M-MCNT-M) and metal–semiconducting-nanotube–metal (M-SCCNT-M) junctions. For the former case of metal-metal Ohmic contacts, that is, in situations where there is hardly any interface potential barrier to tunnel through, the contact resistance mainly depends on the local atomic bonding and orbital rehybridization at the interface. For the latter case of M-SCCNT-M junctions, several experiments suggest that CNTFETs may operate as Schottky-barrier transistors, with a very large contact resistance at low bias related to a tunneling barrier which can be tuned with the gate voltage (Heinze *et al.*, 2002; Chen, Appenzeller, Knoch, Lin, and Avouris, 2005). The charge redistribution through the interface, associated with the physics of band bending and its resulting depletion layers, and the possible occurrence of metal-induced gap states (Tersoff, 1984), are expected to depend strongly on the relative positions of the Fermi level and band edges of the metal and nanotube in contact. It is unclear, however, if these concepts, accepted for standard 3D devices, should be valid in the case of nanotubes, which can be described as either molecular objects or 1D systems. It has been shown in particular that various scaling laws, such as the length of the depletion layer as a function of dopant fraction or the interface dipole, differ significantly in 1D from their 3D analogs (Léonard and Tersoff, 1999; Heinze *et al.*, 2003).

We consider the case of a M-MCNT-M and assume that $|k_m\rangle = \Sigma_l e^{ik_m \cdot l}|\varphi_m^l\rangle$ (or $|k_F\rangle = \Sigma_l e^{i\mathbf{k}_F^l}|\varphi_{NT}^l\rangle$) are the propagating states with k_m (k_F) the wave vector in the metal (nanotube). We take $|\varphi_{NT}^l\rangle$ as the localized atomic basis orbitals (p_z like) in cell (l), which will have nonzero overlap with $|\varphi_m^{l'}\rangle$ for only a few unit cells defining the contact area [($l-l'$) small]. The scattering rate between the metal and nanotube can be qualitatively written following the FGR and will be related to $\langle k_m|\mathcal{H}_{contact}|k_F\rangle$, the coupling operator between the tube and electrodes. This matrix element is related to the chemical nature of the interface bonding (covalent, ionic, etc.) and to the overlap $\langle \varphi_{NT}^l|\varphi_m^{l'}\rangle$, which will depend strongly on the geometry and contact configuration between the nanotube and electrodes (end or side/bulk contacts, length of the contact, etc.) as illustrated in Fig. 35, together with the angular momentum of the atomic orbitals contributing to $|k_m\rangle$. The coupling is further optimized whenever wave-vector conservation is best satisfied, i.e., when $k_m \sim k_F$. For instance, in the case of metallic armchair tubes, larger coupling will be achieved for $k_m \simeq 2\pi/3\sqrt{3}a_{cc}$. A much smaller metallic wave vector will yield a small coupling rate. The tunneling rate from the metal to the nanotube is qualitatively given by

$$\frac{1}{\tau} \sim \frac{2\pi}{\hbar}|\langle k_m|\mathcal{H}_{contact}|k_F\rangle|^2\rho_{NT}(E_F)\rho_m(E_F), \qquad (33)$$

with $\rho_{NT}(E_F)$ [$\rho_m(E_F)$] the density of states of the nanotube (metal) at the Fermi level. Note that these considerations are derived for the low-bias regime.
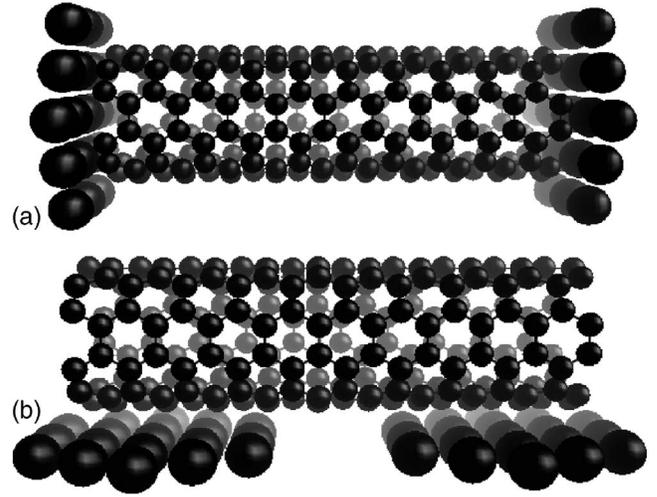
FIG. 35. Contact type between a nanotube and electrode first layers: (a) end contacts and (b) side or bulk contacts. Courtesy of J.J Palacios (Palacios *et al.*, 2003).

Intriguingly, some experiments on metallic tubes have measured only a single channel $G \simeq G_0$ at low bias, instead of the two theoretically predicted channels, assuming π-π^* degeneracy at the charge-neutrality point. Anantram (2001) and Mingo and Han (2001) have proposed an interpretation in terms of imbalanced coupling strength between the π-metal (jellium) contact and the π^*-metal contact. In Fig. 36, the contribution of both channels to the conductance at charge-neutrality point is reported as a function of nanotube length and for two different nanotube diameters. The contribution of the π^* metal is shown to almost vanish for a sufficiently large diameter.

Several theoretical papers emphasized the importance of the hybridization between carbon and metal orbitals at the contact (Nardelli *et al.*, 2001; Dag *et al.*, 2003; Palacios *et al.*, 2003; Okada and Oshiyama, 2005; Ke *et al.*, 2006; Nemec *et al.*, 2006), while other work discussed the role of the Schottky barrier (Dag *et al.*, 2003; Shan and Cho, 2004; Xue and Ratner, 2004; Okada and
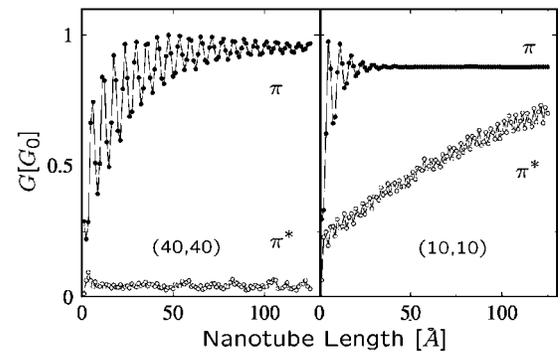
FIG. 36. Contribution of π and π^* channels at the charge-neutrality point to the total nanotube conductance for armchair (10,10) and (40,40) armchair tubes and modeling the metal contact by a jellium. Adapted from Mingo and Han, 2001.

Oshiyama, 2005; Park and Hong, 2005; Odbadrakh *et al.*, 2006; Zhu and Kaxiras, 2006). The variations in contact geometry (end, side, or melted) nanotube length, and metal type can certainly explain that the conclusions are still quite scattered. Further, while charge transfers, interface states, and the suggested modification of the Schottky barrier height by surrounding molecular dipoles (Auvray *et al.*, 2005) are expected to be well described by *ab initio* simulations, it is yet impossible to tackle with such accurate approaches micron-long tubes in the presence of a gate voltage.

Finally, for higher bias voltage between conducting probes, due to the potential drop profile along the tube, the modifications of bands along the tube axis produce additional backscattering (Anantram, 2000). This Bragg reflection is a fundamental point that could explain the experimental observation of limited turn-on current with increasing bias voltage (Frank *et al.*, 1998; Poncharal *et al.*, 2002; Urbina *et al.*, 2003).

C. Effect of disorder on transport

1. Electronic eigenstates and pseudospin symmetry

In the vicinity of the charge-neutrality point, the ballistic character of transport properties in metallic carbon nanotubes or graphene is particularly strong, owing to the linear dispersion relation in conjunction with the specific symmetry of the eigenstates. These properties have been derived within the the so-called $\mathbf{k} \cdot \mathbf{p}$ approximation (Slonczewski and Weiss, 1958; DiVicenzo and Mele, 1984). Instead of the tight-binding model, which allows one to compute the full band structure, the $\mathbf{k} \cdot \mathbf{p}$ approximation is a local description around the Fermi surface, where the Schrödinger equation is written by decomposing the Bloch states as $\Psi_{\mathbf{k}=\mathbf{K}+\delta k}(\mathbf{r}) = e^{i\delta\mathbf{k}\cdot\mathbf{r}}u_{\mathbf{K}}(\mathbf{r})$, $u_{\mathbf{K}}(\mathbf{r})$ obeying the general Bloch condition. For a given periodic potential $V(\mathbf{r})$, the Schrödinger equation can thus be simplified as (DiVicenzo and Mele, 1984)

$$\left(+ \frac{\hat{\mathbf{p}}^2}{2m} + \frac{\hbar^2\delta\mathbf{k}^2}{2m} + \frac{\hbar\,\delta\mathbf{k}\cdot\hat{\mathbf{p}}}{m} + V(\mathbf{r}) \right)u_K(\mathbf{r}) = E_{\mathbf{K}+\delta k}u_{\mathbf{K}}(\mathbf{r}), \tag{34}$$

where $\hat{\mathbf{p}} = -i\nabla$ is the momentum operator and m the electron mass. The task in the $\mathbf{k} \cdot \mathbf{p}$ approximation consists in extracting information by expanding $u_{\mathbf{k}}(\mathbf{r})$ around the Fermi level, in the same spirit as the tight-binding approximation. Ando and co-workers (Ando and Nakanishi, 1998; Ando, Nakanishi, and Saito, 1998) extended the $\mathbf{k} \cdot \mathbf{p}$ approximation to the case of metallic (armchair) nanotubes by expanding the wave functions around the $\mathbf{K}$ and $\mathbf{K}'$ points. The properties of Bloch wave functions in the vicinity of $\mathbf{K}$ points can be derived as follows. First, their Wannier representation up to a normalization factor is given by

$$\Psi_{\mathbf{k}}(\mathbf{r}) = \sum_{\ell \text{ all cells}} e^{i\mathbf{k}\cdot\ell}[b_1\Phi_A(\mathbf{r}-\ell) + b_2\Phi_B(\mathbf{r}-\ell)], \tag{35}$$

where $\Phi_{i=A,B}(\mathbf{r}) = p_z(\mathbf{r}-\mathbf{r}_{i=A,B})$ to account for the two orbitals per unit cell, whereas (b_1,b_2) describe the amplitude of the p_z orbital for the two carbon atoms in the unit cell. Then, following the definitions of Fig. 2 and using Eq. (12), the eigenstates for $\mathbf{k} = \mathbf{K} + \delta\mathbf{k}$ are derived from

$$\begin{pmatrix} E(\mathbf{k}) & -\gamma_0\alpha(\mathbf{k}) \\ -\gamma_0\alpha^*(\mathbf{k}) & E(\mathbf{k}) \end{pmatrix}\begin{pmatrix} b_1 \\ b_2 \end{pmatrix} = \begin{pmatrix} 0 \\ 0 \end{pmatrix}, \tag{36}$$

with $\alpha(\mathbf{k}) = 1 + e^{-i\mathbf{k}\cdot\mathbf{a}_1} + e^{-i\mathbf{k}\cdot\mathbf{a}_2}$. By choosing $\mathbf{K} = (4\pi/3\sqrt{3}a_{cc},0)$, one obtains $\alpha(\mathbf{k}) = 1 + e^{-2i\pi/3}e^{-i\delta k_x a/2} + e^{2i\pi/3}e^{-i\delta k_y a/2}$ and the problem is recast into

$$\begin{pmatrix} E(\delta\mathbf{k}) & 3\gamma_0 a_{cc}(\delta k_x + i\delta k_y)/2 \\ 3\gamma_0 a_{cc}(\delta k_x - i\delta k_y)/2 & E(\delta\mathbf{k}) \end{pmatrix}\begin{pmatrix} b_1 \\ b_2 \end{pmatrix} = \begin{pmatrix} 0 \\ 0 \end{pmatrix}. \tag{37}$$

The dispersion relations are found by setting the determinant to zero, $E(\delta\mathbf{k}) = \pm\hbar v_F|\delta\mathbf{k}|$ [noticing that $E(\mathbf{k}) = E(\mathbf{K}) + \delta\mathbf{k}\,\partial E/\partial\mathbf{k} = E(\delta\mathbf{k})$], whereas the eigenvectors must satisfy $b_1^2(\delta k_x - i\delta k_y) = b_2^2(\delta k_x + i\delta k_y)$. An obvious solution is $b_1 e^{-i\theta_k/2} = \pm b_2 e^{i\theta_k/2}$ [defining $\theta_k = \arctan(\delta k_y/\delta k_x)$, the angle between $\delta\mathbf{k}$ and the k_y axis which corresponds to the tube axis direction], yielding two possible choices

$$|s = \pm 1\rangle = \frac{1}{\sqrt{2}}\begin{pmatrix} s\,e^{-i\theta_k/2} \\ e^{i\theta_k/2} \end{pmatrix}, \tag{38}$$

where $s=1$ indicates positive energy, whereas $s=-1$ describes states with negative energy, with respect to the charge-neutrality point. In the basis $\{|s=1\rangle;|s=-1\rangle\}$, the Hamiltonian reads $\mathcal{H} = \hbar v_F|\delta\mathbf{k}|\sigma_z$, with σ_z the usual Pauli matrix. The Schrödinger equation in the $\mathbf{k} \cdot \mathbf{p}$ approximation can thus be viewed as a (decoupled) two-component matrix equation (one component for each sublattice), which is formally equivalent to the Dirac equation, where the spinor is not the electron spin but a pseudospin representing the sublattice. Additionally, since the energy of the bands touches E_F, the problem is analogous to a free massless neutrino on a cylinder (Ando, 2005). The vectors $1/\sqrt{2}(\pm 1,1)$ are eigenstates of σ_x with eigenvalues ± 1, and the pseudospin for a state with arbitrary vector $\delta\mathbf{k}$ is deduced by applying to $1/\sqrt{2}(\pm 1,1)$ a rotation operator with angle θ_k about the z axis [perpendicular to the tube direction; Fig. 37(c)],with the corresponding rotation matrix (Ando, Nakanishi, and Saito, 1998)

$$\mathcal{R}[\theta_k] = \begin{pmatrix} e^{i\theta_k/2} & 0 \\ 0 & e^{-i\theta_k/2} \end{pmatrix}. \tag{39}$$

Thus, finally, in the vicinity of the $\mathbf{K}$ points, the electronic wave functions can be expanded, up to some normalization factor, as

$$\Psi_{\mathbf{k}=\mathbf{K}\pm\delta\mathbf{k},s=\pm1}(\mathbf{r}) \sim \frac{1}{\sqrt{2}}\begin{pmatrix} se^{+i\theta_k/2} \\ e^{-i\theta_k/2} \end{pmatrix} e^{i(\delta k_x x + \delta k_y y)}. \qquad (40)$$

In Fig. 37 a schematic representation of eigenstates is provided for the sake of illustration. Assuming an initial Fermi energy slightly downshifted with respect to the charge-neutrality point ($s=-1$), the two available orbitals for elastic intravalley scattering are shown. The total wave function is given by $\Psi_{\mathbf{k}=\mathbf{K}\pm\delta\mathbf{k},s=-1}(\mathbf{r})$ [Eq. (40)] times the bonding or antibonding component (set as symbols in Fig. 37), which are obtained in the limit $|\mathbf{k}\rangle=|\mathbf{K}\rangle$, where $E(\mathbf{K})=0$, and which gives two degenerate eigenstates formed by either a symmetric or an antisymmetric combination of the p_z orbitals ($|\Psi_{\mathbf{K}}\rangle=\{|\mathbf{K}_+\rangle,|\mathbf{K}_-\rangle\}$):

$$\langle\mathbf{r}|\mathbf{K}_+\rangle = \sum_\ell \frac{e^{i\mathbf{K}\cdot\ell}}{\sqrt{2}}[p_z(\mathbf{r}-\mathbf{r}_A-\ell)+p_z(\mathbf{r}-\mathbf{r}_B-\ell)]$$

(π-antibonding state),

$$\langle\mathbf{r}|\mathbf{K}_-\rangle = \sum_\ell \frac{e^{i\mathbf{K}\cdot\ell}}{\sqrt{2}}[p_z(\mathbf{r}-\mathbf{r}_A-\ell)-p_z(\mathbf{r}-\mathbf{r}_B-\ell)]$$

(π^*-bonding state).

2. Long-range disorder and the absence of backscattering

If we consider an impurity bound to the surface of the tube, typically by van der Waals coupling, the impurity potential $\mathcal{U}(\mathbf{r})$ is slowly varying on the scale of the interatomic distance a_{cc}. $\mathcal{U}(\mathbf{r})$ can thus be regarded as a perturbation to the Hamiltonian $\mathcal{H}_{\mathbf{k}\cdot\mathbf{p}}$, and the matrix elements $\langle\Psi_{k,s}|\mathcal{U}(\mathbf{r})|\Psi_{k',s'}\rangle$ of the potential between the Bloch states [Eq. (40)] describe the scattering probability amplitude $\mathbf{k}\rightarrow\mathbf{k}'$ due to the single impurity, which in principle results in decreasing conductance. Such a long-range potential generally involves low momentum transfer, which guarantees the applicability of the effective mass approximation, generally ignoring interband transitions.

Assuming a long-range impurity potential, Ando *et al.* (Ando and Nakanishi, 1998; Ando, Nakanishi, and Saito, 1998) demonstrate that both intravalley ($\mathbf{k}=\mathbf{K}\pm\delta\mathbf{k}\rightarrow\mathbf{k}'=\mathbf{K}\mp\delta\mathbf{k}$ and the same changing $\mathbf{K}$ to $\mathbf{K}'$) and intervalley ($\mathbf{k}=\mathbf{K}\pm\delta\mathbf{k}\rightarrow\mathbf{k}'=\mathbf{K}'\mp\delta\mathbf{k}$ and the same changing $\mathbf{K}$ to $\mathbf{K}'$) scattering probabilities were vanishingly small. The case of intravalley scattering (say around $\mathbf{K}$) was investigated by computing the terms $\langle s,\delta\mathbf{k}|\mathcal{T}|s',\delta\mathbf{k}'\rangle$, developing the $\mathcal{T}$ matrix recursively through a Dyson equation [$\mathcal{G}=(E-\mathcal{H}_0-\mathcal{U})^{-1}$]

$$\mathcal{T} = \mathcal{U}+\mathcal{U}\mathcal{G}\mathcal{U} = \mathcal{U}+\mathcal{U}\mathcal{G}_0\mathcal{U}+\mathcal{U}\mathcal{G}_0\mathcal{U}\mathcal{G}_0\mathcal{U}+\cdots$$

$$= \mathcal{U}+\mathcal{U}\frac{1}{E-\mathcal{H}_0}\mathcal{U}+\mathcal{U}\frac{1}{E-\mathcal{H}_0}\mathcal{U}\frac{1}{E-\mathcal{H}_0}\mathcal{U}+\cdots. \quad (41)$$

In this expansion, the $\mathbf{k}\cdot\mathbf{p}$ Hamiltonian around the $\mathbf{K}$ point can be reduced to $\mathcal{H}_0=\gamma_0(\sigma_x\hat{p}_x+\sigma_y\hat{p}_y)$ (σ_x and σ_y the Pauli matrices), whereas $\mathcal{U}$ has a diagonal representation, whose elements provide the impurity potential on-site energies (Ando, Nakanishi, and Saito, 1998). The term of type $\langle s',\delta\mathbf{k}'|\mathcal{T}|s,\delta\mathbf{k}\rangle$ can be expanded on the basis of eigenstates, and one is left with

$$\langle s',\delta\mathbf{k}'|\mathcal{U}|s,\delta\mathbf{k}\rangle \simeq \mathcal{U}(\delta\mathbf{k}-\delta\mathbf{k}')(s\,e^{i\theta_k/2},e^{-i\theta_k/2})$$

$$\times\begin{pmatrix} s\,e^{-i\theta_{k'}/s} \\ e^{-i\theta_{k'}/2} \end{pmatrix}$$

$$\simeq \mathcal{U}(\delta\mathbf{k}-\delta\mathbf{k}')(ss'\,e^{-i(\theta_k-\theta_{k'})/2}$$

$$+ e^{+i(\theta_k+\theta_{k'})/2}), \qquad (42)$$

where $\mathcal{U}(\delta\mathbf{k}-\delta\mathbf{k}')=\int d\mathbf{r}\,\mathcal{U}(\mathbf{r})e^{-i(\delta\mathbf{k}-\delta\mathbf{k}')\cdot\mathbf{r}}$. The backscattering amplitude for the case ($s=s'=\pm1$) thus becomes $\langle s,\delta\mathbf{k}|\mathcal{U}|s,-\delta\mathbf{k}\rangle\simeq\mathcal{U}(2\delta\mathbf{k})\cos(\theta_k+\theta_{-k})/2=0$. This can be straightfowardly generalized to all higher-order terms in the perturbation series (Ando, Nakanishi, and Saito, 1998) given by

$$\langle s,-\delta\mathbf{k}|\hat{\mathcal{T}}(E)^p|s,+\delta\mathbf{k}\rangle \simeq \sum_{s_1k_1}\sum_{s_2k_2}\cdots\sum_{s_pk_p} \frac{\mathcal{U}(-\delta\mathbf{k}-\delta\mathbf{k}_p)\mathcal{U}(\delta\mathbf{k}_p-\delta\mathbf{k}_{p-1})\cdots\mathcal{U}(\delta\mathbf{k}_p-\delta\mathbf{k})}{[E-\varepsilon_{s_p}(\delta\mathbf{k}_p)][E-\varepsilon_{s_{p-1}}(\delta\mathbf{k}_{p-1})]\cdots[E-\varepsilon_{s_1}(\delta\mathbf{k}_1)]}$$

$$\times \langle s|\mathcal{R}[\theta_{-k}]\mathcal{R}^{-1}[\theta_{k_p}]|s_p\rangle\langle s_{p-1}|\mathcal{R}[\theta_{k_p}][R^{-1}[\theta_{k_{p-1}}]|s_{p-1}\rangle\cdots\langle s_1|\mathcal{R}[\theta_{k_1}]R^{-1}[\theta_k]|s\rangle, \qquad (43)$$

where the rotation matrix $\mathcal{R}[\theta_{k_p}]$ is defined by Eq. (39). Therefore, because of the symmetries of eigenstates, all time-reversal terms [like those illustrated in Fig. 37, bottom, (a) and (b)] cancel out, so that the total amplitude is proportional to

$$\langle s|\mathcal{R}[\theta_k]R^{-1}[\theta_{-k}]|s\rangle = \cos(\theta_k+\theta_{-k})/2, \qquad (44)$$

which equals zero since $\theta_k+\theta_{-k}=\pm\pi$ (see Fig. 37). In conclusion, to all orders in the perturbation expansion,

backscattering is suppressed in the low-energy range around the charge-neutrality point. This property has also been confirmed by numerical calculations (Ando and Nakanishi, 1998; McEuen *et al.*, 1999).

The applicability of this result is, however, restricted to metallic nanotubes, in situations of slowly varying potential, and for energy windows that shrink to zero around the charge-neutrality point as the diameter of the nanotube increases. For semiconducting tubes, these
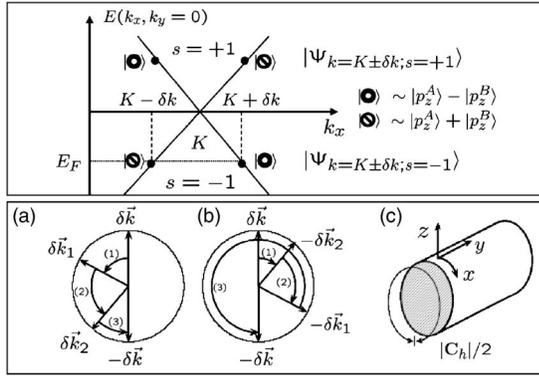
FIG. 37. Scattering states. Top panel: Representation of linear dispersion bands in the vicinity of a **K** point. The eigenstates available for scattering are pinpointed for a given Fermi level below the charge-neutrality point. Bottom panel: Schematic illustration of the pseudospin rotation corresponding to scattering processes (a) $\delta\mathbf{k} \to \delta\mathbf{k}_1 \to \delta\mathbf{k}_2 \to -\delta\mathbf{k}$ and (b) $\delta\mathbf{k} \to -\delta\mathbf{k}_2 \to -\delta\mathbf{k}_1 \to -\delta\mathbf{k}$. We choose $\theta_k = 0$ and $\theta_{-k} = \pi$. In (c), a representation of the local axis orientations with respect to the nanotube.

pseudospin properties do not apply and backscattering is found to be much stronger. This picture has been discussed on the basis of experimental data by McEuen *et al.* (1999).

3. Short-range disorder and elastic mean free path: Model analysis

For a more general and in-depth understanding of disorder effects, including interband scattering in the presence of short-range disorder, evaluation of the elastic mean free path is fundamental. For sufficiently weak disorder, a perturbative treatment can be performed within the FGR, giving direct access to the elastic mean free path $\ell_e = v_F \tau$. This was first derived by White and Todorov (1998), by reducing the band structure to a two-band approximation, as an effective model of the two degenerate bands at the charge-neutrality point for armchair nanotubes. By further considering the on-site Anderson-type disorder (see below), an analytical formula for ℓ_e was derived. ℓ_e was found to scale linearly with diameter for a fixed disorder strength, while at a fixed diameter the expected disorder scaling was shown to be $\ell_e \sim 1/W^2$, W measuring the variation range of the on-site perturbing potential. The analytical derivation of such a fundamental length scale first requires the calculation of the total density of states (DOS) in the vicinity of the Fermi level. As shown in Sec. III, the DOS is written as $\rho(E) = \frac{1}{\Omega}\text{Tr}[\delta(E - \mathcal{H})]$ where the trace has to be developed over a complete basis set. Using the DOS given by Eq. (22), application of the FGR yields

$$\frac{1}{2\tau_e(E_F)} = \frac{2\pi}{\hbar}|\langle \Psi_{n1}(k_F)|\hat{\mathcal{U}}|\Psi_{n2}(-k_F)\rangle|^2$$
$$\times \rho(E_F) N_c N_{\text{ring}} \qquad (45)$$

with N_c and N_{ring}, respectively, the number of pair atoms

along the circumference and the total number of rings taken in the unit cell used for diagonalization, whereas the eigenstates at the Fermi level are rewritten as

$$|\Psi_{n1,n2}(k_F)\rangle = \frac{1}{\sqrt{N_{\text{ring}}}} \sum_{m=1,N_{\text{ring}}} e^{imk_F}|\alpha_{n1,n2}(m)\rangle,$$

with

$$|\alpha_{n1}(m)\rangle = \frac{1}{\sqrt{2N_c}} \sum_{n=1}^{N_c} e^{2i\pi n/N_c}[|p_z^A(mn)\rangle + |p_z^B(mn)\rangle],$$

$$|\alpha_{n2}(m)\rangle = \frac{1}{\sqrt{2N_c}} \sum_{n=1}^{N_c} e^{2i\pi n/N_c}[|p_z^A(mn)\rangle - |p_z^B(mn)\rangle].$$
$$(46)$$

The disorder considered here is an uncorrelated white noise (Anderson-type) distribution given by

$$\langle p_z^A(mn)|\hat{\mathcal{U}}|p_z^A(m'n')\rangle = \varepsilon_A(m,n)\delta_{mm'}\delta_{nn'},$$

$$\langle p_z^B(mn)|\hat{\mathcal{U}}|p_z^b(m'n')\rangle = \varepsilon_B(m,n)\delta_{mm'}\delta_{nn'},$$

$$\langle p_z^A(mn)|\hat{\mathcal{U}}|p_z^A(m'n')\rangle = 0, \qquad (47)$$

where $\varepsilon_B(m,n)$ and $\varepsilon_A(m,n)$ are the on-site energies on atoms A and B in position (m,n), randomly distributed within the interval $[-W/2, W/2]$ and following some uniform distribution with probability $\mathcal{P} = 1/W$. Then by replacing Eq. (46) in Eq. (45) and using Eq. (47), a straightforward calculation gives

$$\frac{1}{\tau_e(E_F)} = \frac{\pi\rho(E_F)}{\hbar}\left(\frac{1}{\sqrt{N_c N_{\text{ring}}}} \sum_{N_c N_{\text{ring}}} \varepsilon_A^2 \right.$$
$$\left. + \frac{1}{\sqrt{N_c N_{\text{ring}}}} \sum_{N_c N_{\text{ring}}} \varepsilon_B^2 \right). \qquad (48)$$

Hence, if the disorder is described by random fluctuations of on-site energies with uniform probability $1/W$ (W the disorder bandwidth), the mean free path can finally be analytically derived as (White and Mintmire, 1998; Roche *et al.*, 2000)

$$\ell_e = \frac{18a_{cc}\gamma_0^2}{W^2}\sqrt{n^2 + m^2 + nm}. \qquad (49)$$

For the armchair $m = n = 5$ nanotube, with disorder $W = 0.2\gamma_0$, by applying Eq. (49), one finds $\ell_e \sim 560$ nm, which is much larger than the circumference length. As shown in Figs. 38 and 39, numerical studies (Triozon *et al.*, 2004) confirm the scaling law of the mean free path with the nanotube diameter close to the charge-neutrality point. For semiconducting bands, the $1/W^2$ scaling law is still satisfied, but the mean free paths are seen to be much smaller and do not scale with diameter.

Besides such analytical results, a numerical analysis of the Landauer conductance in the case of such static uniform disorder was first performed by Anantram and Govindan (1998). The conductance was found to be much more sensitive in regions of higher densities of
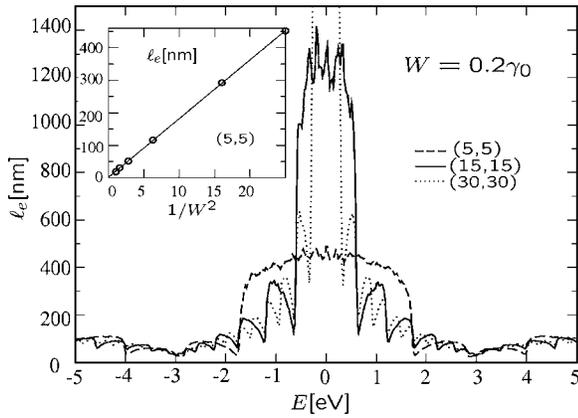
FIG. 38. Energy-dependent mean free path as a function of diameter. Inset: $1/W^2$ scaling in agreement with the Fermi golden rule. Adapted from Triozon *et al.*, 2004.

states, whereas it was almost unaffected by moderate disorder close to the charge-neutrality point (Ando and Seri, 1997).

4. Influence of doping on transport properties

The issue of doping is central to the use of CNTs in electronic devices. In particular, standard logic devices are based on *p*- or *n*-doped junctions, even though it has been proposed that a field effect could be achieved with undoped tubes thanks to a gate-voltage tuning of the Schottky barrier at the tube/electrode interface (Heinze *et al.*, 2002; Appenzeller *et al.*, 2004; Chen, Appenzeller, Knoch, Lin, and Avouris, 2005).

While the desired effect of doping in semiconducting tubes is to bring the Fermi level in (or close) to the valence or conduction bands, several theoretical works have emphasized that the perturbing potential created around an impurity in CNTs can induce a strong backscattering of the propagating wave packets at specific
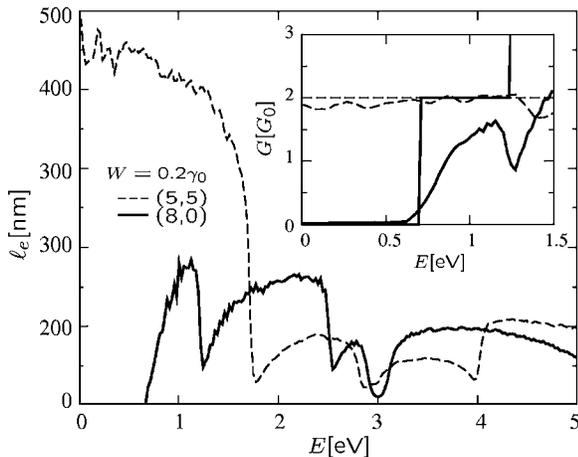
FIG. 39. Mean free paths for the metallic (5,5) and semiconducting (8,0) tubes with the same value of disorder strength. The conductance results (inset) are equivalent in both the Kubo and Landauer formalisms. Adapted from Triozon *et al.*, 2004.

energies, thus reducing the mean free path and mobility of the corresponding free carriers (Ando and Nakanishi, 1998; Ando, Nakanishi, and Saito, 1998; Choi *et al.*, 2000; Kaun *et al.*, 2002; Latil *et al.*, 2004; Mahan, 2004; Son *et al.*, 2005; Adessi *et al.*, 2006). Similar effects can be ascribed to the presence of defects such as vacancies, divacancies, or pentagon or heptagon rearrangements (Chico, Bendedict, Louie, and Cohen, 1996; Chico, Crespi, Benedict, Louie, and Cohen, 1996; Orlikowski *et al.*, 2000). This reduction of conductance occurs in particular at the energy of the (quasi)bound states (Choi *et al.*, 2000; Mahan, 2004) associated with the defects or impurities in the CNTs, leading to the terminology of resonant backscattering. The same physics of resonant backscattering has been seen in the case of doped silicon nanowires (Fernández-Serra *et al.*, 2006a, 2006b). The scaling properties of such bound states in the case of disorder and mixed B and N doping have been analyzed by Lammert and co-workers (Lammert *et al.*, 2001).

Several interesting effects related to the presence of such bound states were theoretically proposed. The position in energy of these quasibound states was shown to be strongly affected by an applied electric field with the possibility of switching the current with a transverse *E* field (Son *et al.*, 2005). Further, it was proposed that the trapping of localized states by defects or impurities should result in the formation of quantum dots along the CNT body (Chico *et al.*, 1998).

Substitutional doping by nitrogen or boron impurities has certainly been the most studied at the theoretical level (Choi *et al.*, 2000; Lammert *et al.*, 2001; Kaun *et al.*, 2002; Latil *et al.*, 2004; Son *et al.*, 2005; Adessi *et al.*, 2006). Substitutional doping by nitrogen or boron, respectively, *n*- and *p*-type dopants (Yi and Bernholc, 1993), was achieved very early, either intentionally or in several attempts to synthesize composite $B_xC_yN_z$ tubes. While incorporation of boron is found to be rather limited, at least lower than 1% which is the resolution limit of electron-energy-loss spectroscopy (EELS) chemical analysis, nitrogen is believed to be incorporated in much larger quantities with several types of bonding (threefold, pyridinelike, etc.), even though it induces at large percentage severe topological modifications (bambooshaped tubes). A thorough review of N doping has been given by Ewels and Glerup (2005).

Figure 40 shows the effect of a single N impurity on the DOS, the conductance, and the scattering phase shifts of the two eigenchannels (Choi *et al.*, 2000) for a metallic (10,10) nanotube. This work was the first *ab initio* study of doped nanotubes (within the Lippman-Schwinger approach). Even though the case of a single impurity was studied (due to computer time limitations), such *ab initio* simulations provide a unique reference that allows one to build realistic models of the scattering potential generated by dopants or defects. The contour plot (Fig. 40, right) shows the quasibound state at 0.53 eV which is at the origin of strong backscattering, whereas the rest of the spectrum is almost unaffected by the resonance.
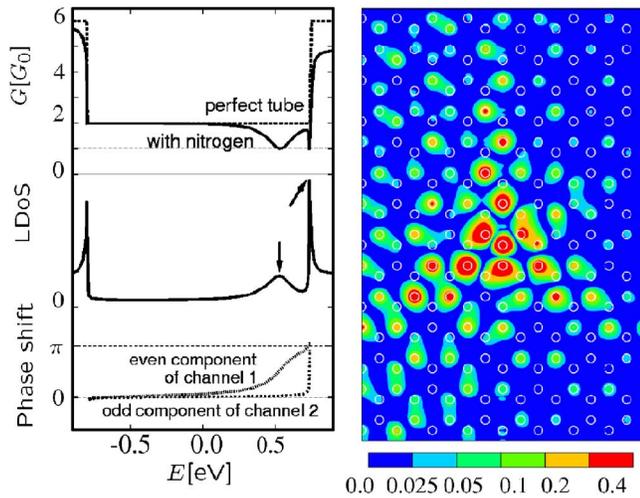
FIG. 40. (Color online) Bound states and resonant backscattering. Left: Effects of a single nitrogen impurity on conductance (top), the local density of states (middle), and the phase shift of eigenchannels (bottom) in the $(10,10)$ nanotube. Right: Contour plot of the totally reflected state at 0.53 eV. Adapted from Choi *et al.*, 2000.

While most work has focused on the effect of a single isolated defect, a few studies (Latil *et al.*, 2004, 2005; Adessi *et al.*, 2006), combining *ab initio* calculations with a semiempirical π-π^* Kubo approach to transport, have studied the effect of a random distribution of substitutional or physisorbed dopants at various concentrations for micron long tubes. Such studies allow one in particular to extract relevant mesoscopic information such as $\ell_e(E)$. In Fig. 41, the mean free path for long metallic boron-doped nanotubes is shown as a function of impurity density and CNT diameter, at a fixed Fermi energy. The downscaling of ℓ_e with impurity density and the upscaling of ℓ_e (at fixed density) with tube diameter are reproduced, showing good agreement with the FGR results derived for uniform disorder (Latil *et al.*, 2004).
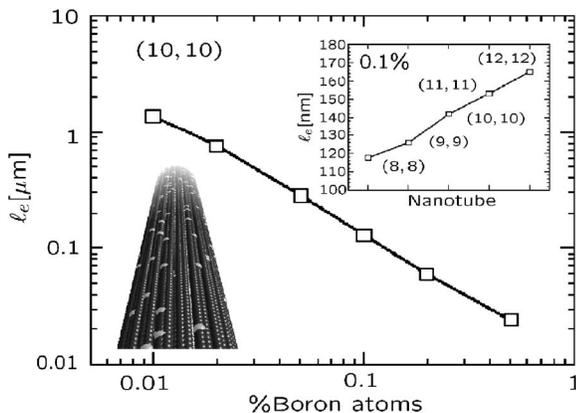
FIG. 41. Scaling of the mean free path at the Fermi level, for a B-doped (n,n) nanotube. Left: In the case of a $(10,10)$ nanotube with various boron concentrations, ℓ_e behaves like the inverse of the doping rate. Right: For a fixed concentration of B atoms, ℓ_e is a linear function of the nanotube's diameter.

In the work of Liu and co-workers (Liu *et al.*, 2001), the electronic transport of boron-doped nanotubes has been investigated experimentally. The concentration of boron atoms was evaluated to be $\simeq 1\%$ whereas the diameters of tubes were estimated in the range [17 nm, 27 nm]. Mean free paths on the order of ℓ_e $=220$–250 nm were inferred from weak-localization theory. Applying the analytical form of Eq. (49) for ℓ_e with the corresponding parameters (the dopant concentration and on-site boron energy can be mapped onto an effective W value), one finds a theoretical estimate of $\ell_e \simeq 274$ nm for the tube with diameter 17 nm, in agreement with experimental estimates. Such studies allow one to test on realistic systems previous studies performed on various models of uniform disorder (Anantram and Govindan, 1998; White and Todorov, 1998; Triozon *et al.*, 2004) and make a quantitative connection with experiments. The case of a limited number (a few tens) of realistic scattering centers was also explored for covalently functionalized (Lee *et al.*, 2005) or irradiated (Biel *et al.*, 2005; Gómez-Navarro *et al.*, 2005) tubes and it was shown again that a strong modification of the CNT atomic structure should quickly lead to a regime of Anderson localization, provided that the transport regime remains quantum-mechanically coherent (i.e., in the absence of electron-phonon or electron-electron inelastic scattering).

The large drop of the mean free path (or mobility) in substitutionally doped tubes can be partially bypassed by adopting other doping strategies. It was shown in particular that physisorption doping, where, e.g., alkalimetal atoms (Rao *et al.*, 1997; Petit *et al.*, 1999; Jouguelet *et al.*, 2000; Zhou *et al.*, 2000; Bendiab *et al.*, 2001; Derycke *et al.*, 2002; Appenzeller *et al.*, 2004; Radosavljević *et al.*, 2004) or molecules (Kazaoui *et al.*, 1999; Kong *et al.*, 2000; Kong and Dai, 2001; Takenobu *et al.*, 2003; Auvray *et al.*, 2005) are adsorbed on the tube, leads to a much larger mean free path than substitutional doping (Latil *et al.*, 2005; Adessi *et al.*, 2006). Alkali-metal atoms located either outside or inside CNTs act as donor impurities (Miyamoto *et al.*, 1995; Rubio *et al.*, 1996) while halogen atoms, molecules, or chains act as acceptors (Rao *et al.*, 1997; Grigorian *et al.*, 1998; Kazaoui *et al.*, 1999; Fan *et al.*, 2000). As yet another example, fullerenes or metallofullerenes, encapsulated inside CNTs, have been used to tune the band gap and/or Fermi level of the host tube (Smith *et al.*, 1998; Hirahara *et al.*, 2000; Hornbaker *et al.*, 2002; Lee *et al.*, 2002). Endohedral doping, that is, intercalation inside the tubes, is expected to allow for good structural stability as the atoms and molecules are not expected to desorb upon increasing temperature.

Several issues are still under debate. It has been observed that as-grown tubes present naturally a *p*-type behavior in CNTFETs (Martel *et al.*, 1998). The presence of holes has been ascribed either to charge transfer from metallic electrodes (Martel *et al.*, 1998; Tans *et al.*, 1998) or to the presence of oxygen adsorbed on the tube (Collins *et al.*, 2000; Kong *et al.*, 2000; Sumanasekera *et al.*, 2000). Another important issue is related to the exis-

tence or not of a Schottky barrier at the tube/electrode interface. From this perspective, it is not clear if the change in CNTFET characteristics upon doping is related to a modification of the intrinsic properties of the tube or of the Schottky barrier at the tube/electrode interface (Derycke *et al.*, 2002; Appenzeller *et al.*, 2004; Radosavljević *et al.*, 2004; Auvray *et al.*, 2005).

To conclude this section, we emphasize that the issue of doping by physisorption of molecules, or more generally the modification of the electronic properties of CNTs by molecular adsorption, is at the heart of a growing and potentially important field, namely, that of chemical sensors based on CNTs (Wong *et al.*, 1998; Baughman *et al.*, 2000; Collins *et al.*, 2000; Kong *et al.*, 2000; Giannozzi *et al.*, 2003; Peng and Cho, 2003; Jhi *et al.*, 2005). The key issue for such devices is selectivity and sensitivity; namely, can we distinguish from the CNT *I*/*V* modifications upon molecular adsorption between two different donor (or acceptor) molecules, and what minimum adsorbate concentration is needed to induce a measurable effect on the conductance. The 1D character of CNTs and the large variation of conductance discussed above in the case of substitutional doping clearly suggest that such a device should present unprecedented sensitivity. The sensing properties of CNTs can be further modified or tailored by covalent functionalization. While many experimental syntheses of covalently functionalized CNTs have been performed (Wong *et al.*, 1998; Bahr *et al.*, 2001; Shim *et al.*, 2001; Chiu *et al.*, 2002; Kamaras *et al.*, 2003; Strano *et al.*, 2003), the theoretical investigation of the related electronic and transport properties is still in its infancy (Chiu *et al.*, 2004; Lee *et al.*, 2005).

5. Multishell conduction

Multiwalled nanotubes or bundles of single-walled nanotubes present additional geometrical complexity due to the coupling between shells, yielding multishell transport. Multiwalled nanotubes are made of a few to tens of shells with random helicities weakly coupled through van der Waals interactions and weak electronic delocalization (Charlier *et al.*, 1994). The intershell coupling can be determined within a tight-binding scheme by keeping one $p_\perp$ orbital per carbon atom, zero on-site energies, constant nearest-neighbor hopping on each layer n, and some effective hopping form for describing neighboring-shell π-π coupling (Charlier and Michenaud, 1993; Saito *et al.*, 1993; Lambin *et al.*, 2000), leading to the following Hamiltonian:

$$\mathcal{H} = \gamma_0 \left[\sum_{i,j} |p_\perp^j\rangle\langle p_\perp^i| \right] - \beta \left[\sum_{i,j} \cos(\theta_{ij}) e^{-(d_{ij}-a)/\delta} |p_\perp^j\rangle\langle p_\perp^i| \right], \quad (50)$$

where θ_{ij} is the angle between $p_\perp^i$ and $p_\perp^j$ orbitals and d_{ij} denotes their relative distance. Typical parameters are $\gamma_0 = 2.9$ eV, $a = 3.34$ Å, and $\delta = 0.45$ Å. The difference between SWNTs and MWNTs stems from the parameter β.

An *ab initio* estimate gives $\beta \simeq \gamma_0/8$, which enables wave packets to redistribute among the different shells of the MWNT (Lambin *et al.*, 2000). Topologically speaking, two kinds of multiwall nanotube can be constructed.

The first class is made from nanotubes whose helicities allow for commensurability between shells. As a result the full MWNT is a periodic object defined by a single unit cell. This is, for instance, the case for (5,5)@(10,10) formed by two armchair metallic tubes or (6,4)@(12,8)@(18,12), which consists of two semiconducting shells enclosed by a metallic one. Indeed, $|\mathbf{T}_{(5,5)}| = |\mathbf{T}_{(10,10)}| \simeq 2.459$ Å whereas $|\mathbf{T}_{(6,4)}| = |\mathbf{T}_{(12,8)}| = |\mathbf{T}_{(18,12)}| \simeq 18.79$ Å, so that all shells in the MWNT have the same translational vector unit along the common axis.

In contrast, in MWNTs such as (6,4)@(10,10)@(17,13) there exists an intrinsic incommensurability between shell registries. Indeed, the translational vectors along each shell are, respectively, $|\mathbf{T}_{(6,4)}| = 3\sqrt{19}a_{cc}$, $|\mathbf{T}_{(10,10)}| = \sqrt{3}a_{cc}$, and $|\mathbf{T}_{(17,13)}| = 3\sqrt{1679}a_{cc}$, so that the ratios of the lengths of the individual shell translational vectors become irrational numbers and no unit cell can be defined.

As a consequence, depending on the individual shell helicity, one can obtain either translationnally invariant or aperiodic objects. The weak electronic coupling between neigbhoring shells thus defines the possibility of very different intertube coupling and charge-transfer characteristics, whose consequences on electronic band structure and transport properties are discussed in the next section.

a. Commensurate multiwalled nanotubes

Since commensurate MWNTs are periodic objects with a well-defined unit cell, the Bloch theorem applies and their band structures can be easily computed. Given that shells interact only weakly, the conductance spectrum of a MWNT in the ballistic conduction regime is given as the sum of all conducting channels at a given energy (Fig. 42). Accordingly, a very small intrinsic resistance is expected at E_F for a metallic MWNT, provided ballistic conduction is established and the charge is allowed to explore all available conducting channels. However, as discussed below, at various energies an intershell interaction might be at the origin of the stepwise reduction of conduction channels. We consider a generic MWNT made of coaxial metallic shells with perfect commensurability, namely, armchair double-walled (5,5)@(10,10) and triple-walled (5,5)@(10,10)@(15,15) nanotubes. Such MWNTs have a fivefold common symmetry. Their respective orientation might also possess additional symmetry planes perpendicular to the tube axis. In that case, the interwall interaction yields no changes over the whole spectrum, which is a superposition of independent spectra. At the charge-neutrality point the conductance should thus be $G = 6G_0$. However, if the symmetry is lowered by disorienting (rotationally and translationally) one nanotube with respect to another, then splitting of the degeneracy occurs and pseudogaps are formed (Kwon and Tománek, 1998;
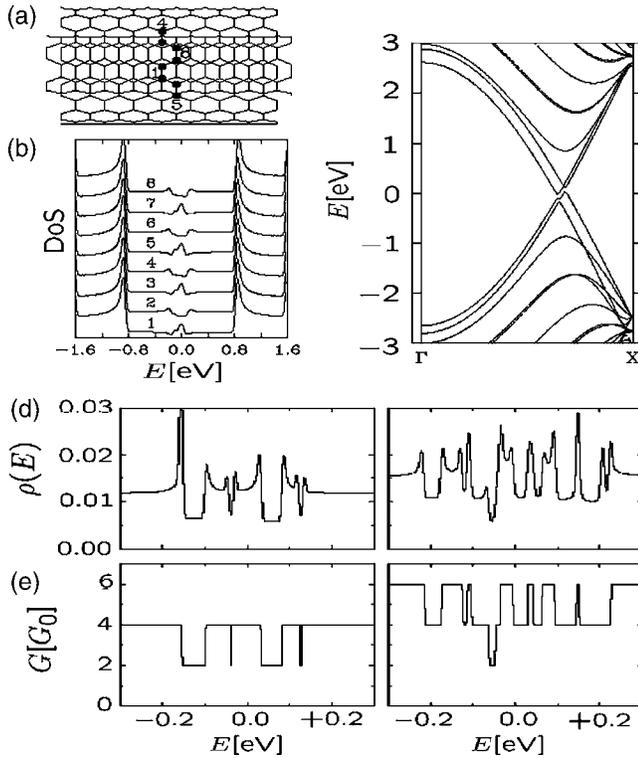
FIG. 42. Effect of the rotational symmetry breaking for a commensurate (5,5)@(10,10)@(15,15) MWNT on (a) its electronic properties, (b) its DOS, and (c) its band structure. Adapted from Lambin *et al.*, 2000. Pseudogaps (d) and associated conductance spectra (e) for (5,5)@(10,10)@(15,15). Adapted from Sanvito *et al.*, 2000.

Lambin *et al.*, 2000). Figure 42 illustrates such a phenomenon.

The presence of pseudogaps in the density of states has direct consequences on the available energy-dependent conduction channels. As shown by Sanvito and co-workers (Sanvito *et al.*, 2000), the conductance is reduced at the charge-neutrality point. One notes that this effect of intershell interaction is, however, specific to rotational disorientations of neighboring shells with C_{5h} symmetry. Other commensurate MWNTs such as (6,6)@(11,11) with no C_{5h} symmetry will not be sensitive to this phenomenon.

b. Incommensurate multiwalled nanotubes

The case of incommensurate shells is even more intriguing and challenging, since the Bloch theorem is no longer applicable, owing to the lack of translational invariance along the MWNT axis. To ascertain the intrinsic quantum transport properties in these incommensurate systems, it is necessary to investigate how propagating wave packets are sensitive to the intershell π-π orbital coupling.

Analysis of the time-dependent evolution of an electronic wave packet initially localized in the outer shell is a first instructive step. This is achieved by solving the time-dependent Schrödinger equation. In a commensurate system, some redistribution of the weight of the
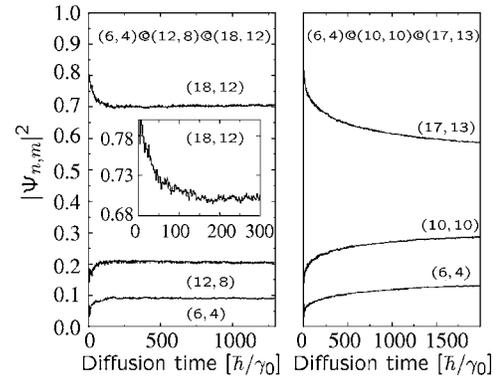
FIG. 43. Time-dependent evolution of total wave-function probability on a given shell (m,n) of a multiwalled nanotube, if at initial time $(t=0)$ the wave packet is fully localized in the outer shell. Left: Commensurate case (6,4)@(12,8)@(18,12), with a close-up of the situation for shell (12,8) in the inset. Right: Incommensurate case (6,4)@(10,10)@(17,13).

wave packet on each inner shell was numerically found to occur at a time scale $\tau_{ll} \sim \hbar \gamma_0 / \beta^2$ defined by the intershell coupling strength and well understood within the Fermi golden rule. This is illustrated in Fig. 43 where the redistribution of a wave packet initially localized in the outer shell is shown (Roche *et al.*, 2001a). From those results, one can estimate that for a source-drain spacing of the order of $\sim 1 \ \mu$m, the ballistic time of flight $\sim 4500 \hbar / \gamma_0$ will be two orders of magnitude larger than τ_{ll} (for $\beta = \gamma_0/8$), which points toward the important contribution of multishell conduction.

Nevertheless, the nature of the intrinsic conduction regime has been strongly debated, with some numerical works in favor of a negligible contribution of intershell scattering for charge energies at the charge-neutrality point, whatever the underlying aperiodic potential (Yoon *et al.*, 2002; Mayer, 2005; Uryu and Ando, 2005). In contrast, by studying numerically the quantum dynamics of wave packets over a larger range of energies, the situation was found to become more complex, with a general *nonballistic* regime, described by $\sqrt{\mathcal{D}(t)t} \sim \mathcal{A}t^{\eta}$ (Roche *et al.*, 2001a; Triozon *et al.*, 2004). The coefficient η is found to decrease from 1 to $\sim 1/2$ depending on the degree of registry mismatch between neighboring shells and the energy of the charge carriers (Roche *et al.*, 2001b). Figure 44 shows, at several energies, the time dependence of the diffusion coefficients for the incommensurate (6,4)@(17,0)@(15,15) and commensurate (5,5)@(10,10)@(15,15) MWNTs (Triozon *et al.*, 2004). Whatever the Fermi energy of the wave packets, the conduction remains ballistic in a defect-free commensurate MWNT. In contrast, for incommensurate systems, depending on the considered energy of charge carriers and the resulting hybridization strength between neighboring shells, charge conduction displays a general power-law behavior of $\mathcal{D}(t)$. This anomalous diffusion yields a specific length scaling of conductance as shown in Fig. 44 (right frame). At the charge-neutrality point, wave packets essentially remain confined to the outer
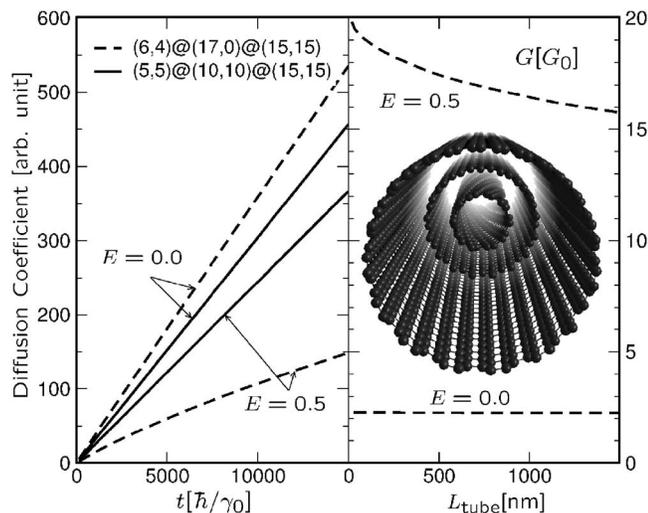
FIG. 44. Time-dependent diffusion coefficient for incommensurate and commensurate disorder-free MWNTs (with $\beta = \gamma_0/8$). Right: Length dependence of conductance for two Fermi energies for (6,4)@(17,0)@(15,15). Adapted from Triozon *et al.*, 2004.

shell as they spread in time and the carrier motion remains ballistic with a quantized conductance $G = 4e^2/h$. In contrast, at energy $E = 1.5$ eV, $G(L) \sim (2e^2/h) \times (L/L_0)^{(\eta-1)/\eta}$, with L_0 (or η) an energy-dependent characteristic length (exponent). This anomalous length scaling of the conductance has been obtained numerically using both Kubo and Landauer calculations (Triozon *et al.*, 2004; Chen and Yang, 2005).

Recently, Wang and Grifoni (2005) have succeeded in investigating analytically the electronic scattering rate of electrons propagating in the outer shell of a double-walled nanotube, due to an effective aperiodic potential produced by the inner shell, and treated perturbatively. General helicity-dependent selection rules were analytically established, and in the case of incommensurate shells the contribution of the coupling to the inner shell was shown to yield a diffusive regime in the outer shell, allowing for the extraction of an elastic mean free path ℓ_e. This elastic length scale was found to decrease with increasing energy, showing a systematic strong suppression at each new subband onset. For the (9,0)@(10,10) CNT, the mean free path in the outer shell at the charge-neutrality point was found to be of the order of $\ell_e \sim 20$ μm and decreasing by one order of magnitude for each higher subband.

The occurrence of a diffusive regime and intrinsic elastic mean free path due to intershell multiple-scattering phenomena was also confirmed by numerical calculations on double-walled (9,0)@(10,10) and triple-walled (6,4)@(17,0)@(15,15) nanotubes (Wang *et al.*, 2006). This novel fundamental elastic length scale (ℓ_e), which results from the intrinsic aperiodicity of objects with a high degree of crystallinity, is unprecedented in mesoscopic physics.

Experiments on boron-doped MWNTs have reported on the anomalous scaling of the conductance (Krstić *et*

al., 2003). However, the obtained exponent $\eta \sim 1/2$, pointing toward a diffusive regime, could not be unambiguously attributed to multishell conduction, owing to the superimposed contribution of chemical disorder. Some estimation of the intershell resistance of ~ 10 kΩ μm was performed (Bourlon *et al.*, 2004), and although its value was found to be very small, this evidences the contribution of multishell conduction in real experiments. Finally, it has been recently possible to fully characterize the chiral indices of individual shells of double-walled nanotubes by means of electron diffraction (Hirahara *et al.*, 2006). This geometrical determination of shell helicities in conjunction with transport measurements (Kociak *et al.*, 2002) opens novel perspectives for an in-depth exploration of conductance scaling properties in these objects.

c. Crossed carbon nanotubes junctions, bending and twisting deformations

Crossed nanotube junctions result from interacting individual SWNT shells, which are either present in bundles, on ropes of compacted nanotubes or intentionally manufactured for a given application purpose. In crossed-tube junctions, the intertube distance can to a certain extent be controlled by applying pressure, for instance, by means of an atomic force microscope (AFM) tip. As a result, a change in the overlap of neighboring-shell wave functions is induced by structural deformations. This was analyzed by Yoon and co-workers (Yoon *et al.*, 2001), who performed first-principles calculations of armchair-based crossed-tube junctions, and found that the intertube conductance fluctuations was on the order of $\simeq (0.1-0.2)G_0$ depending on the applied contact force, roughly a few to about 15 pN (Fig. 45).

On the other hand, the effect of structural distortions on the electronic and transport properties has also been investigated. Electronic band structure calculations showed that progressive bending of CNTs results in a decrease of the transmission coefficient in certain energy ranges [Fig. 46(a)], where curvature-induced σ-π hybridization effects produce localized states and strongly enhanced backscattering (Rochefort *et al.*, 1999; Lammert *et al.*, 2000). Similarly twisting operations were also shown to produce band-gap openings in otherwise gapless metallic armchair nanotubes, with particular band-gap oscillations depending on the twisting angle [Fig. 46(b)].

D. Quantum interference effects

1. Weak localization and the Aharonov-Bohm effect

Weak localization is a quantum interference phenomenon that develops beyond the length scale of the elastic mean free path, provided the wave function maintains its phase coherence (Altshuler *et al.*, 1981). From quantum mechanics, the quantum transmission between two chosen points in real space, let us say P and Q, generally reads
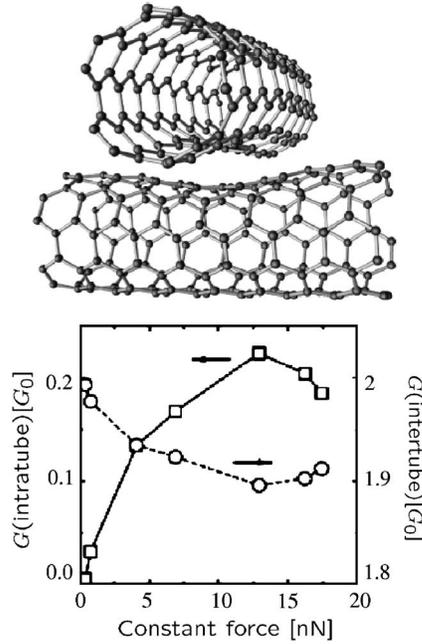
FIG. 45. Calculated intratube and intertube conductances as a function of the contact force for a (5,5) crossed junction. Solid (dashed) lines and left (right) y axis indicate intertube (intratube) conductances. Top: Structural relaxation of the (5,5) crossed CNT junction with a 15-nN contact force. Adapted from Yoon *et al.*, 2001.

$$G = \frac{2e^2}{h} \mathcal{P}_{P \to Q}, \qquad (51)$$

where $\mathcal{P}$, which is the probability for an electronic wave packet to go from one site P to another Q, can be further expanded as
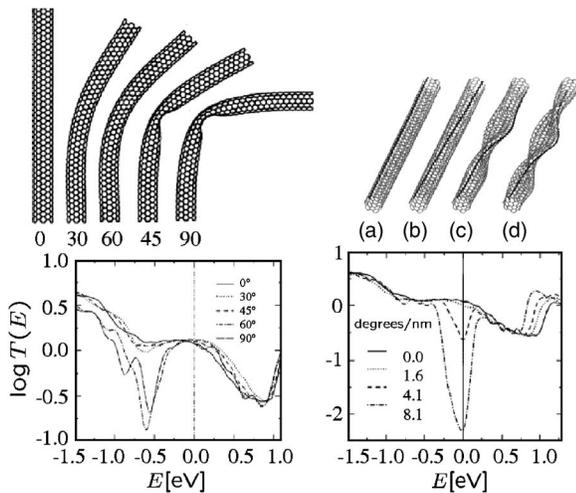
FIG. 46. Transmission coefficient as a function of Fermi level for isolated bent (6,6) nanotubes with increasing bending angle (left) or for twisted models of distortions (right). Upper drawings show the corresponding nanotube structures. Adapted from Rochefort *et al.*, 1999.

$$\mathcal{P}_{P \to Q} = \sum_i |\mathcal{A}_i|^2 + \sum_{i \neq j} \mathcal{A}_i \mathcal{A}_j e^{i(\alpha_i - \alpha_j)}, \qquad (52)$$

defining $\mathcal{A}_i e^{i\alpha_i}$ as the probability amplitude to go from P to Q via the i path. In order to extract the main universal transport features of a given disordered system, an average over a statistical distribution of random configurations has to be performed. In this averaging process, most of the interference terms in the second summation will vanish. However, two scattering events (paths) topologically returning back to the origin (clockwise and counterclockwise) will yield a constructive contribution of quantum interferences, thus reducing the absolute conductance compared to its classical value. For these paths with topological symmetry, the probability of return to the origin is written as

$$\mathcal{P}_{O \to O} = |\mathcal{A}_+ e^{i\alpha_+} + \mathcal{A}_- e^{+i\alpha_-}|^2 = 4|\mathcal{A}_0|^2, \qquad (53)$$

which thus enhances the classical value by a factor of 2. To compute the total quantum correction (δG_{WL}) due to weak-localization effects, one has to integrate over the whole class of such paths, so that

$$\delta G_{WL} \sim \frac{2e^2 D}{h} \int_0^\infty \mathcal{P}_{O \to O}(t)(e^{-t/\tau_\phi} - e^{-t/\tau_e}). \qquad (54)$$

The quantum correction is thus phenomenologically given by the integrated probability of return to the origin between the elastic scattering time τ_e and coherence time τ_ϕ. The coherence time is the time scale that limits the contribution of quantum interference effects. It originates from the intrinsic decoherence mechanisms between clockwise and counterclockwise paths, which are driven by the coupling of the quantum phase to a time-dependent fluctuating potential mimicking either a fluctuating electromagnetic field or a phonon bath (Chakravarty and Schmid, 1986). Applying a magnetic field is a powerful tool for unveiling these quantum interference effects. Indeed, switching on a magnetic field breaks the time-reversal symmetry between these paths, resulting in an increase of conductance or decrease of resistance (negative magnetoresistance). Another magnetic-field-induced quantum interference effect in a ring or cylinder geometry is the modulation of resistance with period $\phi_0/2$. The phase factor can then be written as (**A** is the vector potential)

$$\alpha_\pm = \pm \frac{e}{\hbar c} \oint \mathbf{A} \cdot d\mathbf{r} = \pm \frac{2\pi}{\phi_0} \oint \mathbf{A} \cdot d\mathbf{r}, \qquad (55)$$

and so the amplitude is given by $|\mathcal{A}|^2 |1 + e^{i(\alpha_+ - \alpha_-)}|^2$, resulting in a modulation factor $\cos(2\pi\phi/\phi_0)$. This phenomenon was first reported in carbon nanotubes by Bachtold and co-workers (Bachtold *et al.*, 1999).

a. Application to metallic (armchair) carbon nanotubes

Here the weak-localization phenomena in metallic carbon nanotubes are illustrated, on the basis of numerical results (Roche *et al.*, 2001a). The behavior of the field-dependent diffusion coefficient $\mathcal{D}(\tau_\phi, \phi/\phi_0)$ is shown in Fig. 47 for the (9,0) nanotube as a function of
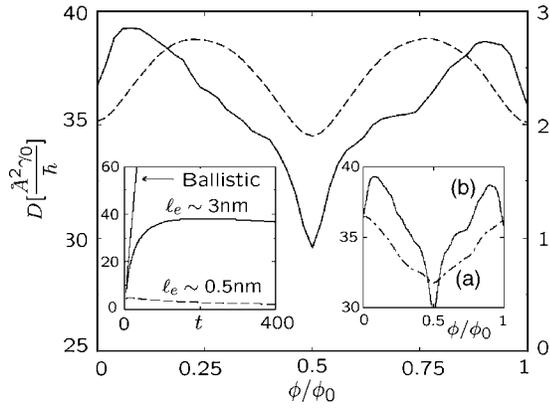
FIG. 47. Diffusion coefficient $\mathcal{D}(\tau_\phi, \phi/\phi_0)$ (in units of $\text{Å}^2\gamma_0/\hbar$) for the (9,0) nanotube evaluated at time $\tau_\phi \gg \tau_e$ for two disorder strengths $W/\gamma_0 = 3$ and 1 such that the mean free path ($\ell_e \sim 0.5$ and 3 nm, respectively) is either shorter (dashed line) or longer (solid line) than the nanotube circumference ($|\mathcal{C}_h| \sim 2.3$ nm). The right y axis is for the dashed line, and the left y axis is for the solid line. Inset: $\mathcal{D}(\tau_\phi, \phi/\phi_0)$ for $\ell_e = 3$ nm and $L(\tau_\phi) < 2\ell_e$.

ℓ_e using Eq. (49). By using Anderson-type disorder, the value of ℓ_e can be tuned by the disorder strength W and several situations of interest can be explored.

First, the weak-localization regime (Altshuler *et al.*, 1981) is analyzed under the condition $\ell_e < |\mathcal{C}_h| < L(\tau_\phi)$. Figure 47 shows that the diffusivity increases at low fields (negative magnetoresistance) and that the periodic Aharonov-Bohm oscillations are dominated by a $\phi_0/2$ period, i.e., $\mathcal{D}(\tau_\phi, \phi + \phi_0/2) = \mathcal{D}(\tau_\phi, \phi)$ in agreement with weak-localization theory. In contrast, when $\ell_e > |\mathcal{C}_h|$, $L(\tau_\phi < 2\ell_e)$, the system exhibits a positive magnetoresistance associated with $\mathcal{D}(\tau_\phi, \phi + \phi_0) = \mathcal{D}(\tau_\phi, \phi)$. For the case $\ell_e > |\mathcal{C}_h|$, $L(\tau_\phi > 2\ell_e)$, negative magnetoresistance and Aharonov-Bohm oscillations with period ϕ_0 are obtained. Note that, with the analytical formula for the mean free path and estimates of disorder values, one gets $\ell_e \simeq 10^4 |\mathcal{C}_h|$, where $|\mathcal{C}_h|$ is the circumference of the outer nanotube in the experiment of Bachtold and co-workers (Bachtold *et al.*, 1999). This leads to some inconsistency since the theoretical value of the mean free path is *a priori* too large to be consistent with a $\phi_0/2$ Aharonov-Bohm oscillation. In that respect, an important observation is that the magnetic field amplitude needed to observe conventional weak localization also strongly modifies the band structure, with a ϕ_0-periodic oscillation of 1D band positions as discussed in Sec. III.E.2. Although the band-gap opening and oscillations, as well as other band structure changes (Van Hove singularity splitting and shifting), are likely to be smoothed by disorder, the magnetofingerprints will obviously result from an entangled situation, which goes much beyond the conventional theory of weak localization (Altshuler *et al.*, 1981). Several early experiments suggested such additional complexity in analyzing magnetotransport measurements (Fujiwara *et al.*, 1999; Fedorov *et al.*, 2005). Roche and Saito (2001) theoretically found that,

for a fixed disorder strength, magnetotransport fingerprints present strong fluctuations as a function of Fermi level position, CNT diameter, and orientation of the magnetic field with respect to the tube axis. Thanks to the engineering of efficient electrostatic gating of the nanotube, some experimental evidence of such multiple Aharonov-Bohm effects, with a $\phi_0/2$ oscillation driven by weak localization superimposed on to ϕ_0-periodic resistance fluctuations related to band structure modulations, have been reported (Stojetz *et al.*, 2006).

The issue of the weak-localization regime in chemically disordered carbon nanotubes has been investigated recently for the case of boron (Latil *et al.*, 2005) and nitrogen doping (Avriller *et al.*, 2006). For an axial magnetic field, the interplay between field-dependent band structures and quantum interference effects was shown to induce strong electron-hole asymmetry of the magnetoresistance patterns. For a given chemical impurity concentration and at a finite magnetic flux threading the initially metallic nanotube, the contribution of boron-induced quasibound states was found to induce strong localization effects for hole transport; in contrast, electron transport remains weakly affected by disorder, with quasiballistic conduction (Latil *et al.*, 2005). In the case of a magnetic field applied perpendicular to the nanotube axis, an upward shift in energy of the nitrogen-induced quasibound states was found to be driven by the field intensity, with large magnetoresistance fluctuations resulting under small Fermi level shifts (Avriller *et al.*, 2006).

Finally, some spectacular energy-dependent behavior of the coherence length and elastic mean free path could also be measured (Stojetz *et al.*, 2005). The obtained energy dependence of ℓ_e was in full agreement with theoretical results (Triozon *et al.*, 2004). Roche and co-workers (Roche *et al.*, 2005a) further studied the energy dependence of the coherence length by computing the total Kubo conductance in nanotubes in the presence of both static disorder (Anderson type) and a time-dependent fluctuating potential (resulting from phonon induced atomic displacement field). By evaluating both the full Kubo conductance and its classical value, the quantum correction could be deduced,

$$\delta G_{WL}(E) = 2\frac{e^2}{h}\frac{N_\perp \ell_e(E)}{L(E,t)} - G(E), \qquad (56)$$

and the energy dependence of $L_\phi(E)$ in the weak-localization regime could be extrapolated on the basis of the conventional phenomenology, i.e., $L_\phi(E) = \delta G_{WL}(E)/L(E,t)$ and $\tau_\phi(E) = L_\phi^2(E)/[\nu(E)\ell_e(E)]$, where $L(E,t)$ corresponds to the relevant length scale entering in the Kubo normalization factor. In Fig. 48, various contributions to the conductance are shown for two selected values of static disorder and acoustic phonon modulation (twist mode). $L_\phi(E)$ and $\tau_\phi(E)$ are seen to decrease at each onset of new subbands, in agreement with experiments (Stojetz *et al.*, 2005). Further, for a fixed energy $L_\phi(E)$ downscales with increasing static disorder potential. For Anderson-type on-site disorder, one
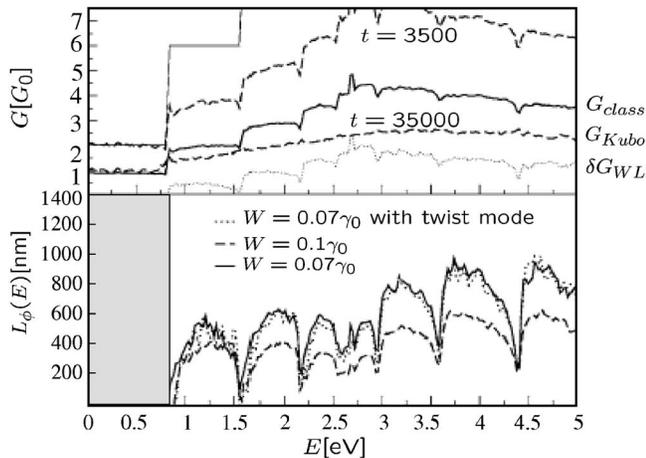
FIG. 48. Quantum conductance and coherence length in disordered nanotubes. Top: Computed Kubo conductance for a weakly disordered (10,10) nanotube for two time scales [$t = (3500, 35\,000)\hbar/\gamma_0$], together with the classical value and the deduced quantum correction. Bottom: Coherence length $L_\phi(E)$ for two values of static disorder and acoustic phonon modulation (twist mode). Adapted from Roche *et al.*, 2005b.

gets $L_\phi(W=0.1\gamma_0) \sim 75$–400 nm, whereas $L_\phi(W=0.2\gamma_0) \sim 50$–200 nm and $L_\phi(W=0.5\gamma_0) \sim 20$–50 nm.

In the case of multiwalled carbon nanotubes, the situation becomes even more complicated. First, each shell has a different diameter, with a difference of ~ 3 Å between neighboring shells. So for a given ϕ_0 flux threading one given shell, neighboring shells will be sensitive to either Larger or smaller flux, leading to multiple contributions of incommensurate Aharonov-Bohm oscillation periods. In addition, even if the MWNTs are free from any other source of contamination, the incommensurability between neighboring shells produces an underlying aperiodic potential for π-electron motion, as explained in Sec. IV.C.5. This phenomenon was shown to be at the origin of various energy-dependent magnetotransport fingerprints, such as ϕ_0-periodic magnetoresistance oscillations at certain energies, that will transform into $\phi_0/2$ oscillations for a shifted Fermi level position (Roche *et al.*, 2001a; Triozon *et al.*, 2004).

2. From weak to strong localization

In low-dimensional systems, the relation between the mean free path and the localization length is an important issue. Thouless (1973) derived the simple relation $\xi = 2\ell_e$ between the two quantities in strictly 1D systems. By means of random matrix theory (Beenakker, 1997) this result was generalized for quasi-1D systems with a large number of conduction channels $\xi \sim N_\perp \ell_e$. For transport regimes that are said to be ergodic, the average properties do not depend on the precise nature of the underlying disorder, but are predicted to be driven by the universal symmetry class of the Hamiltonian; that is, $\xi = \frac{1}{2}\{\beta(N_\perp - 1) + 2\}\ell_e$, with $\beta = 1$ if the Hamiltonian is symmetric under the time-reversal operator and $\beta = 2$ otherwise.

In metallic carbon nanotubes at the charge-neutrality point, assuming uniform Anderson-type disorder (with strength W), the localization length is thus expected, at zero field, to be given by $\xi(E=0) = (36a_{cc}\gamma_0^2/W^2)\sqrt{n^2 + m^2 + nm}$, and will consequently also scale linearly with the tube diameter for low disorder (Roche *et al.*, 2000; Hjort and Stafström, 2001; Jiang *et al.*, 2001). Its experimental observation assumes that an exponential increase of the resistance develops from a certain nanotube length L, i.e., $G \simeq (2e^2/h)\exp(-L/\xi)$, and the localization length $\xi(E)$ is predicted to be energy dependent, with a systematic decrease at each onset of new subbands, following the mean-free-path pattern.

Some evidence of Anderson localization has been obtained experimentally (Shea *et al.*, 2000; Gómez-Navarro *et al.*, 2005). First, Shea and co-workers studied low-temperature magnetotransport in a ring of a rope of SWNTs. Although a weak-localization signature was observed for $T \geq 3$ K, a drastic resistance increase was measured below 1 K, with strong departure of magnetoresistance behavior from weak-localization theory. No clear understanding of the origin of localization or its intrinsic features could be achieved. More recently, Gómez-Navarro and co-workers (Gómez-Navarro *et al.*, 2005) reported an exponential increase of the resistance in Ar$^+$-irradiated carbon nanotubes. By tuning the ion irradiation time exposure to enhance the defect density (assigned to bivacancies), the resulting resistance increase was analyzed in terms of decreasing localization length. These measurements were supported by *ab initio* calculations (Biel *et al.*, 2005), giving the first direct evidence of a metal-insulator transition in quasi-1D systems.

Other recent work has further theoretically investigated simultaneously both the elastic mean free path and the localization length (Avriller *et al.*, 2006) for a realistic model of chemical disorder (substitutional nitrogen impurities). The Thouless relationship between the two was confirmed in the absence and presence of an external magnetic field (Thouless, 1977) and in agreement with the theoretical predictions of random matrix theory (Beenakker, 1997).

E. Inelastic scattering

1. Electron-phonon coupling

Discussion of the vibrational properties of nanotubes would require a full review that is beyond the scope of the present work. However, some aspects of the electronic and transport properties of nanotubes cannot be understood without treating the coupling of electrons with phonons. Such aspects include (nonexhaustively) the charge density wave or superconducting instability of the Fermi sea (Sec. IV.F), the inelastic scattering of electrons by phonons in a transport experiment (Sec. IV.E.2), the Raman intensities, and the relaxation of hot electrons in an optical experiment. Thorough reviews or papers on the phonon properties in CNTs can be found in the literature (Sánchez-Portal *et al.*, 1999; Dresselhaus
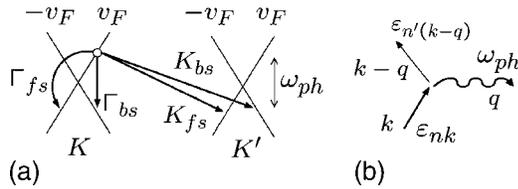
FIG. 49. Electron-phonon scattering processes. (a) Symbolic scattering processes (phonon emission): Γ_{bs} and Γ_{fs} are zone-center (intravalley) backward and forward scattering, while K_{bs} and K_{fs} are zone-boundary (intervalley) backward and forward processes. (b) Symbolic phonon emission process with the energy and momentum of the initial and final electron and phonon states.

FIG. 51. Band gap opening by optical phonons. (a) Displacement pattern of the longitudinal (transverse) A_1 mode in a zigzag (armchair) tube. Band structure for a metallic zigzag tube in (b) the equilibrium positions and (c) for the distortion compatible with the $A_1(L)$ mode. Adapted from Dubay *et al.*, 2002.

and Eklund, 2000; Dubay and Kresse, 2003). A review of the role of electrons and phonons in CNT Raman spectra can be found in Dresselhaus *et al.* (2005).

As an introductory remark to electron-phonon coupling (EPC), we note that conservation of energy and momentum imposes that only zone-center and zone-boundary phonons with momentum $\mathbf{q}=\mathbf{K}$ can couple with electrons in the case of metallic CNTs (in this section, $\mathbf{q}$ will label the phonon momentum). This stems from the fact that phonon energies are much smaller than the electronic Fermi energy. Therefore, rather few phonon modes will be able to scatter electrons from one band to another. Further, depending on the relative signs of the Fermi velocity for the initial and final electronic states, the electron-phonon scattering processes are classified as "forward" or "backward," a notion that is crucial in transport theories. The different electron-phonon scattering processes (here a phonon emission) are summarized in Fig. 49.

We first start with a discussion of the EPC in the graphene sheet and reproduce in Fig. 50 the optical mode branches combining accurate experimental and *ab initio* calculations (Maultzsch *et al.*, 2005). At the zone center, the important modes for the EPC are the twofold E_g^2 high-energy in-plane modes which split away from Γ in a longitudinal and a transverse branch. At the zone boundary, the $\mathbf{q}=\mathbf{K}$ A_1' mode strongly couples to electrons. A clear manifestation of the EPC can already be

FIG. 50. (Color online) Inelastic x-ray scattering and *ab initio* calculations (open circles) of the phonon dispersion in graphite. Adapted from Maultzsch *et al.*, 2005.

found in the phonon band structures where a frequency softening can be observed. In the case of graphene, the peculiar shape of the graphene BZ induces a significant phonon softening of the E_g^2 and $\mathbf{K}$-A_1' modes, related to a Kohn anomaly, which manifests itself by a linear dispersion of the E_g^2 longitudinal and A_1' modes away from Γ and $\mathbf{K}$, respectively (Piscanec *et al.*, 2004).

In the D_{2nh} symmetry group of the achiral (n,n) or $(n,0)$ tubes (Damnjanović *et al.*, 1999; Reich *et al.*, 2004), the graphene Γ-E_g^2 degenerate mode splits into Γ-A_1 longitudinal (L) and transverse (T) polarization modes (labeled as well ILO or ITO for in-plane L or T optical modes). The Γ-A_1 modes EPC coupling in tubes was first shown to rationalize the redshift with decreasing radius of the Raman G band (Dubay *et al.*, 2002). In particular, the different evolution of the $A_1(L)$ mode for metallic and semiconducting zigzag tubes clearly pointed to an electronic contribution to the frequency softening. A clear illustration of the coupling is obtained by observing the evolution of the band structure upon distortion of the atomic network along the phonon eigenmodes with some amplitude $\delta d_{q\nu}$ (q and ν are the phonon momentum and band index). As shown in Fig. 51, the $A_1(L)$ phonon opens a gap at the Fermi level of metallic zigzag tubes, thus strongly affecting the electronic properties. As a matter of fact, the deformation potential $D_{nk}^{q\nu}$ (in eV/Å), which is a measure of the shift $\delta\varepsilon_{nk}$ of the band edges divided by $\delta d_{q\nu}$, can be related to the intraband EPC matrix elements $\langle\psi_{nk}|\delta V_{q\nu}|\psi_{nk}\rangle$, with $\delta V_{q\nu}$ the change upon lattice distortion of the potential seen by electrons (Khan and Allen, 1984) in the case of totally symmetric phonons.

The optical mode deformation potentials for (6,6) and (11,11) tubes have been determined with *ab initio* calculations by Lazzeri *et al.* (2005). They were compared, in particular, to the values obtained from a band-folding analysis of graphene Γ-E_g^2 and $\mathbf{K}$-A_1' deformation potentials ($D=6.7$ and 10.0 eV/Å, respectively), showing a $\sim$20% difference for the smaller tube ($\sim$8 Å diameter) as a manifestation of curvature effects. Similar values were obtained on the basis of a tight-binding approach for a (10,10) tube (Jiang *et al.*, 2005). However, the strong dependence of the deformation potential on the parametrization of the distance derivative of the hopping integral leads to rather scattered values (Mahan,

Acoustic phonon $q \sim 0, \hbar\Omega \ll k_B T$

Optical phonon $q \sim 0, \hbar\Omega > k_B T$

Zone boundary phonon $q > 0, \hbar\Omega > k_B T$
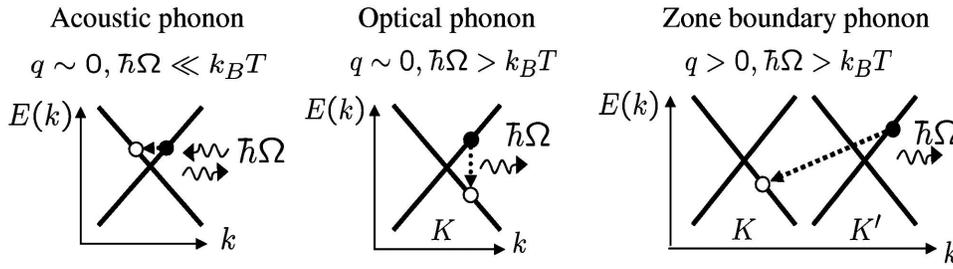
FIG. 52. Schematic representation of the main phonon contributions to backscattering (acoustic, optical, and zone-boundary modes).

2003; Park *et al.*, 2004; Jiang *et al.*, 2005; Perebeinos *et al.*, 2005; Popov and Lambin, 2006b).

The differences between graphene and tubes can be seen more clearly in the case of acoustic modes. The most documented example is that of the out-of-plane acoustic mode of graphene which becomes the radial breathing mode (RBM) in nanotubes. Since a change in the tube radius involves bond stretching and wagging, the RBM displays a nonzero frequency with a $1/R$ radius dependence exploited to calibrate tubes in Raman experiments (Rao *et al.*, 1997; Jorio *et al.*, 2001; Machón *et al.*, 2005; Meyer *et al.*, 2005; Popov and Lambin, 2006a). Further, evolution of the deformation potential and related EPC matrix elements was shown on the basis of *ab initio* calculations to strongly depend on the tube radius and helicity (Machón, 2005). In addition to the RBM, the acoustic in-plane transverse mode of the graphene sheet becomes the so-called twiston mode in tubes, which has been suggested to lead to a significant EPC coupling on the basis of tight-binding (Jishi *et al.*, 1993; Hertel and Moos, 2000; Mahan, 2003; Jiang *et al.*, 2005) or continuous elastic theories (Suzuura and Ando, 2002; De Martino and Egger, 2003).

An interesting issue is to distinguish the influence of confinement and curvature (namely, σ-π rehybridization) on the evolution with the diameter of the phonon frequency and EPC strength. In an early work (Benedict, Crespi, Louie, and Cohen, 1995), quite general symmetry arguments were developed to show that curvature would lead to a $1/R$ increase of the EPC matrix elements with decreasing radius R. This stems from the evolution from $pp\pi$ to $pp\sigma$ bonding upon increasing curvature, an effect that can be connected to the very large deformation potential at the origin of the superconducting transition in all-sp^3 (or σ-bonded) doped diamond (Blase *et al.*, 2004) and clathrates (Connétable *et al.*, 2003). In particular, modes such as the zone-center out-of-plane optical (ZO) and acoustic modes do not couple in the graphene sheet but show nonzero coupling in the case of tubes. Further, electronic and vibrational eigenstate normalization leads to a $1/\sqrt{R}$ dependence of the EPC matrix elements (Benedict, Crespi, Louie, and Cohen, 1995). This dependence will mainly affect modes that are already large in the planar graphene sheet (Γ-E_g^2 and $\mathbf{K}$-A_1').

A quite general analysis of the evolution of the EPC matrix elements with radius, chiral angle, and tube type (metallic types I and II or semiconducting) has been developed on the basis of tight-binding analysis, allowing

for analytic formulas at high-symmetry points (Mahan, 2003; Jiang *et al.*, 2005; Popov and Lambin, 2006b). Such matrix elements were used to compare the experimental and calculated PL and resonant Raman scattering intensities (Jorio *et al.*, 2006). The importance of accurately evaluating EPC matrix elements has also been emphasized recently in attempting to identify the origin and nature of the so-called high-energy G^+ and G^- bands (Lazzeri *et al.*, 2006; Popov and Lambin, 2006a). Such an identification is closely related to the above-mentioned Kohn anomaly, leading to significant mode softening in the limit of small radii.

2. Inelastic transport length scales

We now extend our discussion of the electron-phonon coupling to its influence on transport in the normal state (in contrast to the superconducting phase treated in Sec. IV.F). Electronic transport is sensitive to inelastic effects stemming from either *e*-ph or *e*-*e* scattering. An investigation of the temperature dependence of conductance provides a wealth of information about decoherence mechanisms and inelastic scattering rates. Low-bias measurements show that $G \sim \alpha/T$ (Yao *et al.*, 2000), a scaling law that has been related to *e*-ph scattering driven by low-energy vibrational modes. By using a phenomenological relationship between the conductance and the scattering rate,

$$G \sim \frac{2e^2}{h} \frac{\ell_{ie}}{L_{\text{tube}}}, \tag{57}$$

a typical scattering length $\ell_{ie} \sim 1$–2 μm (300 K) was inferred and attributed to *e*-ph coupling involving acoustic modes. On the other hand, the inelastic scattering rates can be theoretically computed by means of the FGR derived from either a first-principles (Lazzeri *et al.*, 2005) or a semiempirical approach (Jiang *et al.*, 2005). The FGR consists here in calculating the scattering rate between eigenstates of the zero-phonon Hamiltonian. This assumes that the phonon and electronic populations are at equilibrium and can be treated independently, the *e*-ph coupling being assumed to remain of a perturbative nature. In that framework, the inelastic scattering length associated with a given phonon mode is readily deduced from $\ell_{ie} = v\tau_{ie}$, with v the relevant average velocity of the charge carrier energy. Three important phonon modes yield contributions to inelastic backscattering. As depicted in Fig. 52, the first process is driven by acoustic phonons with low energy and small momentum. Within

the FGR, the scattering rate (with phonon emission) $\tau_{e\text{-ph}}^{-1}(\mathbf{q})$ is written as

$$\frac{2\pi}{\Omega\hbar}\sum_k |\langle \mathbf{k}+\mathbf{q},n_q+1|\hat{\Gamma}_{e\text{-ph}}|\mathbf{k},n_q\rangle|^2 \delta(\varepsilon_{k-q}-\varepsilon_k-\hbar\omega_q)$$

$$\times(1+n_q)[1-f(\varepsilon_{k-q})]f(\varepsilon_k), \tag{58}$$

with Ω the surface of the tube and $\hat{\Gamma}_{e\text{-ph}}$ the electron-phonon scattering operator, while n_q and $f(\varepsilon_k)$ give the phonon and electron distributions, respectively. In metallic tubes, the acoustic torsional mode (twisting mode or twiston) is a purely circumference-directional deformation, while its velocity is equal to a transverse acoustic mode of the graphene sheet $[\omega(\mathbf{q})=v_{\text{twist}}|\mathbf{q}|]$. A crude estimation due to inelastic scattering gives $\tau_{e\text{-ph}}^{-1} \sim (4\pi/\hbar)D^2(k_BT/2\rho_M v_{\text{twist}}^2)/hv_F$, with ρ_M the mass density and D the deformation potential (Park *et al.*, 2004). It has to be noted that, unlike in ordinary metals, the linear temperature dependence of the electronic resistivity persists well below the Debye temperature, essentially because these phonon modes are heavily thermally populated (Kane *et al.*, 1998). With reasonable parameters, the inelastic acoustic scattering time is found to be $\simeq 3\times10^{-12}$ s, with a subsequent inelastic mean free path $\ell_{e\text{-ph}}=v_F\tau_{e\text{-ph}}\simeq 2.4$ μm for a 1.8-nm nanotube (Yang and Han, 2000; Park *et al.*, 2004). A theoretical derivation has also predicted some helical-dependent contribution to electron-phonon backscattering and the resistance value in the high-temperature regime (Suzuura and Ando, 2002).

In the high-bias regime, experiments have reported on a $G_{\text{tube}}\sim\beta/V$ scaling law, a behavior attributed to an electronic coupling to zone-center optical as well as zone-boundary phonon modes. By using the same phenomenological relationship $G\sim(2e^2/h)\ell_{ie}/L_{\text{tube}}$, Park and co-workers (Park *et al.*, 2004) experimentally estimated the inelastic mean free paths ℓ_{ie} in the high-bias regime. For bias voltage of the order of 1 V, $\ell_{ie} \sim 10$ nm was assigned to a contribution to both optical and zone-boundary modes. Within the framework of the effective mass formula and deformation potential approximation, the theoretical electron–acoustic-phonon scattering length was estimated to be $\simeq 2.4$ μm in the low-bias regime, while optical and zone-boundary modes were associated with ℓ_{ie} of the order of 180 and 37 nm, respectively. By applying Matthiessen's rule, the total inelastic length at high bias was deduced to be of the order of 30 nm.

In a different approach, Javey and co-workers (Javey *et al.*, 2004) used a CNT-FET experiment, and by fitting with semiclassical Monte Carlo models, they estimate $\ell_{ie}=300$ nm for acoustic modes and $\ell_{ie}=15$ nm for optical modes.

Thus, the reported values for inelastic mean free paths strongly fluctuate within the range [10 nm, 200 nm] for the case of electron–(optical-)phonon coupling. Further, a comparison of experimental values with FGR calculations from first principles leads to a disagreement of about one order of magnitude (Lazzeri *et al.*, 2005).

Perebeinos, Tersoff, and Avouris (2005) recently proposed to investigate the effect of inelastic scattering on the conductance by following the semiclassical Bloch-Boltzmann treatment of transport theory. The authors derive a phenomenological law for the zero-field charge-carrier mobility $\mu(T,d_{\text{tube}})=\tilde{\mu}[(300\text{ K})/T][d_{\text{tube}}/(1\text{ nm})]^\alpha$, exhibiting some specific temperature and diameter dependences (here $\tilde{\mu}=12\,000$ cm^2/V s and $\alpha \sim 2.25$).

In contrast, other theoretical works have investigated the influence of structural lattice fluctuations on the electronic band structure (Dubay *et al.*, 2002) and transport (Georghe *et al.*, 2005; Roche *et al.*, 2005b). The superimposed contribution of optical phonon vibrations has yielded time-dependent band structure changes which affect the conductance scaling features (Roche *et al.*, 2005b). A more general quantum treatment of inelastic transport in metallic nanotubes, going beyond the linear response and within a true many-body approach, has revealed the occurrence of a Peierls-like mechanism associated with the longitudinal optical mode activation (Foa-Torres and Roche, 2006). These recent results highlight effects which are beyond the scope of semiclassical transport theories. Their impact on the simulation of carbon-nanotube–based field-effect transistors remains an open issue.

3. Electron-electron scattering and Luttinger-liquid models

The contribution of *e*-*e* interactions can be envisioned from two perspectives. In the first case, high dimensionality and screening effects are sufficient to warrant that Coulomb interactions can be treated perturbatively, while charge transport remains well described within the Fermi-liquid picture. The stability of the Fermi liquid is actually well established for 3D systems, owing to the fact that the Pauli exclusion principle strongly quenches the electron-electron interaction (Nozières and Pines, 1999). At zero temperature, the discontinuity of the Fermi-Dirac distribution at E_F, combined with the conservation of energy and momentum, causes the number of final (empty) available states to which an electron of energy $E \lesssim E_F$ can be scattered to go quadratically to zero as a function of $E-E_F$. This is the famous result that the lifetime $\tau^{e\text{-}e}$ of an electron, with respect to electron-electron interactions, scales as $1/(E-E_F)^2$ close to the Fermi level.

Such a Fermi-liquid description has been extensively employed for describing quantum transport in MWNTs with large diameters, given the reported strong evidence of weak localization (Bachtold *et al.*, 1999; Stojetz *et al.*, 2005). At low temperatures, the *e*-*e* interaction then acts as a source of decoherence in the weak-localization regime, limiting the contribution of quantum interference and localization effects. Similarly, screening by a metallic substrate, or a surrounding gate, seems to be at the origin of good agreement between the measured STM density of states in small-diameter SWNTs and tight-binding calculations performed assuming noninteracting states (see Sec. III.D). At higher temperature, *e*-*e* scattering
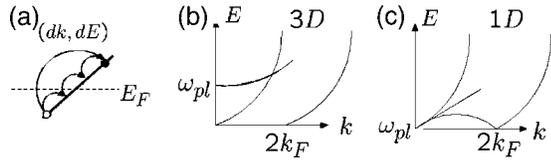
FIG. 53. Elementary excitations in 1D systems. (a) Symbolic representations of a linear band around k_F. The decay of a single-electron excitation into $n=3$ subprocesses is represented. (b), (c) Single-particle and plasmon (energy, momentum) diagrams in 3D and 1D systems. Note that long-wavelength single-particle excitation and plasmon ω_{pl} energies are decoupled in 3D but resonant in 1D.

can drive the temperature dependence of transport coefficients. For instance, Balents and Fisher (1997) demonstrated that umklapp scattering due to e-e interactions yields a resistance linear in temperature. Within this regime, the transport physics is still generally well described within the standard Fermi-liquid single-particle picture, where by starting from extended wave functions with wave vector k the interactions appear as scattering processes between states with different k values, the relevant events being forward and backward scattering with energies close to the Fermi surface.

On the other hand, carbon nanotubes also provide new opportunities to search for strong deviations from the Fermi-liquid theory, since, especially in the case of small-diameter SWNTs, their low dimensionality considerably enhances the strength of repulsive Coulomb interactions. As a matter of fact, independent of the range and strength of the interaction between electrons, it can be shown that scattering of a single charge carrier induces a "collective" response of the 1D electron gas. From that standpoint, the concept of single-particle scattering seems useless and one should adopt a description where all electrons are collectively modified by an external pump or probe. Collective electronic excitations can be described in terms of the well-known charge and spin waves (plasmons and spinons). This point can be illustrated by observing that, sufficiently close to the Fermi level, an electronic band can always be linearized around k_F: $E(k)=v_F(k-k_F)$, with v_F the Fermi velocity [Fig. 53(a)]. The excitation energy associated with an intraband scattering can then be linearly related to the variation of momentum through $dE=v_F dk$. Clearly, conservation of momentum and energy is preserved if one replaces the (dk,dE) single excitation by n $(dk/p,dE/p)$ processes involving p electrons. Namely, there is a momentum and energy resonance between single-electron

scatterings and excitations involving an arbitrarily large number of particles. One says that single-particle excitations decay into collective plasmon modes [Fig. 53(c)].

To describe the charge and spin collective excitations in 1D systems in the presence of a strong Coulomb interaction, a heuristic approach is used based on the Wannier representation. In the Wannier picture, the many-electron Hamiltonian, represented in terms of wave functions localized around the site m $=1,2,3,\ldots,N$ of the lattice, is a Hubbard type where the dominant interaction is between electrons at the same site. The (bare) Coulomb interaction is, however, of long-range nature, so the simple Hubbard model will represent only physical situations for which e-e interactions are strongly screened. By considering an extended version of the on-site Hubbard model (retaining e-e interactions between nearest neighbors), one can enlarge the range of the Coulomb potential to nearest-neighbor sites. The Wannier version of the Hamiltonian is then written as (Baeriswyl and Degiorgi, 1990)

$$H = H_0 + H_{\text{int}} = -\gamma_0 \sum_{m\sigma} (c^\dagger_{m\sigma} c_{m+1\sigma} + c^\dagger_{m+1\sigma} c_{m\sigma})$$
$$+ \tilde{U}_0 \sum_m n_{m\uparrow} n_{m\downarrow} + \tilde{V}_0 \sum_m n_m n_{m+1}, \quad (59)$$

where $c^\dagger_{m\sigma}$ ($c_{m\sigma}$) creates (annihilates) an electron at site m with spin projection $\sigma=\uparrow,\downarrow$, $n_{m\sigma}=c^\dagger_{m\sigma}c_{m\sigma}$, and n_m $=n_{m\uparrow}+n_{m\downarrow}$. For a half-filled band (one electron per site), the $\tilde{U}_0$ term favors an alternating charge density. If one now imposes periodic boundary conditions, i.e., $c_{N+1\sigma}$ $=c_{1\sigma}$, the Bloch representation can be introduced through the canonical transformation $c_{m\sigma}$ $=(1/\sqrt{N})\Sigma_k e^{ikm} c_{k\sigma}$, with $k=2\pi\nu/N$ and $-N/2 \leqslant \nu \leqslant N/2$, i.e., k can be chosen to lie in the first Brillouin zone $-\pi \leqslant k \leqslant \pi$. This transformation diagonalizes the first term of the Hamiltonian as $H_0=\Sigma_k \varepsilon_k c^\dagger_{k\sigma} c_{k\sigma}$ (kinetic energy), with $\varepsilon_k=-2\gamma_0 \cos k$. If one is restricted to the linear part of the spectrum and defines $\Psi_{+,k\sigma}=c_{k_F+k,\sigma}$ and $\Psi_{-,k\sigma}=c_{-k_F+k,\sigma}$, which is just a gauge transformation, we obtain

$$H_0 = \sum_{k\sigma} \hbar v_F k (\Psi^\dagger_{+,k\sigma} \Psi_{+,k\sigma} - \Psi^\dagger_{-,k\sigma} \Psi_{-,k\sigma}), \quad (60)$$

the $\Psi_{+,k\sigma}$ and $\Psi_{-,k\sigma}$ operators representing the right- and left-moving states with wave vectors $+k_F$ and $-k_F$, respectively. These states were introduced by Luttinger (1963). Rewriting H_{int} in terms of these new operators one gets

$$H_{\text{int}} = \frac{1}{N} \sum_{k_1,k_2,k_3,k_4,\sigma,\sigma'} \delta_{k_1+k_2,k_3+k_4} \left(g_1 \Psi^\dagger_{+,k_1\sigma} \Psi^\dagger_{-,k_2\sigma'} \Psi_{+,k_3\sigma'} \Psi_{-,k_4\sigma} + g_2 \Psi^\dagger_{+,k_1\sigma} \Psi^\dagger_{-,k_2\sigma'} \Psi_{-,k_3\sigma'} \Psi_{+,k_4\sigma} \right.$$
$$\left. + \frac{g_3}{2} (\Psi^\dagger_{+,k_1\sigma} \Psi^\dagger_{+,k_2\sigma'} \Psi_{-,k_3\sigma'} \Psi_{-,k_4\sigma} + \text{H.c.}) + \frac{g_4}{2} (\Psi^\dagger_{+,k_1\sigma} \Psi^\dagger_{+,k_2\sigma'} \Psi_{+,k_3\sigma'} \Psi_{+,k_4\sigma} + \Psi^\dagger_{-,k_1\sigma} \Psi^\dagger_{-,k_2\sigma'} \Psi_{-,k_3\sigma'} \Psi_{-,k_4\sigma}) \right), \quad (61)$$

where terms that can be incorporated within the chemical potential have been neglected. The coupling constants g_i are related to the Hubbard parameters as follows: $g_1 = g_3 = \tilde{U}_0 - 2\tilde{V}_0$ and $g_2 = g_4 = \tilde{U}_0 + 2\tilde{V}_0$. All scattering processes in H_{int} can be pictorially represented by Feynman diagrams. The first process g_1 corresponds to backward scattering, while the process g_2 is a forward-scattering event, and g_3 arises as an umklapp process, which becomes irrelevant far from half-filling. Finally g_4 leads to a small renormalization of the Fermi velocity, which is usually neglected. The whole Hamiltonian $H_0 + H_{int}$ defines the one-dimensional Fermi gas model (Solyom, 1979). A simple solvable case of the one-dimensional Fermi gas model is the Tomonaga-Luttinger model (Tomonaga, 1950; Luttinger, 1963), where only forward scattering (g_2) is taken into account ($g_1 = g_3 = g_4 = 0$). It has been solved by Mattis and Lieb (1965), who showed that this model describes a particular type of system where the conventional Fermi surface, defined in terms of a step in the momentum distribution, does not exist for arbitrarily small $g_2 = g$. Haldane (1981) later extended their analysis to a more general situation and coined the term "Luttinger liquid" (LL) in analogy with the Fermi liquid. If for simplicity one is restricted to the the case of spinless fermions, the LL Hamiltonian is written

$$H = H_0 + H_{int} = \sum_{k\sigma} \hbar v_F k (\Psi^\dagger_{+,k\sigma}\Psi_{+,k\sigma} - \Psi^\dagger_{-,k\sigma}\Psi_{-,k\sigma})$$
$$+ \frac{1}{N}\sum_q g(q)\rho_1(q)\rho_2(q), \tag{62}$$

with $\rho_1(q) = \Sigma_k \Psi^\dagger_{+,k}\Psi_{+,k+q}$ while $\rho_2(q) = \Sigma_k \Psi^\dagger_{-,k}\Psi_{-,k+q}$. In the ground state of H_0, all negative-energy states are occupied, while all positive-energy states remain empty. The density operators $\rho_i(q)$ act like Bose creation and annihilation operators of elementary excitations with energy $\hbar v_F|q|$ and momentum q (the so-called bosonization scheme). Several important quantities can be exactly calculated for the LL model, including the momentum distribution function (Mattis and Lieb, 1965) and various response functions (Solyom, 1979), which generally exhibit power-law behavior (Voit, 1995; Giamarchi, 2004).

Despite the early predictions of the LL transition, the difficulty in performing low-temperature experiments on isolated 1D systems explains why experimental confirmation of LL behavior has remained scarce. In that respect, synthesis of CNTs has provided a unique playground to test the theoretical concepts. A formal description of the LL in armchair metallic SWNTs was proposed (Egger and Gogolin, 1997, 1998; Kane et al., 1997). In regard to the strict single-channel case, carbon nanotubes display more complex quasi-1D characteristics, which are required to reconsider (and extend) the basics of LL theory. First, the Fermi surface is described by four k_F points of the Brillouin zone, instead of the two k_F points found for a single channel. In addition, depending on the CNT diameter and chirality, the den-

sity of states varies for small Fermi level shifts, which complicates the extension of analytical results obtained for a 1D channel with constant DOS. In particular, at each onset of new subbands, large fluctuations of the DOS ($\sim 1/\sqrt{E}$) make the LL description technically inappropriate (Giamarchi, 2004). Finally, in real experiments, the structural quality of CNTs as well as the efficiency of electronic contact with external voltage probes are often insufficiently high, all factors that may also limit the applicability range of the LL model in CNTs.

Notwithstanding, whenever the CNT/electrode interface is dominated by a weak tunneling contact and as long as one is restricted to low-energy transport properties, extensions of the LL model to account for additional complexities such as elastic scatterers, intershell tunneling, and multichannel degeneracy have been developed (Egger and Gogolin, 1997, 1998; Kane et al., 1997; Egger, 1999; Mora et al., 2006).

For the sake of illustration, we derive the main LL properties in CNTs, restricting ourselves for simplicity to the spinless electron case (following Mora et al., 2006). We define x as the coordinate along the CNT axis, while $\mathbf{r}_\perp$ denotes the coordinate in the perpendicular direction, so that the wave functions can be expanded as follows ($n = 1, 2$ for the channel degeneracy):

$$\Psi_\pm = \sum_{n=1}^2 e^{\pm k_n x}\phi_n(\mathbf{r}_\perp)\psi_{n,\pm}(x), \tag{63}$$

where $\phi_n(\mathbf{r}_\perp)$ are the transverse eigenmodes normalized according to $\int d\mathbf{r}_\perp \phi_n^*(\mathbf{r}_\perp)\phi_n(\mathbf{r}_\perp) = \delta_{mn}$. Explicitly, $\phi_n(\mathbf{r}_\perp) = |\mathbf{C}_h|^{-1/2}\exp(2\pi i n y/|\mathbf{C}_h|)$, with $|\mathbf{C}_h| = 2\pi r_{tube}$, while y is an angular variable. Each one of the two channels will intersect the Fermi surface at $k = \pm k_n$, with its own Fermi momentum k_n and Fermi velocity v_n. The kinetic part of the Hamiltonian at low energy is rewritten as (Egger and Gogolin, 1997)

$$H_0 = -iv_F\int dx[\Psi^\dagger_+(x)\partial_x\Psi_+(x) - \Psi^\dagger_-(x)\partial_x\Psi_-(x)], \tag{64}$$

with the noninteracting DOS given by $\nu = 2/\pi v_F$. The exact repulsive Coulomb interaction $U_{Coulomb}$ among electrons can be described by the extended Hubbard-Wannier model as previously described. Recently López-Sancho and co-workers (López-Sancho et al., 2001) established, within the mean-field unrestricted Hartree-Fock approximation, a phase diagram ($\tilde{U}_0, \tilde{V}_0$) for the spectrum modifications of metallic armchair and zigzag nanotubes. They found that a true metallic phase persists if on-site and nearest-neighbor interaction parameters are such that $\tilde{U}_0 \leq 2\gamma_0, \tilde{V} \leq \gamma_0$, whereas charge or spin density wave phases develop for larger values, along with small gap openings.

However, from a more general perspective, the e-e interaction term should include the screened long-range part of the potential, which can only be estimated in some approximations. For low-energy properties, following Mora and co-workers (Mora et al., 2006), the interaction is taken as long ranged on length scales larger

than $|\mathbf{C}_h|$, so that the long-range tail of the interaction dominates all 1D Coulomb matrix elements, giving

$$U_{mn} = \int d\mathbf{r}_\perp d\mathbf{r}'_\perp U_{\text{Coulomb}}(x - x', \mathbf{r}_\perp, \mathbf{r}'_\perp)$$
$$\times |\phi_n(\mathbf{r}_\perp)|^2 |\phi_m(\mathbf{r}'_\perp)|^2. \tag{65}$$

For $|x - x'| \gg |\mathcal{C}_h|$, U_{Coulomb} becomes nearly independent of the transverse coordinates and the projected interaction is independent of the channel indices $U_{mn} = U(x - x')$. By expanding the wave functions, the resulting interaction term for the LL (keeping only forward scattering) reads

$$\frac{1}{2} \sum_{+,-} \sum_{n,m=1,2} \int dx\, dx'\, U(x-x') \Psi^\dagger_{n,+}(x) \Psi^\dagger_{m,-}(x')$$
$$\times \Psi_{m,-}(x') \Psi_{n,+}(x), \tag{66}$$

which reduces to $\frac{1}{2} \int dx\, dx' \rho(x) U(x-x') \rho(x')$, indicating that the interaction induces effective coupling between 1D charge density fluctuations. In the long-wavelength limit, one can approximate the Fourier transform $U(k)$ by a constant $U_0 = U(0) - U(2k_F)$ (which will set the interaction strength), to end with a final expression for the interaction term as $H_I = (U_0/2\kappa) \int dx\, \rho^2(x)$, with κ the relevant dielectric constant. In real situations, the Coulomb interaction can be externally screened on a scale L_{scr}, which remains long compared to the CNT radius but shorter than the CNT length. This would occur by assuming a surrounding cylinder of radius L_{scr} placed around the tube. In this case, from elementary electrostatics, the energy to charge the nanotube with an electron density $e\rho_{\text{tot}}$ will be $(e^2/\kappa)\ln(L_{\text{scr}}/r_{\text{tube}}) \int dx\, \rho^2_{\text{tot}}$.

For this LL model in the metallic armchair tube, a single interaction parameter g will drive the power-law temperature-dependent (for $eV \ll k_B T$) and voltage-dependent (for $eV \gg k_B T$) tunneling conductances. The density of states for an electron tunneling from the metallic electrode into the nanotube is $\rho_{\text{tun}}(E) \sim E^{\alpha_b}$ with an exponent $\alpha_b = (g + g^{-1} - 2)/8$, provided electrons tunnel from the metallic (Fermi-liquid) contact into the center of the nanotube (referred to as the bulk contact). Accordingly, the low-temperature conductance $dI/dV = G \simeq V^{\alpha_b}$, while the linear conductance becomes $G(T) \simeq T^{\alpha_b}$. The conductance suppression at low temperature or bias has been shown to become even more dramatic for tunneling into the end of a long nanotube, with an exponent that now reads $\alpha_e = (g^{-1} - 1)/4$ (Egger and Gogolin, 1997). On the other hand, the generic form of the Luttinger parameter is $g = (1 + 2U_0/\Delta)^{-1/2}$ with U_0 the charging energy, whereas Δ is the single-particle level spacing. If Δ is unequivocally given by $\hbar v_F/2L_{\text{tube}}$, the charging energy follows from the capacitive properties of the metal-nanotube junction and from the electronic structure, so that no universal value can be derived. In the weak-screening limit, the tube length becomes the physical cutoff of the e-e interactions, i.e., $L_{\text{scr}} \sim L_{\text{tube}}$

(Kane *et al.*, 1997, Egger and Gogolin, 1998), which allows a phenomenological form of the interaction parameter:

$$g = \left(1 + \frac{8e^2}{\pi \kappa \hbar v_F} \ln \frac{L_{\text{tube}}}{r_{\text{tube}}}\right)^{-1/2}. \tag{67}$$

Taking as a typical value $L_{\text{tube}}/r_{\text{tube}} \sim 10^3$, the theoretical interaction parameter for a metallic armchair nanotube becomes $g \simeq 0.28$. Subsequently, the bulk-tunneling and end-tunneling exponents are, respectively, given by $\alpha_b \simeq 0.24$ and $\alpha_e \simeq 0.65$ (Egger and Gogolin, 1997; Kane *et al.*, 1997). More generally, the differential conductance for a single tunnel junction is given by a universal scaling curve

$$\frac{dI}{dV} = A T^{\alpha_{b,e}} \cosh\left(\gamma \frac{eV}{2k_B T}\right) \left| \Gamma\left(\frac{1 + \alpha_{b,e}}{2}\right.\right.$$
$$\left.\left. + \gamma \frac{ieV}{2\pi k_B T}\right) \right|^2, \tag{68}$$

which means that $(dI/dV)/T^{\alpha_{b,e}}$ is a universal function of $eV/k_B T$ and $\Gamma(x)$ is the Gamma function.

The non-Ohmic behavior of the conductance at low bias voltage is often referred to as the zero-bias anomaly (ZBA) and is a clear signature of a tunneling contact between a Fermi liquid and a strongly correlated system. Some experiments have reported on power-law conductance behaviors with exponent values in the range of theoretical predictions either for individual single-walled nanotubes (Bockrath *et al.*, 1999; Yao *et al.*, 1999) or for crossed metallic junctions of SWNTs (Gao *et al.*, 2004), giving confidence in the manifestation of a Luttinger-liquid state in small-diameter SWNTs. Alternatively, by means of angle-integrated photoemission measurements of SWNTs, some power-law behavior of the spectral function and intensities was also found to be in good agreement with LL model predictions (Ishii *et al.*, 2003).

Similarly, STM experiments on SWNTs have provided some possible alternative signatures for the non-Fermi-liquid properties of metallic nanotubes (Lee *et al.*, 2004). In this work, the tunneling properties of electrons from a metallic tip to a metallic tube deposited on a gold substrate were analyzed in terms of e-e interaction-induced charge-spin separation. The strength of the Coulomb interaction inside the nanotube was, however, found to be reduced from its expected theoretical value (Eggert, 2000), possibly due to the screening effect of the underlying metallic substrate. This is illustrated in Fig. 54, where a tight-binding calculation shows the two standing waves with different wavelengths caused by separate spin and charge bosonic excitations. The slopes calculated near the K points, ± 8.8 and ± 11.9 cm^{-1}, correspond to a larger charge-mode group velocity of $\sim v_F/0.55$, whereas the spin-mode velocity remains similar to the Fermi velocity v_F obtained for noninteracting electrons. The deduced value for the g parameter is ~ 0.55, much larger than the predicted value given by the unscreened Coulomb potential, $g \sim 0.3$ (Kane *et al.*, 1997). This indicates a possible screening of e-e interac-
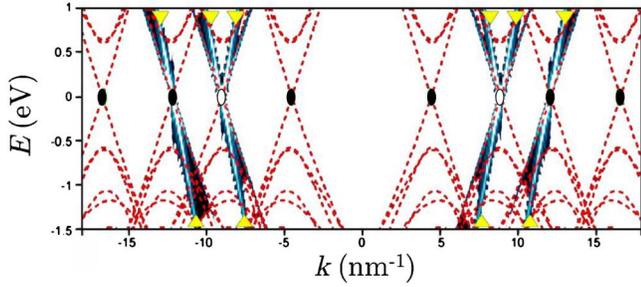
FIG. 54. (Color online) Fourier-transformed map of dI/dV (density of states) as a function of electron momentum k and sample bias V. Ovals near the Fermi levels indicate the corners of the Brillouin zone nearest (elongated black dots) or second nearest (elongated white dots) to the Γ point. Curves give the energy dispersions of the (19,7) tube by tight binding, whereas superimposed color lines indicate the Luttinger-liquid result. Adapted from Eggert, 2000.

tions, induced by the metallic substrate, which can be substantiated by replacing L_{tube} by a screened length in Eq. (67). A straightforward evaluation yields $\sim 1.4 r_{tube}$ to fit the experimental data (Lee *et al.*, 2004).

In the case of MWNTs composed of N metallic armchair shells, intershell coupling has been predicted to induce additional screening of the Coulomb interaction, screening that can be recast by renormalizing the power-law exponents by a factor of $1/N$ (for both cases α_b/N and α_e/N). This produces an increase of g which tends to 1 in the limit $N \to \infty$ (Fermi-gas limit) (Egger, 1999). One also notes that, in the case of a tunneling contact to MWNTs, the observed zero-bias anomaly and power-law behaviors of transport quantities have been assigned to a different physical mechanism known as the environmental Coulomb blockade, which can, like the LL model, describe the same kind of universalities in the conductance scaling anomalies (Rollbühler and Grabert, 2001; Tarkiainen *et al.*, 2001; Dayen *et al.*, 2005). Further, several groups (Egger and Gogolin, 2001; Mishchenko *et al.*, 2001; Mishchenko and Andreev, 2002) have performed a nonperturbative calculation of the *e-e* interaction in disordered MWNTs, showing a crossover from the Luttinger-liquid result (valid at sufficiently high energy) to a new low-energy behavior of the density of states.

We end by discussing the case of graphite, which we have often used to illuminate the properties of CNTs through band-folding arguments. Several theoretical (González *et al.*, 1996; Spataru *et al.*, 2001) and experimental (Xu *et al.*, 1996; Moos *et al.*, 2001) studies have revealed an anomalous $(E-E_F)$ linear behavior of the inverse $1/\tau^{ee}$ lifetime, deviating from the standard Fermi-liquid theory. However, such effects stem from the specific band structure of graphite and cannot be used for laying the grounds for a LL transition in nanotubes.

4. Transport spectroscopy in the Coulomb blockade regime

In the situation of high contact resistance between metallic or semiconducting CNTs and voltage probes,
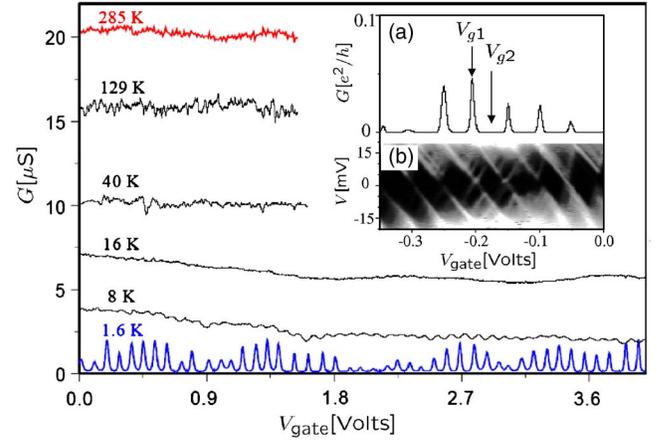
FIG. 55. (Color online) Conductance spectrum for several temperatures as a function of external gate voltage applied to the single-walled nanotube contacted with noble metal. Inset: $G(V_g)$ for a device at 4.2 K showing a regular series of Coulomb conductance peaks. Adapted from Nygard *et al.*, 1999.

the low-temperature transport properties turn out to be dominated by the Coulomb-blockade effect. This phenomenon, first observed in semiconductor quantum dots and small metallic grains (Grabert and Devoret, 1992), occurs at low enough temperature, when the total capacitance C of a metallic island becomes so small that adding even a single electron requires an electrostatic energy $E_c = e^2/2C$ larger than the thermal energy $k_B T$. This situation generally develops when the conducting island is weakly coupled to source and drain leads through tunnel barriers with a resistance larger than the quantum resistance h/e^2.

As a matter of illustration, if one considers a nanotube at a distance z away from a conducting substrate (metallic gate), the total capacitance is $C = 2\pi \kappa_r \epsilon_0 L_{tube}/\ln(2z/r_{tube})$, κ_r being the average dielectric constant of the environment. Using $\epsilon_r \simeq 2$ (for comparison, $\kappa_r = 3.9$ for SiO$_2$), $z = 300$ nm, and $r_{tube} = 0.7$ nm, the charging energy becomes $E_c \simeq (5 \text{ meV})/[L_{tube} (\mu m)]$. Thus for a typical ~ 1 μm long tube, Coulomb blockade should set in below $\simeq 50$ K ($k_B T = 5$ meV). For small electrode spacing, the total capacitance is often dominated by the capacitance of the leads.

Level splitting due to the finite size of the nanotube is another relevant energy scale. A simple particle-in-a-box estimate yields $\Delta E = h v_F/4 L_{tube} \simeq (1 \text{ meV})/[L_{tube} (\mu m)]$; the factor of 2 accounts for the channel degeneracy at the charge-neutrality point. Both E_c and ΔE scale inversely with length (up to a logarithmic factor), but the ratio $E_c/\Delta E$ is thus roughly independent of length, i.e., the level spacing is always a small but appreciable fraction of the charging energy.

In Fig. 55 (main frame), the experimental conductance dI/dV at small bias and as a function of gate voltage is shown for various temperatures for a single-walled carbon nanotube. When $k_B T < E_c$, single-electron tunneling prevails as revealed by the fine structure of the conductance spectrum. Each conductance peak represents the

addition of an extra charge to the nanotube, whereas the peak spacing is given by $(2E_c + \Delta E)C/eC_g$, with C_g and C the capacitance of the gate and the total capacitance, respectively. The regularity (periodicity) of the peaks is related to the size of the coherent conducting island (nanotube). In the case of an irregular conductance spectrum, the nanotube is believed to be split into a series of conducting parts separated by local tunneling contacts.

The overall diagram of conductance as a function of bias and gate voltage generally appears as a diamond-shaped structure [Fig. 55, inset (b)], referred to as the Coulomb diagram. For a fixed gate voltage, the current increases stepwise with increasing bias voltage, producing the excited-state spectrum. Each step in the current is related to a new higher-lying energy level that enters the bias window [Fig. 55, inset (a), V_{g1}]. Within each diamond, the electron number of the nanotube is fixed and the current vanishes [Fig. 55, inset (a), V_{g2}]. The boundary of each diamond represents the transition between N and $N+1$ electrons, and the parallel lines outside the diamonds correspond to excited states. Such a plot is well understood within the constant-interaction model, in which the capacitance is independent of the electronic states. Some significant deviations from this simple picture were, however, observed (Tans *et al.*, 1998). The ground-state spin configuration in a nanotube was determined by studying the transport spectrum in a magnetic field. Cobden and co-workers (Cobden *et al.*, 1998) observed that the level spectrum is split by the Zeeman energy $g\mu_B B$, where μ_B is the Bohr magneton and the g factor is found to be 2, indicating the absence of orbital effects as expected for nanotubes; the total spin of the ground state alternates between 0 and $1/2$ as successive electrons are added, demonstrating a simple shell-filling, or even-odd, effect, i.e., successive electrons occupy the levels in spin-up and spin-down pairs. The semiconducting case was treated by Jarillo-Herrero *et al.* (2004). Some value of the orbital magnetic moment could also be estimated using the magnetic field effect to lift the orbital degeneracy (Jarillo-Herrero *et al.*, 2005).

Finally, in the Coulomb-blockade regime, transport measurements on suspended single-wall carbon nanotubes have shown spectacular signatures of phonon-assisted tunneling, mediated by longitudinal vibrational (stretching) modes (Sapmaz *et al.*, 2006). In this experiment, the current-voltage characteristics show multiple steps whose heights are in reasonable agreement with the Franck-Condon predictions of a large *e*-ph coupling constant. On the other hand, in this regime, Coskun and co-workers (Coskun *et al.*, 2004) succeeded in measuring Aharonov-Bohm ϕ_0 periodic oscillations of the band structure for a MWNT.

On the theoretical side, a calculation of the total transmission coefficient, based on expanding the many-body wave function into all possible single-particle wave functions, was shown to provide a good description of Coulomb blockade in CNTs (Mehrez *et al.*, 2001). Further, Bellucci and co-workers (Bellucci *et al.*, 2005) studied the crossover from a Luttinger liquid to the Coulomb-blockade regime in CNTs. They extended the LL description by incorporating the effects of a single-particle spectrum and found that the intermediate regime is characterized by a power-law conductance, with power exponent oscillating with applied gate voltage. This scheme tends to support similar experimental measurements obtained in MWNTs (Kanda *et al.*, 2005).

F. Superconducting and charge-density-wave instabilities

The field of superconductivity (SC) in nanotubes started experimentally in 1998 with the discovery of a strong proximity-induced SC in isolated or bundled SWNTs connected to superconducting leads (Kasumov *et al.*, 1998; Mopurgo *et al.*, 1998). In these experiments, the NTs were considered to be in the normal (N) state but with a phase coherence length L_ϕ and a thermal length L_T larger than the superconducting coherence length, allowing for the SNS junction to sustain a very high supercurrent below the lead transition temperature. Three years later, however, intrinsic SC in nanotubes was discovered in bundles of large-diameter SWNTs (Kociak *et al.*, 2001; Kasumov *et al.*, 2003) and in zeolite-inserted SWNTs of small (~4 Å) diameter (Tang *et al.*, 2001). While in the first case a $T_C = 0.55$ K was observed on the basis of resistivity measurements, the small-diameter SWNT samples led to $T_C \sim 15$ K, as evidenced from the Meissner effect. These early observations were confirmed with the observation of a SC transition with T_C up to 12 K in MWNTs encapsulated in large pores of zeolite (Takesue *et al.*, 2006).

Before continuing, it is important to comment on the low-energy excitation phase diagram of 1D systems in general, complementing our discussion of the Luttinger liquid (Sec. IV.E.3) by switching on the electron-phonon interaction. Upon coupling of both electrons and phonons, the superconducting phase in 1D systems enters into competition with another type of quantum order, the charge-density-wave (CDW) phase, which manifests itself through a modulation of the charge density with a wave vector $q = 2k_F$, where k_F is the Fermi wave vector (not necessarily commensurate with the nanotube). The well-known case of the Peierls transition in monatomic chains at half-filling, accompanied by a dimerization and a band-gap opening, is a specific example of such an instability related to the more general Kohn anomaly (Kohn, 1959). While the SC transition induces the creation or destruction of electron (Cooper) pairs, the CDW is induced by the spontaneous formation of electron-hole excitations. The CDW instability is very specific to 1D systems while the SC one occurs irrespective of the dimension. An important point related to the CDW and SC instabilities is that they are in general incompatible, meaning that the occurrence of one usually destroys the other. As a result, the discussion of SC in nanotubes needs to be associated with that of the CDW (or Peierls) transition.

Further, even if the SC prevails over the CDW instability, its manifestation in nanotubes should be very peculiar as, in 1D systems, the existence of a phase-

coherent order over macroscopic distances is strongly suppressed by both thermal (Mermin and Wagner, 1966) and quantum fluctuations. By 1D systems, we mean systems for which the largest transverse direction is significantly smaller than the longitudinal superconducting coherence length ξ. The physics of quantum fluctuations stems from the phenomenon of phase slip (Langer and Ambegaokar, 1967; Tinkham, 1996) which manifests itself by the appearance of an intrinsic resistive character below the bulk T_C value in a narrow superconducting wire. In particular, the resistance of the wire, instead of dropping abruptly to zero below T_C, smoothly decays with nonzero values down to 0 K. The manifestation of phase slips was also provided in the case of ultrathin superconducting wires (Bezryadin et al., 2000).

After giving many good reasons for not observing a SC order in nanotubes, the fact remains that it has been clearly seen evidenced experimentally, with a rather large T_C in the a priori most disfavorable case of isolated (that is, more 1D-like) nanotubes synthesized in pores of zeolites. This explains the large interest generated in the theory community with several attempts to refine the description of the electron-electron and electron-phonon interactions at low energy (that is, for energies around that of relevant phonons). In particular, and as the electronic states around E_F were already well known, two important questions mainly arose: (i) which phonons are responsible for the EPC and (ii) what is the influence of putting nanotubes in a bundle geometry, both on the screening of the Coulomb interactions and on the possibility for Cooper pairs to tunnel (Josephson coupling) from one tube to another. The relevance of this last point is clearly to question the effective dimensionality of the tubes in order to circumvent the abovementioned difficulty of survival of SC order in 1D systems.

As in the case of fullerenes, the weakness of intertube interactions leads to the conclusion that on-tube phonons are responsible for the main EPC channels. As such, early studies of the electron-phonon interaction focused on isolated tubes and in particular on the possible occurrence of a Peierls instability. Such an instability is always expected to occur in 1D systems, and the relevant question is to know the transition temperature T_{CDW} (as the instability is quenched at sufficiently high temperature). This was the idea behind the title "Are fullerene tubules metallic?" of one of the first theoretical studies of nanotubes (Mintmire et al., 1992). By comparison with the case of polyacetylene, Mintmire and co-workers concluded that the mean-field Peierls transition temperature in nanotubes, with respect to coupling to $q=2k_F$ phonons, should be extremely small, below 1 K.

The Peierls (or CDW) instability in nanotubes was subsequently studied in several papers (Saito et al., 1992; Harigaya and Fujita, 1993; Huang et al., 1996; Tanaka et al., 1997; Sédéki et al., 2000), where specific deformation modes (in-plane, out-of-plane, etc.) and parametrized model interactions were considered, leading to a variety of results with, in particular, T_{CDW} ranging from ~9.1 K
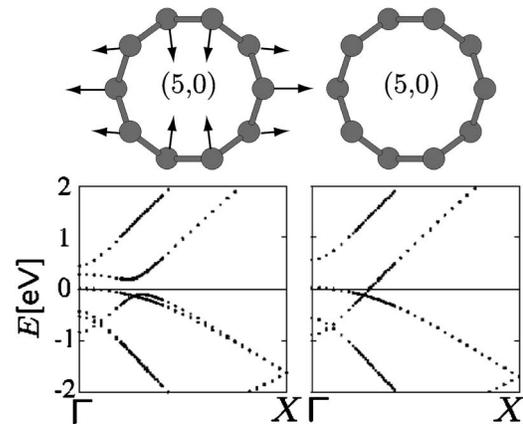
FIG. 56. Schematic representation of a Peierls instability in a (5,0) nanotube (left) compared to the perfectly cylindrical (5,0) nanotube (right). This instability opens spontaneously a band gap (0.2 eV) in the electronic structure of the perfect (D_{5d} symmetry) tube. Adapted from Connétable et al., 2005.

(Huang et al., 1996) to 15 K (Sédéki et al., 2000) for a (5,5) tube. Such temperatures are clearly larger than, or equivalent to, the experimental T_C for the SC instability.

Following our discussion of electron-phonon coupling (Sec. IV.E.1), the coupling to long-wavelength acoustic modes such as twistons or radial breathing modes (derived from the transverse acoustic modes of graphite) was also studied as a means to induce a CDW instability (Figge et al., 2001; De Martino and Egger, 2003). The related Peierls transition temperature was estimated by Figge et al. to be around 10 K for an (8,8) tube, which is again larger than or equivalent to the experimental T_C.

The softening of phonons by electron-phonon interactions and the Peierls transition was carefully studied in the specific case of small 4-Å tubes using DFT calculations (Bohnen et al., 2004; Connétable et al., 2005). The increase of the coupling with radius (Sec. IV.E.1) was shown to lead to a Peierls distortion at several hundred Kelvin mediated by $2k_F$ phonons in the (3,3) armchair case (Bohnen et al., 2004; Connétable et al., 2005). Further, in the case of the (5,0) tube, the other possible candidate for a SC transition, a long-wavelength "squashing mode" was found by Connétable and co-workers (2005) to induce a band gap opening mechanical instability at room temperature (Fig. 56). Such results seem incompatible with the observed SC transition at ~15 K (Tang et al., 2001). However, the same (5,0) tube was studied within a self-consistent tight-binding approach (Barnett et al., 2005), yielding results compatible with the experimental observation, namely, that the CDW instability can be made weaker than the SC one, provided that Coulomb interactions are treated beyond the mean field. This last point raises the important question of the validity of mean-field techniques, such as the DFT, to describe low-energy excitations in nanotubes.

The possible failure of single-particle theories paves the way to many-body techniques such as those based on bozonization and the renormalization group (RG). Such approaches have been used to study electron-electron

interactions in the Luttinger-liquid phase and can be generalized to address the CNT quantum phase diagram upon switching of the electron-phonon interactions. The true many-body functional form of the Hamiltonian is preserved but several approximations are performed, such as the linearization of bands around the Fermi level. Further, the strengths of the electron-electron and electron-phonon interactions (the g_i constants of Sec. IV.E.3 and the deformation potentials of Sec. IV.E.1) are taken as adjustable parameters, so that the results are often presented as a phase diagram in parameter space with areas dominated by CDW or SC instabilities, and it is not easy to decide which parameters should be taken for realistic systems.

Using such RG techniques, Kamide *et al.* (2003) concluded that a SC order may dominate in the (5,0) tube provided that the electron-phonon interaction is strong enough. This conclusion contradicts previous studies based on RG analysis which concluded, on the contrary, that, in isolated nanotubes, Coulomb repulsion should easily overcome the attractive interaction mediated by phonons (González, 2002; Sédéki *et al.*, 2002; Alvarez and González, 2003; De Martino and Egger, 2004). This conclusion led these authors to determine that SC fluctuations are expected to occur in bundles containing a large number of (metallic) tubes, as confirmed by the evolution of T_C with the number of estimated tubes in various SWNT bundles (Kasumov *et al.*, 2003). Both the better screening in nanotube bundles, which allows one to reduce long-range Coulomb repulsion, and the possibility for Cooper pairs to tunnel from one tube to another, thus reducing the 1D character of the superconducting sample, are strong arguments in favor of the important role of tube-tube interactions. Upon inclusion of quantum phase slip effects, the experimental temperature-dependent profile of the resistance below T_C for nanotube bundles (Kasumov *et al.*, 2003) could be reproduced on the basis of theory (De Martino and Egger, 2004). In the case of zeolite-inserted small-radius tubes, the screening by the zeolite, by contacting electrodes, and by other tubes, has also been invoked as an important factor that may decide the strongest relevant instability (González and Perfetto, 2005), even though a possible dominant triplet-state superconducting instability was suggested to arise from the specific three-band topology at the Fermi level of isolated C(5,0) tubes (Carpentier and Orignac, 2006).

The physics of superconductivity in nanotubes remains a challenging subject. The difficulties in estimating the transition temperatures can be related to our discussion of the EPC deformation potential strength in Sec. IV.E.1. In the normal state, the relevant quantities, such as the inelastic mean free path, depend quadratically on the deformation potential through the Fermi golden rule. In the case of the superconducting transition temperature, the dependence is exponential as illustrated in the McMillan formula
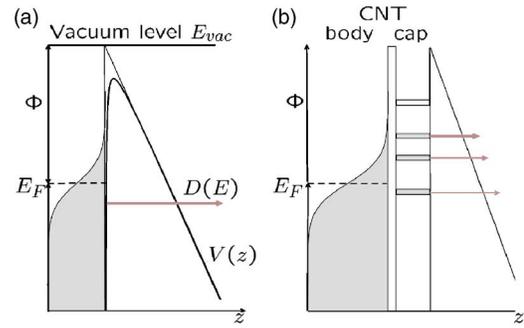
FIG. 57. (Color online) Symbolic energy diagram for cold cathodes Left: The shaded area represents the Fermi-Dirac distribution of occupied states. Inclusion of the image charge potential reduces the triangular barrier $V(z)$ (thin line) to the rounded one (thick line). Right: Illustration of the resonant tunneling process involving tip states. The work function ϕ of CNTs, which is radius dependent, is of the order of 4.5–5.0 eV.

$$T_C = \frac{\hbar \omega_{\log}}{1.2 k_B} \exp\left[\frac{-1.04(1+\lambda)}{\lambda - \mu^*(1 + 0.62\lambda)} \right], \qquad (69)$$

where $\omega_{\log}$ is some average phonon frequency, λ is the e-ph coupling constant (proportional to an average over the Fermi surface of the EPC matrix elements squared), and μ^* is the screened and retarded Coulomb repulsion parameter. The validity of such a formula for CNTs is certainly questionable but Eq. (69) illustrates qualitatively that the difficulty in obtaining accurate electron-electron and electron-phonon interaction parameters prevents the emergence of a clear and conclusive understanding of the experimental situation.

G. Field emission from nanotubes

Field emission (FE) from nanotubes (Chernozatonskii *et al.*, 1995; De Heer *et al.*, 1995; Rinzler *et al.*, 1995), that is, the use of CNTs as a source of electrons under applied electric field, is one of the most promising fields of application and several prototypes have been demonstrated, including flat panel displays, lighting elements, high-brightness electron microscopy sources, rf amplifiers, portable x-ray systems, and ionization vacuum gauges (see Purcell *et al.*, 2006, for detailed references). Several extensive articles have been written in the field (Lovall *et al.*, 2000; Bonard *et al.*, 2001; de Jonge and Bonnard, 2004), and we provide below just a summary of the underlying physical ideas and research issues. A general review of field emission can be found in Gadzuk and Plummer (1973).

The basic FE principles are illustrated in Fig. 57(b). Electrons at the Fermi level in solids need to overcome a potential barrier ϕ to be emitted through the surface into the vacuum. ϕ is the work function specific to the material and surface crystallographic direction. This barrier can be overcome by providing thermal energy to the carriers. This is the thermoionic effect used in standard cathodic tubes. However, under application of an electric field, the potential barrier $V(z)$ seen by electrons can

be reduced dramatically by a quantity $-eFz$, z being the distance to the surface and F the magnitude of the electric field. The thinning of the potential barrier allows for electrons to tunnel out of the solid even at zero temperature. This is the principle of field emission used in cold cathodes.

The probability of emission $P(E)$ increases with the electron energy E. However, the temperature-dependent Fermi-Dirac distribution $f_{T,E_F}(E)$ dramatically reduces the number of electrons above the Fermi level available for tunneling. The current density $J(E)$ results from a trade-off between the evolution of $P(E)$ and $f_{T,E_F}(E)$:

$$J(E) = 2e \int_{\mathbf{k}} f_{T,E_F}(E) P(E) v_z \frac{d^3\mathbf{k}}{(2\pi)^3}, \qquad (70)$$

with $\mathbf{k}$ the momentum of the electronic states and $v_z = \hbar k_z/m$ the electron velocity in the direction of emission within the free-electron model. This tunneling current can be calculated analytically by assuming a semi-infinite jellium of electrons and a tunnel probability $P(E)$ given by the semiclassical Wentzel-Kramers-Brillouin (WKB) approximation, namely,

$$P_{\text{WKB}} = \exp\left[-2\left(\frac{2m}{\hbar^2}\right)^{1/2} \int_{z_1}^{z_2} dz \sqrt{V(z) - E_z} \right], \qquad (71)$$

with $E_z = \hbar^2 k_z^2/2m$ the kinetic energy in the direction of emission. The integral limits (z_1, z_2) are the classical turning points defined by $V(z_i) = E_z$. Assuming a triangular potential barrier $V(z) = E_{\text{vac}} - eFz$ and solving $(E_{\text{vac}} - E_z)^{3/2}$ to first order in $E_F - E_z$, one obtains

$$P_{\text{WKB}} = \exp\left[-\frac{4\phi^{3/2}}{3eF}\left(\frac{2m}{\hbar^2}\right)^{1/2} \right]$$
$$\times \exp\left[\left(\frac{2m}{\hbar^2}\right)^{1/2} \frac{2\phi^{1/2}}{eF}(E_z - E_F) \right]. \qquad (72)$$

Equation (72) relies on several severe approximations, including neglect of the image charge potential (interaction of the electron with the hole left behind), but it is known to work qualitatively well for metallic surfaces. Equation (72) can then be used to obtain the Fowler-Nordheim equation for the emission current density which, at zero temperature, reads

$$J_{\text{FN}} = \frac{e}{4(2\pi)^2\hbar\phi} F^2 \exp\left[-\frac{4\sqrt{2m}\phi^{3/2}}{3\hbar eF} \right]. \qquad (73)$$

While the use of such a formula in the case of a thin metallic object such as a CNT is certainly subject to criticisms (Fransen *et al.*, 1999; Lovall *et al.*, 2000; Bonard *et al.*, 2004), it clearly illustrates that the emitted current density J depends exponentially on the material work function and the value of the electrostatic field F at the CNT cap. The great advantage of nanotubes in this respect is the well-known field enhancement effect at sharp metallic tips resulting from self-consistent rearrangement of charges upon applied external field. The local electric field $F_l(\text{tip})$ is much larger than the applied field with a proportionality factor γ which is a purely geometrical factor; namely, $F_l(\text{tip}) = \gamma F = \gamma V/d$, with V the drop in potential between two planar electrodes separated by a distance d. This amplification of the field was already exploited in the so-called Spindt cathodes made of sharp conical metallic emitters. The values of γ can be shown to be proportional to h/r for a vertically aligned model metallic cylinder of length h terminated by an hemisphere of radius r ($h \ll r$) (Bonard *et al.*, 1998; Edgcombe and Valdré, 2001). This scaling is the crucial difficulty for theoretical approaches as it requires one to study prohibitively long tubes, a difficulty that is often bypassed by studying short tubes with a very large external applied field (Adessi and Devel, 2002; Han *et al.*, 2002; Buldum and Lu, 2003; Zheng *et al.*, 2004; Khazaei *et al.*, 2005).

A high γ value related to this qualitative h/r behavior applies to isolated tubes. Upon gathering of tubes in mats or bundles, the γ factor collapses dramatically as the electric field at the tip of a given CNT is strongly screened by neighboring tubes. It has been estimated that tubes must be separated by a distance $l \geqslant 2h$ in order to recover the isolated tube γ value (Nilsson *et al.*, 2000). To maximize the emitted current per surface area, a trade-off must be found between the emitter surface density and the amplification factor.

An interesting issue concerning the physics of CNT emission is the role of tip states. The analysis of the emission patterns, that is, the shape of the bright spots observed on electrosensitive screens facing an emitting isolated CNT, was interpreted in several works as providing a direct signature of the atomic structure and related local electronic structure of tube tips (Carroll *et al.*, 1997; Saito, Hata, and Murata, 2000). This interpretation hinges on the physics of resonant tunneling as illustrated in Fig. 57. The tunneling probability is related to the decay of the electronic wave functions into the vacuum across the potential barrier. As such, it is expected to be related to the electronic states at the tube tip. However, electrons which will tunnel can only be carried from the anode to the emitting tip by extended Bloch states corresponding to the tube body. Such propagating wave packets will first tunnel into the tip states before being emitted. One may thus expect that the energy and spatial decomposition of the current carry information on the CNT caps.

The interest in FE from CNTs does not reside only in its technological applications. Field emission is also a powerful characterization tool. The analysis of the current density [Eq. (70)] shows that valuable information on the work function, CNT bulk and apex density of states, tip temperature, etc., can be extracted from the I/V characteristics and the energy-resolved decomposition of the emitted current. It can also be used to observe directly the mechanical vibration resonances of CNTs from which elastic moduli can be inferred (Purcell *et al.*, 2002b). Further, the analysis of the temperature at the tube apex and knowledge of the emitted current provide quantitative information on the tube electrical re-

sistivity, even though it is not a trivial task to separate the contribution from heat radiation and Joule heating (Purcell *et al.*, 2002a; Vincent *et al.*, 2002). Finally, FE from growing CNTs has been used to provide some estimate of the tube growth rates in a CVD reactor (Bonard and Croci, 2002).

V. CONCLUSION

The field of nanotubes is still rapidly growing. As emphasized, many questions are still unanswered. The dynamics of hot electrons (and electron-hole pairs) in optical experiments, the nature of the contact resistance at metallic electrode interfaces, the effect of an out-of-equilibrium phonon distribution on inelastic scattering, and the domain of existence of the Luttinger-liquid, charge-density-wave, and superconducting phases are still subjects which require a considerable amount of work and understanding. Further, and beyond the intrinsic properties of nanotubes, the physics of functionalized, chemisorbed, doped, or excited CNTs is driven by potential applications in molecular electronics, optoelectronics, and sensors. Such themes are still largely unexplored areas for theorists: while early theoretical papers preceded experiments on the discussion of the basic electronic properties of pristine tubes, such complex systems and applications have now been demonstrated experimentally and theory is lagging behind.

The field of nanotubes has fostered much interest in related systems such as graphene or semiconducting nanowires. The actual synthesis of isolated graphene sheets or few-layer graphite materials (Novoselov *et al.*, 2004) and the sudden interest generated by such a synthesis come nearly 15 years after the development of nanotubes. This is an amazing twist of history as the properties of nanotubes are usually derived, as in Sec. III, from those of graphene. Charge carriers around the charge-neutrality point in graphene show a very high mobility with a Dirac-like behavior, namely, an energy-independent velocity (Novoselov *et al.*, 2005, 2006; Zhang *et al.*, 2005; Berger *et al.*, 2006; Ohta *et al.*, 2006, Zhou *et al.*, 2006). In the case of graphene nanoribbons, confinement effects induce a width- and orientation-dependent band-gap opening (Son *et al.*, 2006a) and one is back to the size and helicity selection that complicates the use of nanotubes in applications. Other interesting properties, such as a half-metalic behavior, where spin-up and spin-down electrons display a different metallicity, have been proposed (Son *et al.*, 2006b).

Semiconducting nanowires (Si, GaN, etc.) also offer an interesting alternative to nanotubes as they do not exhibit the problem of the variation of the band gap with chirality. Through confinement, an effect well described within simple effective mass or more sophisticated quasiparticle approaches (Niquet *et al.*, 2006), the band gap depends only on the wire radius. Further, while the band gap of nanotubes lies in the infrared, with difficulties in obtaining a strong PL signal, III-V or II-VI nanowires and their related heterostructures are well adapted to optoelectronic applications in the visible range (Duan *et al.*, 2001; Bjork *et al.*, 2002). Topics such as integration in FETs (Duan *et al.*, 2001; Huang *et al.*, 2001; Martensson *et al.*, 2004; Wang *et al.*, 2006) and functionalization for chemical sensing (Cui *et al.*, 2001) are also being developed and discussed in the field of nanowires. It is interesting to note that, while the channel of existing standard Si-based transistors is now routinely reaching the few tens of nanometer range, semiconducting nanowires are regarded as new objects with strong technological potential. The difficulty in obtaining structurally perfect wires with controlled radius, surface roughness, and dopant density is certainly as large a challenge as controlling the radius and helicity of tubes during synthesis.

REFERENCES

Adessi, Ch., and M. Devel, 2002, Phys. Rev. B **65**, 075418.
Adessi, Ch., S. Roche, and X. Blase, 2006, Phys. Rev. B **73**, 125414.
Aharonov, Y., and D. Bohm, 1959, Phys. Rev. **115**, 485.
Ajayan, P. M., T. W. Ebbesen, T. Ichihashi, S. Iijima, K. Tanigaki, and H. Hiura, 1993, Nature (London) **362**, 522.
Ajiki, H., and T. Ando, 1993, J. Phys. Soc. Jpn. **62**, 1255.
Ajiki, H., and T. Ando, 1994, Physica B **201**, 349.
Ajiki, H., and T. Ando, 1996, J. Phys. Soc. Jpn. **65**, 505.
Altshuler, B. L., and A. G. Aronov, 1985, in *Electron-Electron Interactions in Disordered Systems*, edited by A. L. Efros and M. Pollak (North-Holland, Amsterdam).
Altshuler, B. L., A. G. Aronov, and B. Spivak, 1981, JETP Lett. **33**, 94.
Alvarez, J. V., and J. González, 2003, Phys. Rev. Lett. **91**, 076401.
Anantram, M. P., 2000, Phys. Rev. B **62**, R4837.
Anantram, M. P., 2001, Appl. Phys. Lett. **78**, 2055.
Anantram, M. P., and T. R. Govindan, 1998, Phys. Rev. B **58**, 4882.
Ando, T., 1997, J. Phys. Soc. Jpn. **66**, 1066.
Ando, T., 2004, J. Phys. Soc. Jpn. **73**, 3351.
Ando, T., 2005, J. Phys. Soc. Jpn. **74**, 777.
Ando, T., and T. Nakanishi, 1998, J. Phys. Soc. Jpn. **67**, 1704.
Ando, T., T. Nakanishi, and R. Saito, 1998, J. Phys. Soc. Jpn. **67**, 2857.
Ando, T., and S. Seri, 1997, J. Phys. Soc. Jpn. **66**, 3558.
Appenzeller, J., J. Knoch, M. Radosavljević, and Ph. Avouris, 2004, Phys. Rev. Lett. **92**, 226802.
Arenal, R., O. Stéphan, M. Kociak, D. Taverna, A. Loiseau, and C. Colliex, 2005, Phys. Rev. Lett. **95**, 127601.
Arnaud, B., S. Lebégue, P. Rabiller, and M. Alouani, 2006,

Phys. Rev. Lett. **96**, 026402.

Auvray, S., V. Derycke, M. Goffman, A. Filoramo, O. Jost, and J.-P. Bourgoin, 2005, Nano Lett. **5**, 451.

Avriller, R., S. Latil, F. Triozon, X. Blase, and S. Roche, 2006, Phys. Rev. B **74**, 121406.

Bachilo, S. M., M. S. Strano, C. Kittrell, R. H. Hauge, R. E. Smalley, and R. B. Weisman, 2002, Science **298**, 2361.

Bachtold, A., C. Strunk, J.-P. Salvetat, J.-M. Bonard, L. Forró, T. Nussbaumer, and C. Schönenberger, 1999, Nature (London) **397**, 673.

Baeriswyl, D., and L. Degiorgi, 1990, *Strong Interactions in Low Dimensions* (Kluwer Academic, Dordrecht).

Bahr, J. L., J. P. Yang, D. V. Kosynkin, M. J. Bronikowski, R. E. Smalley, and J. M. Tour, 2001, J. Am. Chem. Soc. **123**, 6536.

Bai, X. D., E. G. Wang, and J. Yu, Hui Yang, 2000, Appl. Phys. Lett. **77**, 67.

Balents, L., and M. P. A. Fisher, 1997, Phys. Rev. B **55**, R11973.

Banhart, F., 1999, Rep. Prog. Phys. **62**, 1181.

Barnett, R., E. Demler, and E. Kaxiras, 2005, Phys. Rev. B **71**, 035429.

Baughman, R. H., Anvar A. Zakhidov, and Walt A. de Heer, 2000, Science **297**, 787.

Bellucci, S., J. Gonzalez, and P. Onorato, 2005, Phys. Rev. Lett. **95**, 186403.

Beenakker, C. W., 1997, Rev. Mod. Phys. **69**, 731.

Bendiab, N., L. Spina, A. Zahab, P. Poncharal, C. Marliere, J. L. Bantignies, E. Anglaret, and J. L. Sauvajol, 2001, Phys. Rev. B **63**, 153407.

Benedict, L. X., V. H. Crespi, S. G. Louie, and M. L. Cohen, 1995, Phys. Rev. B **52**, 14935.

Benedict, L. X., S. G. Louie, and M. L. Cohen, 1995, Phys. Rev. B **52**, 8541.

Berger, C., Z. Song, X. Li, X. Wu, N. Brown, C. Naud, D. Mayou, T. Li, J. Hass, A. N. Marchenkov, E. H. Conrad, P. N. First, and W. A. de Heer, 2006 Science **312**, 1191.

Bethune, D. S., C. H. Kiang, M. S. de Vries, G. Gorman, R. Savoy, J. Vazquez, and R. Beyers, 1993, Nature (London) **363**, 605.

Bezryadin, A., C. N. Landau, and M. Tinkham, 2000, Nature (London) **404**, 971.

Biel, B., F. J. García-Vidal, A. Rubio, and F. Flores, 2005, Phys. Rev. Lett. **95**, 266801.

Bjork, M. T., B. J. Ohlsson, T. Sass, A. I. Persson, C. Thelander, M. H. Magnusson, K. Deppert, L. R. Wallenberg, and L. Samuelson, 2002, Appl. Phys. Lett. **80**, 1058.

Blase, X., Ch. Adessi, and D. Connétable, 2004, Phys. Rev. Lett. **93**, 237004.

Blase, X., L. X. Benedict, E. L. Shirley, and S. G. Louie, 1994, Phys. Rev. Lett. **72**, 1878.

Blase, X., J.-C. Charlier, A. De Vita, and R. Car, 1997, Appl. Phys. Lett. **70**, 197.

Blase, X., A. De Vita, J.-C. Charlier, and R. Car, 1999, Appl. Phys. A: Mater. Sci. Process. **68**, 293.

Blase, X., A. Rubio, M. L. Cohen, and S. G. Louie, 1994, Europhys. Lett. **28**, 335.

Bockrath, M., D. H. Cobden, J. Lu, A. G. Rinzler, R. E. Smalley, L. Balents, and P. L. McEuen, 1999, Nature (London) **397**, 598.

Bohnen, K.-P., R. Heid, H. J. Liu, and C. T. Chan, 2004, Phys. Rev. Lett. **93**, 245501.

Bonard, J.-M., and M. Croci, 2002 Appl. Phys. Lett. **81**, 2836.

Bonard, J.-M., K. Dean, B. Coll, and C. Klinke, 2004, Phys.

Rev. Lett. **89**, 197602.

Bonard, J.-M., H. Kind, T. Stöckli, and L. A. Nilsson, 2001, Solid-State Electron. **45**, 893.

Bonard, J.-M., T. Stöckli, F. Maier, W. A. de Heer, and A. Chatelain, 1998, Phys. Rev. Lett. **81**, 1441.

Bourlon, B., C. Miko, L. Forro, D. C. Glattli, and A. Bachtold, 2004, Phys. Rev. Lett. **93**, 176806.

Buldum A., and J. P. Lu, 2003, Phys. Rev. Lett. **91**, 236801.

Büttiker, M., Y. Imry, R. Landauer, and S. Pinhas, 1985, Phys. Rev. B **31**, 6207.

Cabria, I., J. W. Mintmire, and C. T. White, 2003, Phys. Rev. B **67**, 121406.

Cao, J., Q. Wang, M. Rolandi, and H. Dai, 2004, Phys. Rev. Lett. **93**, 216803.

Carpentier, D., and E. Orignac, 2006, Phys. Rev. B **74**, 085409 (2006).

Carroll, D. L., Ph. Redlich, P. M. Ajayan, J.-C. Charlier, X. Blase, A. De Vita, and R. Car, 1997, Phys. Rev. Lett. **78**, 2811.

Chakravarty, S., and A. Schmidt, 1986, Phys. Rep. **140**, 193.

Chang, E., G. Bussi, A. Ruini, and E. Molinari, 2004, Phys. Rev. Lett. **92**, 196401.

Charlier, J.-C., 2002, Acc. Chem. Res. **35**, 1063.

Charlier, J.-C., T. W. Ebbesen, and Ph. Lambin, 1996, Phys. Rev. B **53**, 11108.

Charlier, J.-C., X. Gonze, and J.-P. Michenaud, 1991, Phys. Rev. B **43**, 4579.

Charlier, J.-C., X. Gonze, and J.-P. Michenaud, 1994, Europhys. Lett. **28**, 403.

Charlier, J.-C., X. Gonze, and J.-P. Michenaud, 1995, Europhys. Lett. **29**, 43.

Charlier, J.-C., and Ph. Lambin, 1998, Phys. Rev. B **57**, R15037.

Charlier, J.-C., and J.-P. Michenaud, 1993, Phys. Rev. Lett. **70**, 1858.

Charlier, J.-C., and G.-M. Rignanese, 2001, Phys. Rev. Lett. **86**, 5970.

Chen, J., V. Perebeinos, M. Freitag, J. Tsang, Q. Fu, J. Liu, and P. Avouris, 2005, Science **310**, 1171.

Chen, J., and L. Yang, 2005, J. Phys.: Condens. Matter **17**, 957.

Chen, Y., J. C. Barnard, R. E. Palmer, and M. O. Watanabe, 1999, Phys. Rev. Lett. **83**, 2406.

Chen, Z. H., J. Appenzeller, J. Knoch, Y. M. Lin, and P. Avouris, 2005, Nano Lett. **5**, 1497.

Chernozatonskii, L. A., Y. V. Gulyaev, Z. J. Kosakovskaja, N. I. Sinitsyn, G. V. Torgashov, Y. F. Zakharchenko, E. A. Fedorov, and V. P. Val'chuk, 1995, Chem. Phys. Lett. **233**, 63.

Chico, L., L. X. Benedict, S. G. Louie, and M. L. Cohen, 1996, Phys. Rev. B **54**, 2600.

Chico, L., V. H. Crespi, L. X. Benedict, S. G. Louie, and M. L. Cohen, 1996, Phys. Rev. Lett. **76**, 971.

Chico, L., M. P. López Sancho, and M. C. Muñoz, 1998, Phys. Rev. Lett. **81**, 1278.

Chiu, P. W., G. S. Duesberg, U. Dettlaff-Weglikowska, and S. Roth, 2002, Appl. Phys. Lett. **80**, 3811.

Chiu, P.-W., M. Kaempgen, and S. Roth, 2004, Phys. Rev. Lett. **92**, 246802.

Choi, H. J., J. Ihm, S. G. Louie, and M. L. Cohen, 2000, Phys. Rev. Lett. **84**, 2917.

Cobden, D. H., *et al.*, 1998, Phys. Rev. Lett. **81**, 681.

Collins, P. G., K. Bradley, M. Ishigami, and A. Zettl, 2000, Science **287**, 1801.

Connétable, D., G.-M. Rignanese, J.-C. Charlier, and X. Blase, 2005, Phys. Rev. Lett. **94**, 015503.

Connétable, D., V. Timoshevskii, B. Masenelli, J. Beille, J.

Marcus, B. Barbara, A. M. Saitta, G.-M. Rignanese, P. Méli-non, S. Yamanaka, and X. Blase, 2003, Phys. Rev. Lett. **91**, 247001.

Coskun, U. C., T.-C. Wei, S. Vishveshwara, P. M. Goldbart, and A. Bezryadin, 2004, Science **304**, 1132.

Crespi, V. H., M. L. Cohen, and A. Rubio, 1997, Phys. Rev. Lett. **79**, 2093–2096.

Cui, Y., Q. Wei, H. Park, and C. M. Lieber, 2001, Science **293**, 1289.

Dag, S., O. Gulseren, S. Ciraci, and T. Yildirim, 2003, Appl. Phys. Lett. **83**, 3180.

Damnjanović, M., I. Milošević, T. Vuković, and R. Sredanović, 1999, Phys. Rev. B **60**, 2728.

Datta, S., 1995, *Electronic Transport in Mesoscopic Systems* (Cambridge University Press, Cambridge, England).

Dayen, J.-F., T. L. Wade, M. Konczykowski, J.-E. Wegrowe, and X. Hoffer, 2005, Phys. Rev. B **72**, 073402.

De Heer, W. A., A. Chatelain, and D. Ugarte, 1995, Science **270**, 1179.

de Jonge, N., and J.-M. Bonnard, 2004, Philos. Trans. R. Soc. London, Ser. A **362**, 2239.

Delaney, P., H. J. Choi, J. Ihm, S. G. Louie, and M. L. Cohen, 1998, Nature (London) **391**, 466.

De Martino, A., and R. Egger, 2003, Phys. Rev. B **67**, 235418.

De Martino, A., and R. Egger, 2004, Phys. Rev. B **70**, 014508.

Derycke, V., R. Martel, J. Appenzeller, and Ph. Avouris, 2002, Appl. Phys. Lett. **15**, 2773.

De Vita, A., J.-C. Charlier, X. Blase, and R. Car, 1999, Appl. Phys. A: Mater. Sci. Process. **68**, 283.

DiVicenzo, D. P., and E. J. Mele, 1984, Phys. Rev. B **29**, 1685.

Dresselhaus, M. S., G. Dresselhaus, and Ph. Avouris, 2001, *Carbon Nanotubes*, Topics in Applied Physics Vol. 80 (Springer-Verlag, Berlin).

Dresselhaus, M. S., G. Dresselhaus, and P. C. Eklund, 1996, *Science of Fullerenes and Carbon Nanotubes* (Academic, San Diego, CA).

Dresselhaus, M. S., G. Dresselhaus, R. Saito, and A. Jorio, 2005, Phys. Rep. **409**, 47.

Dresselhaus, M. S., and P. C. Eklund, 2000, Adv. Phys. **49**, 705–814.

Duan, X. F., Y. Huang, Y. Cui, J. F. Wang, and C. M. Lieber, 2001, Nature (London) **409**, 66.

Dubay, O., and G. Kresse, 2003, Phys. Rev. B **67**, 035401.

Dubay, O., G. Kresse, and H. Kuzmany, 2002, Phys. Rev. Lett. **88**, 235506.

Dunlap, B. I., 1994, Phys. Rev. B **49**, 5643.

Ebbesen, T. W., 1997, *Carbon Nanotubes: Preparation and Properties* (CRC, Boca Raton, FL).

Edgcombe, C., and U. Valdré, 2001, J. Microsc. **203**, 188.

Egger, R., 1999, Phys. Rev. Lett. **83**, 5547.

Egger, R., and A. O. Gogolin, 1997, Phys. Rev. Lett. **79**, 5082.

Egger, R., and A. O. Gogolin, 1998, Eur. Phys. J. B **3**, 281.

Egger, R., and A. O. Gogolin, 2001, Phys. Rev. Lett. **87**, 066401.

Eggert, S., 2000, Phys. Rev. Lett. **84**, 4413.

El-Barbary, A. A., R. H. Telling, C. P. Ewels, M. I. Heggie, and P. R. Briddon, 2003, Phys. Rev. B **68**, 144107.

Elliott, R. J., 1957, Phys. Rev. **108**, 1384.

Endo, M., S. Iijima, and M. S. Dresselhaus, 1996, *Carbon Nanotubes* (Pergamon, Amsterdam).

Ewels, C. P., and M. Glerup, 2005, J. Nanosci. Nanotechnol. **5**, 1345.

Ewels, C. P., M. I. Heggie, and P. R. Briddon, 2002, Chem.

Phys. Lett. **351**, 178.

Fan, X., E. C. Dickey, P. C. Eklund, K. A. Williams, L. Grigo-rian, R. Buczko, S. T. Pantelides, and S. J. Pennycook, 2000, Phys. Rev. Lett. **84**, 4621.

Fan, Y., B. R. Goldsmith, and P. G. Collins, 2005, Nat. Mater. **4**, 906.

Fedorov, G., B. Lassagne, M. Sagnes, B. Raquet, J. M. Broto, F. Triozon, S. Roche, and E. Flahaut, 2005, Phys. Rev. Lett. **94**, 066801.

Fernández-Serra, M.-V., 2006, unpublished.

Fernández-Serra, M.-V., Ch. Adessi, and X. Blase, 2006a, Phys. Rev. Lett. **96**, 166805.

Fernández-Serra, M.-V., Ch. Adessi, and X. Blase, 2006b, Nano Lett. **6**, 2674.

Figge, M. T., M. Mostovoy, and J. Knoester, 2001, Phys. Rev. Lett. **86**, 4572.

Foa-Torres, L., and S. Roche, 2006, Phys. Rev. Lett. **97**, 076804.

Frank, S., P. Poncharal, Z. L. Wang, and W. A. de Heer, 1998, Science **280**, 1744.

Fransen, M., T. van Rooy, and P. Kruit, 1999, Appl. Surf. Sci. **146**, 312.

Fujiwara, A., K. Tomiyama, H. Suematsu, M. Yumura, and K. Uchida, 1999, Phys. Rev. B **60**, 13492.

Gadzuk, J. W., and E. W. Plummer, 1973, Rev. Mod. Phys. **45**, 487.

Gao, B., A. Komnik, R. Egger, D. C. Glattli, and A. Bachtold, 2004, Phys. Rev. Lett. **92**, 216804.

Gavillet, J., 2001, Ph.D. thesis (ONERA–Universitè Paris VI)

Georghe, M., R. Gutierrez, A. Pecchia, A. di Carlo, and G. Cuniberti, 2005, Europhys. Lett. **71**, 438.

Giamarchi, T., 2004, *Quantum Physics in One Dimension* (Oxford Science, Oxford).

Giannozzi, P., R. Car, and G. Scoles, 2003, J. Chem. Phys. **118**, 1003.

Gómez-Navarro, G., P. J. De Pablo, J. Gómez-Herrero, B. Biel, F.-J. Garcia-Vidal, A. Rubio, and F. Flores, 2005, Nat. Mater. **4**, 534.

González, J., 2002, Phys. Rev. Lett. **88**, 076403.

González, J., F. Guinea, and M. A. H. Vozmediano, 1996, Phys. Rev. Lett. **77**, 3589 (1996).

González, J., and B. Perfetto, 2005, Phys. Rev. B **72**, 205406.

Grabert, H., and M. H. Devoret, 1992, *Single Electron Tunnelling: Coulomb Blockade Phenomena in Nanostructure* (Plenum, New York).

Grigorian, L., K. A. Williams, S. Fang, G. U. Sumanasekera, A. L. Loper, E. C. Dickey, S. J. Pennycook, and P. C. Eklund, 1998, Phys. Rev. Lett. **80**, 5560.

Guo, T., C.-M. Jin, and R. E. Smalley, 1995, Chem. Phys. Lett. **243**, 49.

Haeckel, E., 1998, *Art Forms in Nature* (Prestel-Verlag, Berlin).

Hagen, A., G. Moos, V. Talalaev, and T. Hertel, 2004, Appl. Phys. A: Mater. Sci. Process. **78**, 1137 (2004).

Hagen, A., M. Steiner, M. B. Raschke, C. Lienau, T. Hertel, H. Qian, A. J. Meixner, and A. Hartschuh, 2005, Phys. Rev. Lett. **95**, 197401 (2005).

Haldane, F. D. M., 1981, J. Phys. C **14**, 2585.

Hamada, N., S. Sawada, and A. Oshiyama, 1992, Phys. Rev. Lett. **68**, 1579.

Han, S., M. H. Lee, and J. Ihm, 2002, Phys. Rev. B **65**, 085405.

Harigaya, K., and M. Fujita, 1993, Phys. Rev. B **47**, 16563.

Harris, P. J. F., 1999, *Carbon Nanotubes and Related Structures* (Cambridge University Press, Cambridge, England).

Hashimoto, A., K. Suenaga, A. Gloter, K. Urita, and S. Iijima, 2004, Nature (London) **430**, 870.

Heinze, S., M. Radosavljević, J. Tersoff, and Ph. Avouris, 2003, Phys. Rev. B **68**, 235418.

Heinze, S., J. Tersoff, R. Martel, V. Derycke, J. Appenzeller, and Ph. Avouris, 2002, Phys. Rev. Lett. **89**, 106801.

Hertel, T., and G. Moos, 2000, Phys. Rev. Lett. **84**, 5002.

Hirahara, K., M. Kociak, S. Bandow, T. Nakahira, K. Ito, Y. Saito, and S. Iijima, 2006, Phys. Rev. B **73**, 195420.

Hirahara, K., K. Suenaga, S. Bandow, H. Kato, T. Okazaki, H. Shinohara, and S. Iijima, 2000, Phys. Rev. Lett. **85**, 5384.

Hjort, M., and S. Stafström, 2001, Phys. Rev. B **63**, 113406.

Hornbaker, D. J., S.-J. Kahng, S. Misra, B. W. Smith, A. T. Johnson, E. J. Mele, D. E. Luzzi, and A. Yazdani, 2002, Science **295**, 828.

Huang, Y., X. F. Duan, Y. Cui, L. J. Lauhon, K. H. Kim, and C. M. Lieber, 2001, Science **294**, 1313.

Huang, Y., M. Okada, K. Tanaka, and T. Yamabe, 1996, Phys. Rev. B **53**, 5129.

Imry, Y., 1997, *Introduction to Mesoscopic Physics* (Oxford University Press, Oxford).

Iijima, S., 1991, Nature (London) **354**, 56.

Iijima, S., and T. Ichihashi, 1993, Nature (London) **363**, 603.

Ishii, H., *et al.*, 2003 Nature (London) **426**, 540.

Jarillo-Herrero, P., J. Kong, H. S. J. van der Zant, C. Dekker, L. P. Kouwenhoven, and S. De Franceschi, 2005, Phys. Rev. Lett. **94**, 156802.

Jarillo-Herrero, P., S. Sapmaz, C. Dekker, L. P. Kouwenhoven, and H. S. J. van der Zant, 2004, Nature (London) **429**, 389.

Javey, A., J. Guo, M. Paulsson, Q. Wang, D. Mann, M. Lundstrom, and H. Dai, 2004, Phys. Rev. Lett. **92**, 106804.

Jensen, P., J. Gale, and X. Blase, 2002, Phys. Rev. B **66**, 193403.

Jhi, S.-H., S. G. Louie, and M. L. Cohen, 2005, Phys. Rev. Lett. **95**, 226403.

Jiang, J., J. Dong, and D. Y. Xing, 2000, Phys. Rev. B **62**, 13209.

Jiang, J., J. Dong, H. T. Yang, and D. Y. Xing, 2001, Phys. Rev. B **64**, 045409.

Jiang, J., R. Saito, Ge. G. Samsonidze, S. G. Chou, A. Jorio, G. Dresselhaus, and M. S. Dresselhaus, 2005, Phys. Rev. B **72**, 235408.

Jishi, R. A., M. S. Dresselhaus, and G. Dresselhaus, 1993, Phys. Rev. B **48**, 11385.

Jorio A., C. Fantini, M. A. Pimenta, D. A. Heller, M. S. Strano, M. S. Dresselhaus, Y. Oyama, J. Jiang, and R. Saito, 2006, Appl. Phys. Lett. **88**, 023109.

Jorio, A., A. G S Filho, G. Dresselhaus, M. S. Dressellhaus, R. Saito, J. H. Hafner, C. M. Lieber, F. M. Matinaga, M. S. S. Dantas, and M. A. Pimenta, 2001, Phys. Rev. B **63**, 245416.

Jouguelet, E., C. Mathis, and P. Petit, 2000, Chem. Phys. Lett. **318**, 561.

Kamaras, K., M. E. Itkis, H. Hu, B. Zhao, and R. C. Haddon, 2003, Science **301**, 1501.

Kamide, K., T. Kimura, M. Nishida, and S. Kurihara, 2003, Phys. Rev. B **68**, 024506.

Kanda, A., K. Tsukagoshi, Y. Aoyagi, and Y. Ootuka, 2005, Phys. Rev. Lett. **92**, 036801.

Kanda, A., S. Uryu, K. Tsukagoshi, Y. Ootuka, and Y. Aoyagi, 2002, Physica B **323**, 246.

Kane, C. L., L. Balents, and M. P. A. Fisher, 1997, Phys. Rev. Lett. **79**, 5086.

Kane, C. L., and E. J. Mele, 1997, Phys. Rev. Lett. **78**, 1932.

Kane, C. L., and E. J. Mele, 2003, Phys. Rev. Lett. **90**, 207401.

Kane, C. L., E. J. Mele, R. S. Lee, J. E. Fischer, P. Petit, H.

Dai, A. Thess, R. E. Smalley, A. R. M. Verschueren, S. J. Tans, and C. Dekker, 1998, Europhys. Lett. **41**, 683.

Kasumov, A. Y., R. Deblock, M. Kociak, B. Reulet, H. Bouchiat, I. I. Khodos, Y. B. Gorbatov, V. T. Volkov, C. Journet, and M. Burghard, 1998, Science **284**, 1508.

Kasumov, A., M. Kociak, M. Ferrier, R. Deblock, S. Guéron, B. Reulet, I. Khodos, O. Stéphan, and H. Bouchiat, 2003, Phys. Rev. B **68**, 214521.

Kataura, H., Y. Kumazawa, Y. Maniwa, I. Umezu, S. Suzuki, Y. Ohtsuka, and Y. Achiba, 1999, Synth. Met. **103**, 2555.

Kaun, C. C., B. Larade, H. Mehrez, J. Taylor, and H. Guo, 2002, Phys. Rev. B **65**, 205416.

Kazaoui, S., N. Minami, R. Jacquemin, H. Kataura, and Y. Achiba, 1999, Phys. Rev. B **60**, 13339.

Ke, S.-H., W. Yang, and H. U. Baranger, 2006, J. Chem. Phys. **124**, 181102.

Khan, F., and P. Allen, 1984, Phys. Rev. B **29**, 3341.

Khazaei, M., A. A. Farajian, and Y. Kawazoe, 2005, Phys. Rev. Lett. **95**, 177602.

Kociak, M., A. Y. Kasumov, S. Guéron, B. Reulet, I. I. Khodos, Yu. B. Gorbatov, V. T. Volkov, L. Vaccarini, and H. Bouchiat, 2001, Phys. Rev. Lett. **86**, 2416.

Kociak, M., K. Suenaga, K. Hirahara, Y. Saito, T. Nakahira, and S. Iijima, 2002, Phys. Rev. Lett. **89**, 155501.

Kohn, W., 1959, Phys. Rev. Lett. **2**, 393.

Kong, J., and H. Dai, 2001, J. Phys. Chem. B **105**, 2890.

Kong, J., N. R. Franklin, C. Zhou, M. G. Chapline, S. Peng, K. Cho, and H. Dai, 2000, Science **28**, 622.

Krstić, V., S. Blumentritt, J. Muster, S. Roth, and A. Rubio, 2003, Phys. Rev. B **67**, 041401(R).

Kubo, R., 1966, Rep. Prog. Phys. **29**, 255.

Kwon, Y-K., and D. Tománek, 1998, Phys. Rev. B **58**, R16001.

Lambin, Ph., A. Fonseca, J.-P. Vigneron, J. B. Nagy, and A. A. Lucas, 1995, Chem. Phys. Lett. **245**, 85.

Lambin, Ph., V. Meunier, and A. Rubio, 2000, Phys. Rev. B **62**, 5129.

Lambin, Ph., L. Philippe, J.-C. Charlier, and J.-P. Michenaud, 1994, Comput. Mater. Sci. **2**, 350.

Lammert, P. E., V. H. Crespi, and A. Rubio, 2001, Phys. Rev. Lett. **87**, 136402.

Lammert, P. E., P. Zhang, and V. H. Crespi, 2000, Phys. Rev. Lett. **84**, 2453.

Langer, J. S., and V. Ambegaokar, 1967, Phys. Rev. **164**, 498.

Latil, S., S. Roche, and J.-C. Charlier, 2005, Nano Lett. **5**, 2216.

Latil, S., S. Roche, D. Mayou, and J.-C. Charlier, 2004, Phys. Rev. Lett. **92**, 256805.

Latil, S., F. Triozon, and S. Roche, 2005, Phys. Rev. Lett. **95**, 126802.

Lauret, J. S., R. Arenal, F. Ducastelle, A. Loiseau, M. Cau, B. Attal-Tretout, E. Rosencher, and L. Goux-Capes, 2005, Phys. Rev. Lett. **94**, 037405.

Lazzeri, M., S. Piscanec, F. Mauri, A. C. Ferrari, and J. Robertson, 2005, Phys. Rev. Lett. **95**, 236802.

Lazzeri, M., S. Piscanec, F. Mauri, A. C. Ferrari, and J. Robertson, 2006, Phys. Rev. B **73**, 155426.

Lee, J., S. Eggert, H. Kim, S. J. Kahng, H. Shinohara, and Y. Kuk, 2004, Phys. Rev. Lett. **93**, 166403.

Lee, J., H. Kim, S.-J. Kahng, G. Kim, Y.-W. Son, J. Ihm, H. Kato, Z. W. Wang, T. Okazaki, H. Shinohara, and Y. Kuk, 2002, Nature (London) **415**, 1005.

Lee, J.-O., J.-R. Kim, J.-J. Kim, J. Kim, N. Kim, J. W. Park, and K.-H. Yoo, 2000, Solid State Commun. **115**, 467.

Lee, H.-W, and D. S. Novikov, 2003, Phys. Rev. B **68**, 155402.

Lee, Y.-S., M. Buongiorno Nardelli, and N. Marzari, 2005, Phys. Rev. Lett. **95**, 076804.

Lefebvre, J., Y. Homma, and P. Finnie, 2003, Phys. Rev. Lett. **90**, 217401.

Lehtinen, P. O., A. S. Foster, A. Ayuela, A. Krasheninnikov, K. Nordlund, and R. M. Nieminen, 2003, Phys. Rev. Lett. **91**, 017202.

Lemay, S. G., J. W. Janssen, M. van den Hout, M. Mooij, M. J. Bronikowski, P. A. Willis, R. E. Smalley, L. P. Kouwenhoven, and C. Dekker, 2001, Nature (London) **412**, 617.

Léonard, F., and J. Tersoff, 1999, Phys. Rev. Lett. **83**, 5174.

Liu, H. J., and C. T. Chan, 2002, Phys. Rev. B **66**, 115416.

Liu, K., P. Avouris, R. Martel, and W. K. Hsu, 2001, Phys. Rev. B **63**, 161404(R).

Lin, M. F., and K. W.-K. Shung, 1995, Phys. Rev. B **51**, 7592.

Loiseau, A., P. Launois, P. Petit, S. Roche, and J.-P. Salvetat, 2006, *Understanding Carbon Nanotubes From Basics to Applications*, Lecture Notes in Physics Vol. 677 (Springer-Verlag, Berlin).

López Sancho, M. P., J. M. López Sancho, and J. Rubio, 1984, J. Phys. F: Met. Phys. **14**, 1205.

López Sancho, M. P., M. C. Muñoz, and L. Chico, 2001, Phys. Rev. B **63**, 165419.

Loudon, R., 1959, Am. J. Phys. **27**, 649.

Lovall, D., M. Buss, E. Graugnard, R. P. Andres, and R. Reifenberger, 2000, Phys. Rev. B **61**, 5683.

Lu, J.-P., 1995, Phys. Rev. Lett. **74**, 1123.

Luttinger, J. M., 1951, Phys. Rev. **84**, 814.

Luttinger, J. M., 1963, J. Math. Phys. **4**, 1154.

Machón, M., S. Reich, C. Thomsen, D. Sánchez-Portal, and P. Ordejón, 2002, Phys. Rev. B **66**, 155410.

Machón, M., *et al.*, 2005, Phys. Rev. B **66**, 155410.

Mahan, G. D., 2003, Phys. Rev. B **68**, 125409.

Mahan, G. D., 2004, Phys. Rev. B **69**, 125407.

Marinopoulos, A. G., L. Reining, A. Rubio, and N. Vast, 2003, Phys. Rev. Lett. **91**, 046402.

Martel, R., T. Schmidt, H. R. Shea, T. Hertel, and Ph. Avouris, 1998, Appl. Phys. Lett. **73**, 2447.

Martensson, T., P. Calberg, M. Borgstrom, L. Montelius, W. Seifert, and L. Samuelson, 2004, Nano Lett. **4**, 699.

Marty, L., E. Adam, L. Albert, R. Doyon, D. Ménard, and R. Martel, 2006, Phys. Rev. Lett. **96**, 136803.

Mattis, D. C., and E. H. Lieb, 1965, J. Math. Phys. **6**, 304.

Maultzsch, J., R. Pomraenke, S. Reich, E. Chang, D. Prezzi, A. Ruini, E. Molinari, M. S. Strano, C. Thomsen, and C. Lienau, 2005, Phys. Rev. B **72**, 241402(r).

Mayer, A., 2005, Carbon **43**, 717.

Mazzoni, M. S. C., R. W. Nunes, S. Azvedo, and H. Chacham, 2006, Phys. Rev. B **73**, 073108.

McEuen, P. L., M. Bockrath, D. H. Cobden, Y.-G. Yoon, and S. G. Louie, 1999, Phys. Rev. Lett. **83**, 5098.

Mehrez, H., H. Guo, J. Wang, and C. Roland, 2001, Phys. Rev. B **63**, 245410.

Mermin, N. D., and H. Wagner, 1966, Phys. Rev. Lett. **17**, 1133.

Meunier, V., M. Buongiorno Nardelli, J. Bernholc, T. Zacharia, and J.-C. Charlier, 2002, Appl. Phys. Lett. **81**, 5234.

Meyer, A., *et al.*, 2005, Carbon **43**, 717.

Mintmire, J. W., B. I. Dunlap, and C. T. White, 1992, Phys. Rev. Lett. **68**, 631.

Mintmire, J. W., and C. T. White, 1998, Phys. Rev. Lett. **81**, 2506.

Minot, E. D., Y. Yaish, V. Sazonova, and P. L. McEuen, 2004, Nature (London) **428**, 536.

Mingo, N., and J. Han, 2001, Phys. Rev. B **64**, 201401.

Mishchenko, E. G., and A. V., Andreev, 2002, Phys. Rev. B **65**, 235310.

Mishchenko, E. G., Andreev, and L. I. Glazman, 2001, Phys. Rev. Lett. **87**, 246801.

Misewich, J. A., R. Martel, Ph. Avouris, J. C. Tsang, S. Heinze, and J. Tersoff, 2003, Science **300**, 783.

Miyamoto, Y., A. Rubio, X. Blase, M. L. Cohen, and S. G. Louie, 1995, Phys. Rev. Lett. **74**, 2993.

Miyamoto, Y., S. Saito, and D. Tománek, 2001, Phys. Rev. B **65**, 041402(R).

Moos, M., *et al.*, 2001, Phys. Rev. Lett. **87**, 267402.

Mopurgo, A. F., J. Kong, C. M. Marcus, and H. Dai, 1998, Science **286**, 263.

Mora, C., R. Egger, and A. Altland, 2006, Phys. Rev. B **75**, 035310.

Nardelli, M. B., J.-L. Fattebert, and J. Bernholc, 2001, Phys. Rev. B **64**, 245423.

Nemec, N., and G. Cuniberti, 2006, Phys. Rev. B **74**, 165411.

Nemec, N., D. Tománek, and G. Cuniberti, 2006, Phys. Rev. Lett. **96**, 076802.

Nilsson, L., O. Groening, C. Emmenegger, O. Kuettel, E. Schaller, L. Schlapbach, H. Kind, J.-M. Bonard, and K. Kem, 2000, Appl. Phys. Lett. **76**, 2071.

Niquet, Y.-M., A. Lherbier, N. H. Quang, X. Blase, and Ch. Delerue, 2006, Phys. Rev. B **73**, 165319.

Novoselov, K. S., A. K. Geim, S. V. Morozov, D. Jiang, S. V. Dubonos, I. V. Girgorieva, and A. A. Firsov, 2004, Science **306**, 666.

Novoselov, K. S., A. K. Geim, S. V. Morozov, D. Jiang, M. I. Katsnelson, I. V. Girgorieva, S. V. Dubonos, and A. A. Firsov, 2005, Nature (London) **438**, 197.

Novoselov, K. S., E. McCann, S. V. Morozov, V. I. Fal'ko M. I. Katsnelson, U. Zeitler, D. Jiang, F. Schedin, and A. K. Geim, 2006, Nat. Phys. **2**, 177.

Nozières, P., and D. Pines, 1999, *Theory of Quantum Liquids* (Perseus, New York).

Nygard, J., *et al.*, 1999, Appl. Phys. A **69**, 297.

O'Connell, M. J., S. M. Bachilo, C. B. Huffman, V. C. Moore, M. S. Strano, E. H. Haroz, K. L. Rialon, P. J. Boul, W. H. Noon, C. Kittrell, J. Ma, R. H. Hauge, R. B. Weisman, and R. E. Smalley, 2002, Science **297**, 593.

Odbadrakh, K., P. Pomorski, and Ch. Roland, 2006, Phys. Rev. B **73**, 233402.

Odom, T. W., J. L. Huang, P. Kim, and C. M. Lieber, 1998, Nature (London) **391**, 62.

Odom, T. W., J.-L. Huang, and C. M. Lieber, 2002, J. Phys.: Condens. Matter **14**, R145.

Ogawa, T., and T. Takagahara, 1991a, Phys. Rev. B **43**, 14325.

Ogawa, T., and T. Takagahara, 1991b, Phys. Rev. B **44**, 8138.

Ohta, T., A. Bodtwick, T. Seyller, K. Horn, and E. Rotenberg, 2006, Science **313**, 951.

Okada, S., and A. Oshiyama, 2005, Phys. Rev. Lett. **95**, 206804.

Orlikowski, D., M. Buongiorno Nardelli, J. Bernholc, and C. Roland, 2000, Phys. Rev. B **61**, 14194.

Ouyang, M., J.-L. Huang, C. L. Cheung, and C. M. Lieber, 2001a, Science **291**, 97.

Ouyang, M., J. L. Huang, C. L. Cheung, and C. M. Lieber, 2001b, Science **292**, 702.

Palacios, J. J., A. J. Perez-Jimenez, E. Louis, E. SanFabian, and J. A. Verges, 2003, Phys. Rev. Lett. **90**, 106801.

Papadopoulos, C., A. Rakitin, J. Li, A. S. Vedeneev, and J. M. Xu, 2000, Phys. Rev. Lett. **85**, 3476.

Park, C.-H., C. D. Spataru, and S. G. Louie, 2006, Phys. Rev. Lett. **96**, 126105.

Park, J.-Y., S. Rosenblatt, Y. Yaish, V. Sazonova, H. Ustunel, S. Braig, T. A. Arias, P. W. Brouwer, and P. L. McEuen, 2004, Nano Lett. **4**, 517.

Park, N., and S. Hong, 2005, Phys. Rev. B **72**, 045408.

Peierls, R E., 1933, Z. Phys. **80**, 763.

Peng, S., and K. Cho, 2003, Nano Lett. **3**, 513.

Perebeinos, V., and Ph. Avouris, 2006, Phys. Rev. B **74**, 121410.

Perebeinos, V., J. Tersoff, and Ph. Avouris, 2004, Phys. Rev. Lett. **92**, 257402.

Perebeinos, V., J. Tersoff, and Ph. Avouris, 2005, Phys. Rev. Lett. **94**, 086802.

Petit, P., C. Mathis, C. Journet, and P. Bernier, 1999, Chem. Phys. Lett. **305**, 370.

Piscanec, S., M. Lazzeri, F. Mauri, A. C. Ferrari, and J. Robertson, 2004, Phys. Rev. Lett. **93**, 185503.

Poncharal, P., C. Berger, Z. L. Wang, and W. A. de Heer, 2002, J. Phys. Chem. **106**, 12104.

Popov, V. N., and L. Henrard, 2004, Phys. Rev. B **70**, 115407.

Popov, V. N., and Ph. Lambin, 2006a, Phys. Rev. B **73**, 085407.

Popov, V. N., and Ph. Lambin, 2006b, Phys. Rev. B **74**, 075415.

Purcell, S., P. Vincent, C. Journet, and V. T. Binh, 2002a, Phys. Rev. Lett. **88**, 105502.

Purcell, S., P. Vincent, C. Journet, and V. T. Binh, 2002b, Phys. Rev. Lett. **89**, 276103.

Purcell, S., P. Vincent, M. Rodriguez, C. Journet, S. Vignoli, D. Guillot, and A. Ayari, 2006, Chem. Vap. Deposition **12**, 331.

Radosavljević, M., J. Appenzeller, Ph. Avouris, and J. Knoch, 2004, Appl. Phys. Lett. **84**, 3693.

Rao, A. M., P. C. Ecklund, S. Bandow, A. Thess, and R. E. Smalley, 1997, Nature (London) **388**, 257.

Reich, S., J. Maultzsch, C. Thomsen, and P. Ordejón, 2002, Phys. Rev. B **66**, 035412.

Reich, S., C. Thomsen, and J. Maultzsch, 2004, *Carbon Nanotubes, Basic Concepts and Physical Properties* (Wiley-VCH Verlag GmbH, Weinheim).

Reich, S., C. Thomsen, and P. Ordejón, 2002, Phys. Rev. B **65**, 155411.

Reich, S., C. Thomsen, and J. Robertson, 2005, Phys. Rev. Lett. **95**, 077402.

Rinzler, A. G., J. H. Hafner, P. Nikolaev, L. Lou, S. G. Kim, D. Tománek, P. Nordlander, D. T. Colbert, and R. E. Smalley, 1995, Science **269**, 1550.

Roche, S., 1999, Phys. Rev. B **59**, 2284.

Roche, S., G. Dresselhaus, M. S. Dresselhaus, and R. Saito, 2000, Phys. Rev. B **62**, 16092.

Roche, S., J. Jiang, F. Triozon, and R. Saito, 2005a, Phys. Rev. Lett. **95**, 076803.

Roche, S., J. Jiang, F. Triozon, and R. Saito, 2005b, Phys. Rev. B **72**, 113410.

Roche, S., and D. Mayou, 1997, Phys. Rev. Lett. **79**, 2518.

Roche, S., and R. Saito, 2001, Phys. Rev. Lett. **87**, 246803.

Roche, S., F. Triozon, A. Rubio, and D. Mayou, 2001a, Phys. Rev. B **64**, 121401.

Roche, S., F. Triozon, A. Rubio, and D. Mayou, 2001b, Phys. Rev. Lett. A **285**, 94.

Rochefort, A., Ph. Avouris, F. Lesage, and D. R. Salahub, 1999, Phys. Rev. B **60**, 13824.

Rocquefelte, X., G.-M. Rignanese, V. Meunier, H. Terrones, M. Terrones, and J.-C. Charlier, 2004, Nano Lett. **4**, 805.

Rollbühler J., and H. Grabert, 2001, Phys. Rev. Lett. **87**, 126804.

Rubio, A., J. Corkill, and M. L. Cohen, 1994, Phys. Rev. B **49**, 5081.

Rubio, A., Y. Miyamoto, X. Blase, M. L. Cohen, and S. G. Louie, 1996, Phys. Rev. B **53**, 4023.

Rubio, A., D. Sánchez-Portal, E. Artacho, P. Ordejón, and J. M. Soler, 1999, Phys. Rev. Lett. **82**, 3520.

Saito, R., G. Dresselhaus, and M. S. Dresselhaus, 1993, J. Appl. Phys. **73**, 494.

Saito, R., G. Dresselhaus, and M. S. Dresselhaus, 1994, Phys. Rev. B **50**, 14698.

Saito, R., G. Dresselhaus, and M. S. Dresselhaus, 1996, Phys. Rev. B **53**, 2044.

Saito, R., G. Dresselhaus, and M. S. Dresselhaus, 1998, *Physical Properties of Carbon Nanotubes* (Imperial College Press, London).

Saito, R., G. Dresselhaus, and M. S. Dresselhaus, 2000, Phys. Rev. B **61**, 2981.

Saito, R., M. Fujita, G. Dresselhaus, and M. S. Dresselhaus, 1992, Appl. Phys. Lett. **60**, 2204.

Saito, Y., K. Hata, and T. Murata, 2000, Jpn. J. Appl. Phys., Part 2 **39**, L271.

Sánchez-Portal, D., *et al.*, 1999, Phys. Rev. B **59**, 12678.

Sanvito, S., Y. K. Kwon, D. Tománek, and C. J. Lambert, 2000, Phys. Rev. Lett. **84**, 1974.

Sapmaz, S., P. Jarillo-Herrero, Ya. M. Blanter, C. Dekker, and H. S. J. van der Zant, 2006 Phys. Rev. Lett. **96**, 026801.

Sédéki, A., L. G. Caron, and C. Bourbonnais, 2000, Phys. Rev. B **62**, 6975.

Sédéki, A., L. G. Caron, and C. Bourbonnais, 2002, Phys. Rev. B **65**, 140515.

Seri, T., and T. Ando, 1997, J. Phys. Soc. Jpn. **66**, 169.

Shan, B., and K. Cho, 2004, Phys. Rev. B **70**, 233405.

Shea, H. R., R. Martel, and P. Avouris, 2000, Phys. Rev. Lett. **84**, 4441.

Shim, M., A. Javey, N. W. S. Kam, and H. Dai, 2001, J. Am. Chem. Soc. **123**, 11512.

Shyu, F. L., C. P. Chang, R. B. Chen, C. W. Chiu, and M. F. Lin, 2003, Phys. Rev. B **67**, 045405.

Slonczewski, J. C., and P. R. Weiss, 1958, Phys. Rev. **109**, 272.

Smith, B. W., M. Monthioux, and D. E. Luzzi, 1998, Nature (London) **396**, 323.

Solyom, J., 1979, Adv. Phys. **28**, 201.

Son, Y.-W., M. L. Cohen, and S. G. Louie, 2006a, Phys. Rev. Lett. **97**, 216803.

Son, Y.-W., M. L. Cohen, and S. G. Louie, 2006b, Nature (London) **444**, 347.

Son, Y.-W., J. Ihm, M. L. Cohen, S. G. Louie, and H. J. Choi, 2005, Phys. Rev. Lett. **95**, 216602.

Spataru, C. D., M. A. Cazalilla, A. Rubio, L. X. Benedict, P. M. Echenique, and S. G. Louie, 2001, Phys. Rev. Lett. **87**, 246405.

Spataru, C. D., S. Ismail-Beigi, L. X. Benedict, and S. G. Louie, 2004, Phys. Rev. Lett. **92**, 077402.

Spataru, C. D., S. Ismail-Beigi, R. B. Capaz, and S. G. Louie, 2005, Phys. Rev. Lett. **95**, 247402.

Stojetz, B., C. Miko, L. Forro, and Ch. Strunk, 2005, Phys. Rev. Lett. **94**, 186802.

Stojetz, B., S. Roche, C. Miko, F. Triozon, L. Forro, and Ch. Strunk, 2006, unpublished.

Stone, A. J., and D. J. Wales, 1986, Chem. Phys. Lett. **128**, 501.

Strano, M. S., C. A. Dyke, M. L. Usrey, P. W. Barone, M. J. Allen, H. Shan, C. Kittrell, R. H. Hauge, J. M. Tour, and R. E. Smalley, 2003, Science **301**, 1519.

Suenaga, K., C. Colliex, N. Demoncy, A. Loiseau, H. Pascard, and F. Willaime, 1997, Science **278**, 653.

Sumanasekera, G. U., C. K. W. Adu, S. Fang, and P. C. Eklund, 2000, Phys. Rev. Lett. **85**, 1096.

Suzuura, H., and T. Ando, 2002, Phys. Rev. B **65**, 235412.

Szafer, A., and A. D. Stone, 1988, IBM J. Res. Dev. **32**, 84.

Takesue, I., J. Haruyama, N. Kobayashi, S. Chiashi, S. Maruyama, T. Sugai, and H. Shinohara, 2006, Phys. Rev. Lett. **96**, 057001.

Takenobu, T., T. Takano, M. Shiraishi, Y. Murakami, M. Ata, H. Kataura, Y. Achiba, and Y. Iwasa, 2003, Nat. Mater. **2**, 683.

Tamura, T., and M. Tsukada, 1995, Phys. Rev. B **52**, 6015.

Tanaka, K., *et al.*, 1997, Int. J. Quantum Chem. **63**, 637.

Tang, Z. K., Lingyun Zhang, N. Wang, X. X. Zhang, G. H. Wen, G. D. Li, J. N. Wang, C. T. Chan, and P. Sheng, 2001, Science **292**, 2462.

Tans, S. J., A. R. M. Verschueren, and C. Dekker, 1998, Nature (London) **393**, 49.

Tarkiainen, R., M. Ahlskog, J. Penttilä, L. Roschier, P. Hakonen, M. Paalanen, and E. Sonin, 2001, Phys. Rev. B **64**, 195412.

Telling, R. H., C. P. Ewels, A. A. El-Barbary, and M. I. Heggie, 2003, Nat. Mater. **2**, 333.

Terrones, M., F. Banhart, N. Grobert, J.-C. Charlier, H. Terrones, and P. M. Ajayan, 2002, Phys. Rev. Lett. **89**, 075505.

Terrones, M., H. Terrones, F. Banhart, J.-C. Charlier, and P. M. Ajayan, 2000, Science **288**, 1226.

Terrones, H., M. Terrones, E. Hernandez, N. Grobert, J.-C. Charlier, and P. M. Ajayan, 2000, Phys. Rev. Lett. **84**, 1716.

Tersoff, J., 1984, Phys. Rev. Lett. **52**, 465.

Thouless, D. J., 1973, J. Phys. C **6**, 249.

Thouless, D. J., 1977, Phys. Rev. Lett. **39**, 1167.

Tian, W., and S. Datta, 1994, Phys. Rev. B **49**, 5097.

Tinkham, M., 1996, *An Introduction to Superconductivity* (McGraw-Hill, New York), Chap. 8.

Tománek, D., and R. J. Enbody, 1999, *Science and Application of Nanotubes* (Kluwer Academic, Dordrecht).

Tomonaga, S., 1950, Prog. Theor. Phys. **5**, 544.

Triozon, F., Ph. Lambin, and S. Roche, 2005, Nanotechnology **16**, 230.

Triozon, F., S. Roche, A. Rubio, and D. Mayou, 2004, Phys. Rev. B **69**, 121410.

Urbina, U., I. Echeverria, A. Perez-Garrido, A. Diaz-Sanchez, and J. Abellan, 2003, Phys. Rev. Lett. **90**, 106603.

Uryu, S., and T. Ando, 2005, Phys. Rev. B **72**, 245403.

Venema, L. C., V. Meunier, Ph. Lambin, and C. Dekker, 2000, Phys. Rev. B **61**, 2991.

Venema, L. C., J. W. G. Wildöer, J. W. Janssen, S. J. Tans, H. L. J. Temminck, Tuinstra, L. P. Kouwenhoven, and C. Dekker, 1999, Science **283**, 52.

Vincent, P., S. T. Purcell, C. Journet, and V. T. Binh, 2002, Phys. Rev. B **66**, 075406.

Voit, J., 1995, Rep. Prog. Phys. **58**, 977.

Vucović, T., I. Milošević, and M. Damnjanović, 2002, Phys. Rev. B **65**, 045418.

Wallace, P. R., 1947, Phys. Rev. **71**, 622.

Wang, D., B. Sheriff, and J. R. Heath, 2006, Nano Lett. **6**, 1096.

Wang, F., G. Dukovic, L. E. Brus, and T. F. Heinz, 2004, Phys. Rev. Lett. **92**, 177401.

Wang, F., G. Dukovic, L. E. Brus, and T. F. Heinze, 2005a, Science **308**, 838.

Wang, F., G. Dukovic, L. E. Brus, and T. F. Heinze, 2005b, Science **309**, 1677.

Wang, N., Z. K. Tang, G. D. Li, and J. S. Chen, 2000, Nature (London) **408**, 50.

Wang, S., and M. Griffoni, 2005, Phys. Rev. Lett. **95**, 266802.

Wang, S., M. Griffoni, and S. Roche, 2006, Phys. Rev. B **74**, 121407.

Watanabe, K., T. Taniguchi, and H. Kanda, 2004, Nat. Mater. **3**, 404.

Watanabe, M. O., S. Itoh, T. Sasaki, and K. Mizushima, 1996, Phys. Rev. Lett. **77**, 187.

Webb, R., S. Washburn, C. Umbach, and R. Laibowitz, 1985, Phys. Rev. Lett. **54**, 2696.

White, C. T., and J. W. Mintmire, 1998, Nature (London) **394**, 29.

White, C. T., and T. N. Todorov, 1998, Nature (London) **393**, 240.

Wildöer, J. W. G., L. C. Venema, A. G. Rinzler, R. E. Smalley, and C. Dekker, 1998, Nature (London) **391**, 59.

Wirtz, L., A. Marini, and A. Rubio, 2006, Phys. Rev. Lett. **96**, 126104.

Wong, S. S., E. Joselevich, A. T. Woolley, C. L. Cheung, and C. M. Lieber, 1998, Nature (London) **394**, 52.

Xu, S., *et al.*, 1996, Phys. Rev. Lett. **76**, 483.

Xue, Y., and M. Ratner, 2004, Phys. Rev. B **70**, 205416.

Yang, L., and J. Han, 2000, Phys. Rev. Lett. **85**, 154.

Yao, Z., C. L. Kane, and C. Dekker, 2000 Phys. Rev. Lett. **84**, 2941.

Yao, Z., H. W. Postma, L. Balents, and C. Dekker, 1999, Nature (London) **402**, 273.

Yi, J.-Y., and J. Bernholc, 1993, Phys. Rev. B **47**, 1708.

Yoon, Y.-G., P. Delanay, H. J. Choi, J. Ihm, and S. G. Louie, 2002, Phys. Rev. B **69**, 073407.

Yoon, Y.-G., M. S. C. Mazzoni, H. J. Choi, J. Ihm, and S. G. Louie, 2001, Phys. Rev. Lett. **86**, 688.

Zaric, S., G. N. Ostojic, J. Kono, J. Shaver, V. C. Moore, M. S. Strano, R. H. Hauge, R. E. Smalley, and X. Wei, 2004, Science **304**, 1129.

Zaric, S., *et al.*, 2005, Phys. Rev. Lett. **96**, 016406.

Zhang, Y., Y. W. Tan, H. L. Stormer, and Ph. Kim, 2005, Nature (London) **438**, 201.

Zheng, X., G. Chen, Z. Li, S. Deng, and N. Xu, 2004, Phys. Rev. Lett. **92**, 106803.

Zhou, C., J. Kong, E. Yenilmez, and H. Dai, 2000, Science **290**, 1552.

Zhou, S. Y., G.-H. Gweon, J. Graf, A. V. Fedorov, C. D. Spataru, R. D. Diehl, Y. Kopelevich, D.-H. Lee, S. G. Louie, and A. Lanzara, 2006, Nat. Phys. **2**, 595.

Zhou, X., J.-Y. Park, S. Huang, J. Liu, and P. L. McEuen, 2005, Phys. Rev. Lett. **95**, 146805.

Zhu, W. G., and E. Kaxiras, 2006, Nano Lett. **6**, 1415.